ABSTRACT

Title of Dissertation: THE GENESIS OF TYPHOON CHANCHU (2006)

Wallace A. Hogsett, Ph.D., 2010

Directed By: Professor Da-Lin Zhang
Department of Atmospheric and Oceanic Science

The phenomenon of tropical cyclogenesis (TCG), defined as the processes by which common tropical convection organizes into a coherent, self-sustaining, rapidly-rotating, and potentially destructive tropical cyclone (TC), consistently headlines research efforts but still remains largely mysterious. TCG has been described by a leading TC scientist as "one of the great remaining mysteries of the tropical atmosphere." This dissertation was motivated by a specific case of TCG: the near-equatorial formation of a well-organized synoptic cyclonic disturbance during the active West Pacific Madden-Julian Oscillation (MJO). At very high resolution, the Weather Research and Forecasting (WRF) mesoscale atmospheric model proves capable of reproducing the multiscale interactions that comprise the TCG of Typhoon Chanchu.

In the first part of the dissertation, the synoptic observations of the incipient disturbance (i.e., weak cyclonic vortex) are compared with the results from the WRF simulation. It is found that the disturbance tilts westward with height, and as a consequence of the vertical tilt, large-scale ascent (and thus precipitation) is dynamically favored on the downtilt-right side of the vortex. A major result is that the precipitation to the north of the tilted vortex serves as an attractor to the vortex

through its generation of vorticity, thereby serving to dually diminish the vertical tilt of the vortex and deflect the incipient storm northward. Observations and the model simulation both indicate that TCG commences when the storm becomes vertically upright.

In the second part of the dissertation, it is shown that the simulated downtilt-right precipitation takes the form of several mesoscale convective systems (MCSs), which spawn midlevel vortices that merge with and intensify the midlevel vortex. The precipitation during the several days prior to TCG generally serves to precondition the near-vortex environment by raising the low- and midlevel humidity. Apparently, the onset of TCG can be characterized as the transition of a tilted cold-core vortex into a vertically-erect warm-core vortex.

The final part of the dissertation addresses the storm-scale processes during the day of TCG. The primary point of emphasis is the vertical wind shear, which is often dismissed as detrimental to the prospect of TCG. On the contrary, it is found that the inherent vertical shear of the tilted vortex is actually the critical variable in understanding the TCG of Chanchu through its role in the vorticity tilting term. More specifically, the clockwise turning (i.e., veering) of the shear vector with height suggests a new mechanism for the rapid generation of system-scale vorticity, which current hypotheses posit as simply a stochastic amalgamation of vorticity sufficient to trigger self-intensification. The near-surface spin-up mechanism is analogous to that which occurs in supercell thunderstorms. The missing link in TCG understanding may be the dynamic implications of the veering wind profile in which the convection develops.

THE GENESIS OF TYPHOON CHANCHU (2006)

By

Wallace A. Hogsett

Dissertation submitted to the Faculty of the Graduate School of the
University of Maryland, College Park, in partial fulfillment
of the requirements for the degree of
Doctor of Philosophy
2010

Advisory Committee:
Prof. Da-Lin Zhang, Chair
Prof. James Carton
Prof. Daniel Kirk-Davidoff
Prof. Hugo Berbery
Prof. Karen Prestegaard (Dean's Representative)

Preface

This dissertation is presented in a simple five-chapter format, in which the first chapter provides a basic, broad, and bullish perspective of the present understanding, the outstanding issues of interest, and the need for continued tropical cyclogenesis (TCG) research. Each of Chapters 2 – 4 represents a self-contained study of the genesis of Typhoon Chanchu. The chapters build on one another and logically progress from synoptic scales and weekly timescales (Chapter 2), to mesoscale and daily timescales (Chapter 3), and finally to the storm scale and hourly timescales (Chapter 4). The final chapter summarizes the major findings and sketches the research path forward.

The three middle chapters are organized as three dependent submissions to the literature. Chapter 2 has been submitted as an article to the *Journal of the Atmospheric Sciences* (January 2010), and Chapters 3 and 4 will similarly be submitted in the coming months as Part II and Part III of this ongoing study. The final Chapter 5 contains the plan for continued study of what appears to be a rich dataset, as well as future theoretical and practical extensions of the scientific findings presented herein.

Dedication

To the late Jean Grace.

Acknowledgements

Thanks to: Dad for encouraging me to spend time enjoying the outdoors; Mom for encouraging me to do anything I wanted to do; Will and Hal for camaraderie throughout the years; Prof. Zhang for providing the requisite tools and unfettered freedom to innovate while wielding ruthless constructive criticism; Alex and Charcoal; John for encouraging occasional irresponsibility; Joel for endless encouragement; Ashley for pretending to listen to my half-constructed theories on tropical cyclogenesis; the U.S. State Department for auxiliary education; Chanh for confidence; Rich for encouraging me to come to graduate school in DC; and of course the weather, for giving me something to do with my life.

??This work was supported by ONR Grant N000140710186, and NSF ATM0758609.

Table of Contents

Chapter 1: Introduction

1.1. Statement of the problem

The formation of tropical cyclones (TCs) is fundamentally misunderstood-too strong??. Consistent observations are sparse in the vast tropical oceans, and field projects require extraordinary funding to adequately sample nascent storms. Thus the acquisition of a dataset that is capable of resolving the multiscale interactions that comprise TCG is one of the greatest challenges to TCG investigators. In fact, data scarcity is probably *the* limiting factor preventing a more complete understanding of TCG, since the densely-sampled land-based vortical storms are significantly better understood.

Each year many tropical waves and mesoscale??convective clusters develop in the tropics, but only a selected?? few undergo TCG. Of course, the limited observational resources (e.g. aircraft hours, dropsondes, etc.) can spread thin very quickly in the face of innumerable TC "prospects." This is especially true when existing observational resources are directed at mature TCs that threaten coastal wealth rather than those developing in the open ocean. An exception is a handful of targeted observational field campaigns that have contributed significantly to an increasing, albeit slowly, understanding of TCG in the past half-century.

1.2. Importance of the problem

While it could be argued that TCG should be a secondary forecasting concern, with the track and intensity forecasts of mature TCs that do extensive damage as the primary concern, it is concerning how little is understood about the TCG process.

Often TCG is only noticed after it has begun. Indeed, most TCG cases do occur far from land in the open ocean, including the case of Chanchu presented herein, but TCG can occur near shore, quickly, and without forecast skill. Such cases present a great risk to coastal populations. Several cases of poorly-forecast, near-land TCG in the recent past (e.g. Hurricane Humberto, 2007) remain the subject of intense investigation, but until a fundamental understanding of the TCG processes is attained, TCG forecasts of such dangerous cases will fail. itis needed because of extended fcst??

If case studies, such as the present study, can provide any improved understanding of the structures?? and evolution of pre-TC disturbances and their associated TCG, forecasts could benefit. Given finite observational capabilities, improved understanding could help to more efficiently target observations toward high-value locations that may impact TCG more than others. To the extent that improved understanding is obtained from analyses herein, and subsequently generalized, more precisely targeted observations and unique forecasting techniques will certainly follow.

1.3. Scope of the problem

Stressing depth over breadth, this dissertation is based almost exclusively on a single numerical simulation in which a single episode of TCG is completely captured at cloud-resolving scale. To the extent that the current generation of mesoscale atmospheric models can provide a dynamically consistent perspective of the atmosphere, the point at issue in this dissertation is not one of *forecasting* TCG, but instead one of *understanding* the TCG process through the acquisition and analysis of a high-resolution TCG dataset. Until now, no such dataset has been obtained (or if

so, it has not been analyzed in depth)too strong??. An attempt is made to shed light on processes that contribute to intensification at various scales and have eluded understanding until now should provide 2-3 pages review of TCG??.

Chapter 2: Formation of Chanchu during the MJO

2.1. Introduction

In the Western North Pacific (WNP) basin, the frequency of tropical cyclogenesis (TCG) peaks in the late northern summer, when the monsoon trough extends eastward from Asia into the Pacific Ocean. It is in this region that easterly trade winds meet westerly monsoon winds and sustain an environment that is favorable for enhanced convergence and rotation of the low-level winds. Previous studies have identified this low-latitude confluence zone at the easternmost extent of the monsoon trough as a focus for TCG (see Holland 1995).

However, few tropical cyclones (TCs) develop prior to June in the WNP, even though the necessary conditions for TCG persist year round (Gray 1998). This is because this region lacks climatological foci for TCG prior to the onset of the Asian monsoon. Instead, trade easterlies dominate the WNP during the spring months, and the rare TCs that do develop during this pre-monsoon environment are often associated with anomalous westerly equatorial winds that modulate the formation of TC precursor disturbances (Ritchie and Holland 1999). This is the case for the present study of Typhoon Chanchu, which developed in early May 2006. In fact, Mao and Wu (2008) found that Chanchu served as the trigger for the onset of the 2006 Asian monsoon through its modulation of the meridional temperature gradient.

The Madden-Julian Oscillation (MJO; Madden and Julian 1994) is the dominant mode of intraseasonal variability globally, and it was first discussed by Liebmann et al. (1994) as a favorable environment for TCG. Barrett and Leslie (2009) showed

that the MJO significantly modulates TC activity in all ocean basins worldwide through its enhancement of low-level vorticity and deep convection. In general, the MJO can be characterized as a wavelike disturbance that propagates eastward from the equatorial Indian Ocean into the WNP; its active phase is associated with active deep convection and westerly winds in the lower troposphere, the so-called westerly wind bursts (WWBs). Near-equatorial WWBs converge with easterly trades during the active phase of the MJO, not only enhancing deep convection, but also facilitating the growth of cyclonic disturbances through wave accumulation - a process by which cyclonic vorticity associated with traveling disturbances is gathered in a region of converging zonal wind (Chang and Webster 1990). When WWBs impinge on the easterly trades, the cyclonic vorticity associated with the zonal wind shear allows northwestward-moving cyclonic eddies to develop via barotropic energy conversions, as found by Maloney and Hartmann (2001). These sub-synoptic eddies can serve as precursors to TCG (Aiyyer and Molinari 2003), and if the eddies are continuously produced they can repeatedly spawn TCs (Molinari et al. 2007). In some situations, WWBs can modulate the development of twin TCs that are roughly symmetric about the equator (Lander 1990; Zhu et al. 2003).

Dickinson and Molinari (2002) showed that within the area of active convection associated with the MJO, mixed Rossby-gravity (MRG) waves can develop and serve as precursors to TCG. The MRG waves exhibit a westward vertical tilt because of the easterly vertical shear during the MJO (Frank and Roundy 2006). Dickinson and Molinari (2002) further found that deep convection prior to TCG develops not near the circulation center, but to its north. As the westward-tilted MRG waves

"transition" to tropical depression (TD) type waves, deep convection develops closer to their centers and they move northwestward away from the equator. The northward translation and "transition" of the incipient equatorial disturbances to off-equatorial TCs still remain mysteries central to the issue of TCG during the active MJO.

While the previous studies have established the relationship between the MJO, WWBs, and TCG, little is certain about the mechanisms by which they interact. Specifically, what is the importance of the associated WWB vortex, occurring at the synoptic scale, in initiating TCG? How is the low-level cyclonic circulation, which is necessary for triggering the wind-induced surface heat exchange (WISHE) processes (Emanuel 1986), initially generated from the large-scale flows? In this dissertation, we attempt to address these issues by examining the multi-scale processes involving the MJO, WWBs, mesoscale convective systems (MCSs), mesoscale convective vortices (MCVs), and convective scale processes during the genesis of Typhoon Chanchu (2006).

The purposes of Chapter 2 of this dissertation are to (i) document the evolution of large-scale conditions associated with Typhoon Chanchu, from its incipient to typhoon stage, using the National Centers for Environmental Prediction (NCEP) final analysis (FNL) at 1.0^{o} resolution and satellite observations; (ii) demonstrate that the general flow structures and organization of precipitation that comprise the genesis of Chanchu could be reasonably duplicated by an 11-day cloud-resolving simulation using the Weather Research and Forecast (WRF) model at the finest resolution of 2 km; and (iii) examine the evolution of the simulated westward-tilted vortex associated

with a WWB, hereafter the tilted WWB-vortex, that occurs prior to the genesis of Chanchu.

The next section provides an overview of the evolution of Chanchu in relation to the large-scale environment as well as the 2006 typhoon season and intraseasonal variability. Section 2.3 describes the configuration of the WRF model used for the present study. Section 2.4 compares the simulation results to available observations prior to the genesis of Chanchu. Section 2.5 shows the mechanisms by which the pre-Chanchu disturbance develops and evolves during the pre-genesis stage. A summary and concluding remarks are given in the final section.

2.2. Synoptic overview of Chanchu

2.2.1. TC activity in the Indian and West Pacific basins: Spring 2006

Chanchu was the second named TC of the 2006 Northern Hemisphere tropical season and the second to make landfall in Southeast Asia. The first TC, Cyclone Mala, developed in the Indian Ocean basin on 20 April and became what would retrospectively be the strongest TC of the 2006 TC season and the first category-4 cyclone of the 21st century in the Indian Ocean basin. The pre-Mala disturbance developed slowly as it tracked northwestward from near the northern tip of Sumatra into the open Bay of Bengal during 20 – 24 April (Fig. 2.1). Mala subsequently intensified in warm water (> 30ºC), reached peak intensity on 28 April, weakened slightly prior to landfall in Burma on 29 April, and accelerated northeastward over mainland China and into the open Pacific along the northern periphery of a subtropical ridge.

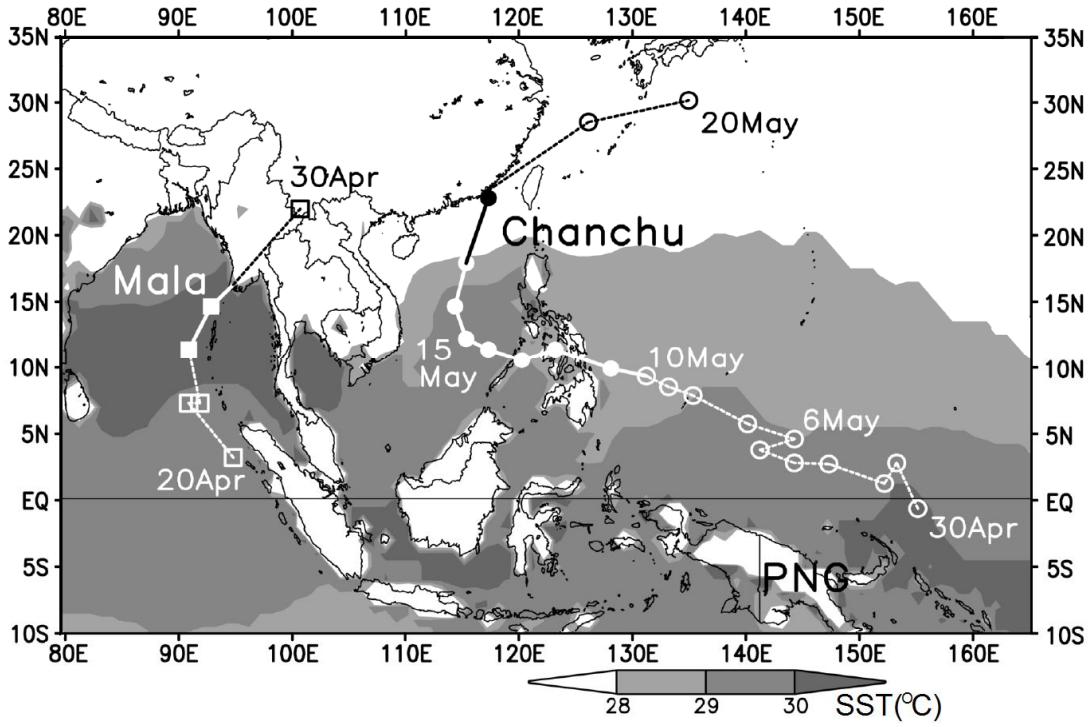

Figure 2.1. Observed track of Typhoon Chanchu (Cyclone Mala), marked at daily (two-day) intervals and based on the 900-hPa circulation center from NCEP's FNL during the period of 0000 UTC 30 April – 20 May (20 – 30 April) 2006. Filled symbols and heavy track lines represent the periods when the intensity exceeded category one hurricane equivalent. NCEP SSTs at the model initial time are shaded according to the gray scale. Symbol "PNG" denotes the location of Papua New Guinea.

As Mala completed its extratropical transition, an area of active equatorial deep convection northeast of Papua New Guinea, denoted by "PNG" in Fig. 2.1, spawned the pre-requisite disturbance on 30 April that led to the second named storm of the 2006 season, Typhoon Chanchu. The pre-Chanchu disturbance appears to have originated in the Southern Hemisphere and crossed the equator as it moved erratically northwestward (Fig. 2.1). After an 8-day incubation period, the pre-Chanchu disturbance began to organize on 7 May, received the designation of tropical depression on 8 May, and by 10 May it became a typhoon. Chanchu deepened slowly as it moved across the Philippine archipelago, and after entering the South China Sea on 13 May it deepened rapidly and became a super-typhoon on 15 May.

Subsequently, Chanchu turned sharply northward and accelerated toward mainland China. It weakened over the cooler water (Fig. 2.1) of the northern South China Sea prior to landfall late on 17 May and finally underwent extratropical transition as it merged with a midlatitude frontal system and the associated jet stream aloft. While the current chapter focuses on the formation of Chanchu, the next two subsections indicate that the near-equatorial formation of Mala two weeks prior to Chanchu was not necessarily coincidental. Their associated pre-genesis disturbances were closely associated with the active phase of the MJO.

2.2.2. Relationship between Chanchu and the MJO

For the purposes of this study, we use the term *pre-genesis* to refer to the period between the initial identification of a low-level (900-hPa) cyclonic circulation in the NCEP FNL and the official recognition of the system by the Joint Typhoon Warning Center (JTWC). The pre-genesis periods for Mala and Chanchu are shown schematically in Fig. 2.2 against the background of the MJO during April – May 2006. During this period, the MJO exhibited its well-known west to east propagation, from the Indian Ocean into the Pacific Ocean.

Fig. 2.2 shows that Mala and Chanchu, while developing in separate basins, both began pre-genesis during the convectively active phase of apparently the same MJO event. The pre-Mala disturbance developed first as a closed low-level circulation on 20 April near 100°E, at the peak of the active phase of the MJO in the Indian Ocean, and reached its depression stage as the equatorial Indian Ocean transitioned to the inactive phase of the MJO. During its pre-genesis stage, the pre-Mala disturbance translated west-northwestward under the influence of the easterly

trades. By 30 April, Mala intensified into a destructive cyclone in the Bay of Bengal, as the MJO propagated eastward into the West Pacific along with its enhanced equatorial deep convection.

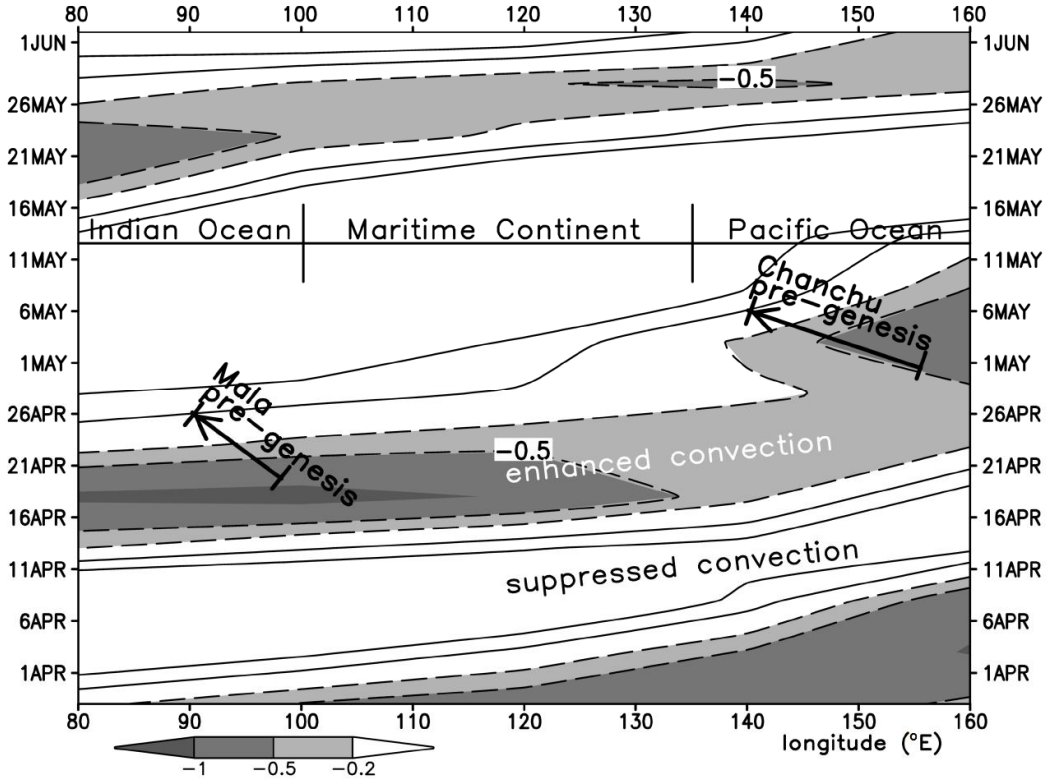

Figure 2.2. Hovmöller diagram of the observed (5-day) mean MJO index from 27 March to 2 June 2006 for the equatorial region spanning from 80°E to 160°E. Positive (negative) magnitudes are plotted using solid (dashed) contours at intervals of ±0.2 and 0.5 and represent convectively inactive (active) periods. Convectively active periods are shaded according to the gray scale. The pre-genesis periods of Chanchu and Mala are marked by the heavy arrows. Data source: www.cpc.ncep.noaa.gov/products/precip/CWlink/daily_mjo_index/mjo_index.html.

On 30 April, the pre-Chanchu disturbance emerged near 155°E during the MJO's local peak conditions (Fig. 2.2), moved west-northwestward during pre-genesis, and became a depression during the transition period between the active and inactive MJO. The precursors associated with Mala and Chanchu appeared to persist as weak but coherent low-level disturbances for 5 and 8 days, respectively, prior to

being classified as tropical depressions. It is likely that the slowly evolving MJO helped maintain the two weak disturbances (Liebmann et al. 1994). While the pre-Mala and pre-Chanchu disturbances both developed during the active phase of the MJO, their geneses occurred as the MJO weakened (Fig. 2.2). Thus, the active phase of the MJO could not be considered as sufficient for TCG, but only favorable for the development and maintenance of the pre-Mala and pre-Chanchu disturbances.

2.2.3. Pre-genesis of Chanchu

Enhanced deep convection and WWBs are well-known accompaniments to the MJO in the near-equatorial region. Fig. 2.3 shows the synoptic setup at the 600- and 900- hPa levels during the pre-genesis and genesis stages of Chanchu, i.e., from 0000 UTC 28 April – 0000 UTC 8 May 2006. A subtropical high-pressure system dominated the WNP, with the easterly winds spanning the basin except in the vicinity of the equator. As early as 28 April, Fig. 2.3g shows a WWB situated on the maritime continent, extending eastward to PNG. Convergence of the WWB and the easterly trades led to enhanced cloud cover along their northwest-southeast oriented interface (see Figs. 2.4a,b) with an inverted trough (see the dashed lines in Fig. 2.3g) just east of PNG in advance of the WWB. The 900-hPa trough amplified as the WWB intensified to exceed 10 m s^{-1} and progressed eastward to nearly 160°E, and by 30 April a closed cyclonic vortex developed to both the north ("C") and south ("L") of the WWB (Fig. 2.3h). By 2 May, two cyclonic vortices ("L") had developed south of the equator (Fig. 2.3i). Note that the two southern vortices resulted from the split of the WWB as it crossed the rugged terrain of PNG. Though the focus of the current chapter is the development of the northern vortex into Chanchu, it is noteworthy that

the PNG landmass sits entirely in the southern hemisphere, and it likely disrupted the formation of a coherent mirror image vortex to that which formed in the northern hemisphere by 2 May.

A northwest-southeast oriented trough also appeared at 600 hPa on 28 April (Fig. 2.3a) in advance of the WWB, but it was located about 1000 km to the west of the 900-hPa trough. By 2 May, two 600-hPa cyclonic circulations also appeared approximately symmetric on the north and south sides of the WWB (Fig. 2.3c). Because the highest mountain on the island (i.e., Puncak Jaya) has an elevation of 4884 m, the WWB at 600 hPa showed little evidence of splitting. Note that the center of the north-hemispheric circulation at 600 hPa appeared as if it were spatially disjointed westward from its 900-hPa counterpart (cf. Figs. 2.3c, i), and that the WWB at 900 hPa extended much farther eastward than that at 600 hPa on 2 May. As will be shown in the next subsection, the two vortices are physically related in the vertical.

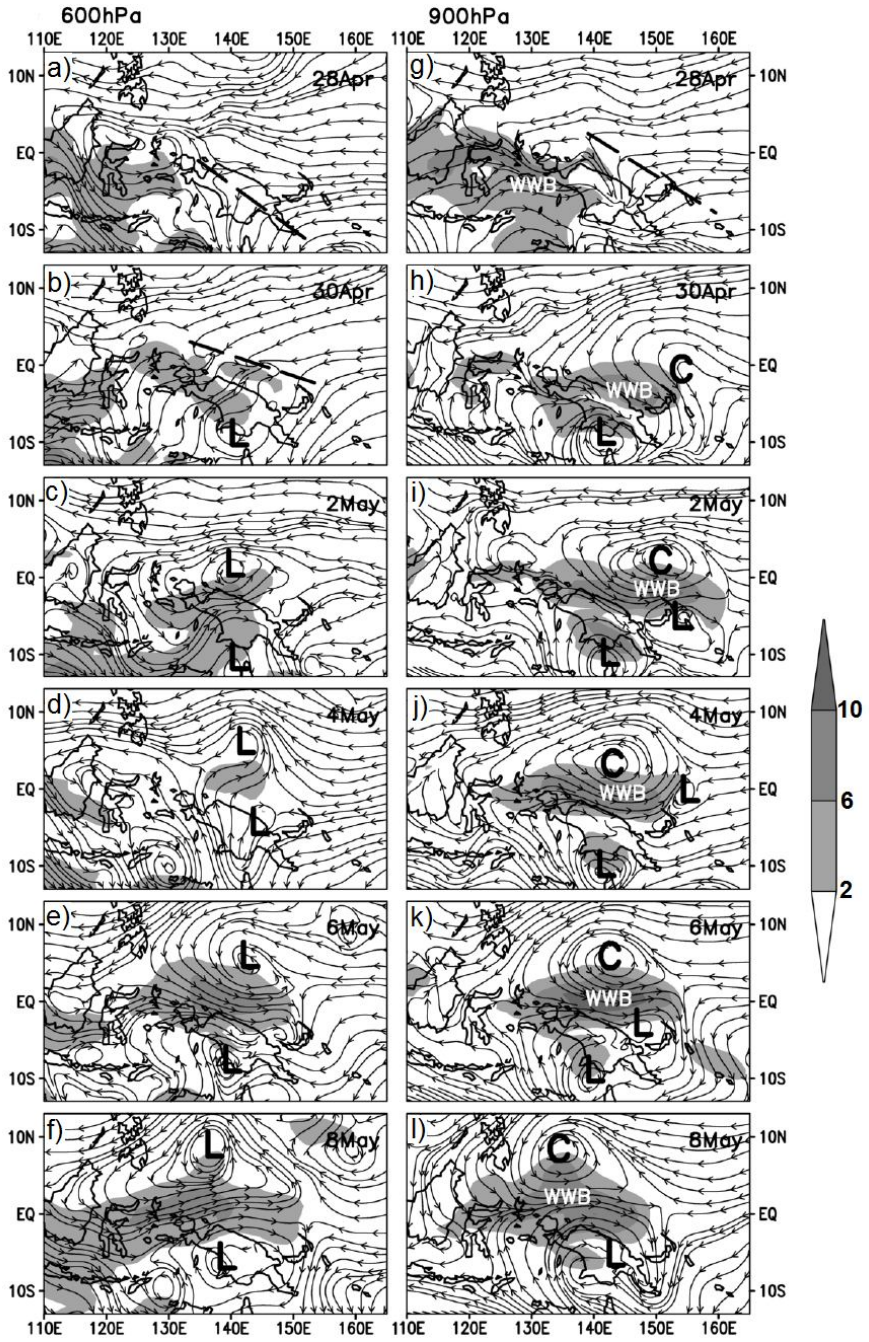

Figure 2.3. Distribution of horizontal streamlines, obtained from NCEP's FNL, with the westerly winds (m s^{-1}) shaded in (a) – (f) at 600 hPa (left panel), and in (g) – (l) at 900 hPa (right panel) during the period of 0000 UTC 28 April (top) – 0000 UTC 8 May (bottom) at 2-day intervals. Letter "C" highlights a closed 900-hPa circulation associated with Chanchu, and "L" denotes other closed cyclonic circulations. Symbol "WWB" in the right panel denotes the westerly wind burst, and heavy lines represent trough axes of interest. Fields are averaged within a ± 6-h period and a ± 50-hPa layer.

During the period of May 2 – 6, the 600-hPa circulation moved slowly northeastward (Fig. 2.3c-e), while the 900-hPa vortex moved northwestward (Figs. 2.3i-k). The northwestward movement of such low-level pre-TC disturbances during active MJO periods has been shown by Maloney and Hartmann (2001) and other studies. Because of their differing translations during 2 – 6 May, the horizontal distance between the two vortex centers diminished to nearly zero by 6 May, after which they moved northwestward as a vertically stacked vortex (Figs. 2.3f,l). The subsequent rapid convective organization and TCG after the two vortices were vertically locked in phase is evident on May 10 (see Fig. 2.4g). In fact, Chanchu reached near typhoon strength on this date.

Though the MJO appeared to propagate smoothly eastward (Fig. 2.2), the WWB exhibited a different evolution. That is, the intensifying WWB surged first rapidly eastward during 28 April – 2 May, resulting in the formation of the pre-Chanchu disturbance at 900 hPa, but it retreated northwestward during 2 – 8 May (Figs. 2.3i-l). This behavior is similar to the MJO composites shown by Kim et al. (2008) and other studies. Thus, the evolution of the WWB shown in Fig. 2.3 could be considered typical, although the mechanisms responsible for the northward movement of the MJO are still not well understood. While we do not address this issue herein, it is of interest that because only the northern vortex intensified (and the southern one weakened due likely to the landmass blocking), its subsequent northwestward translation could give the appearance of the northwestward translation of the WWB.

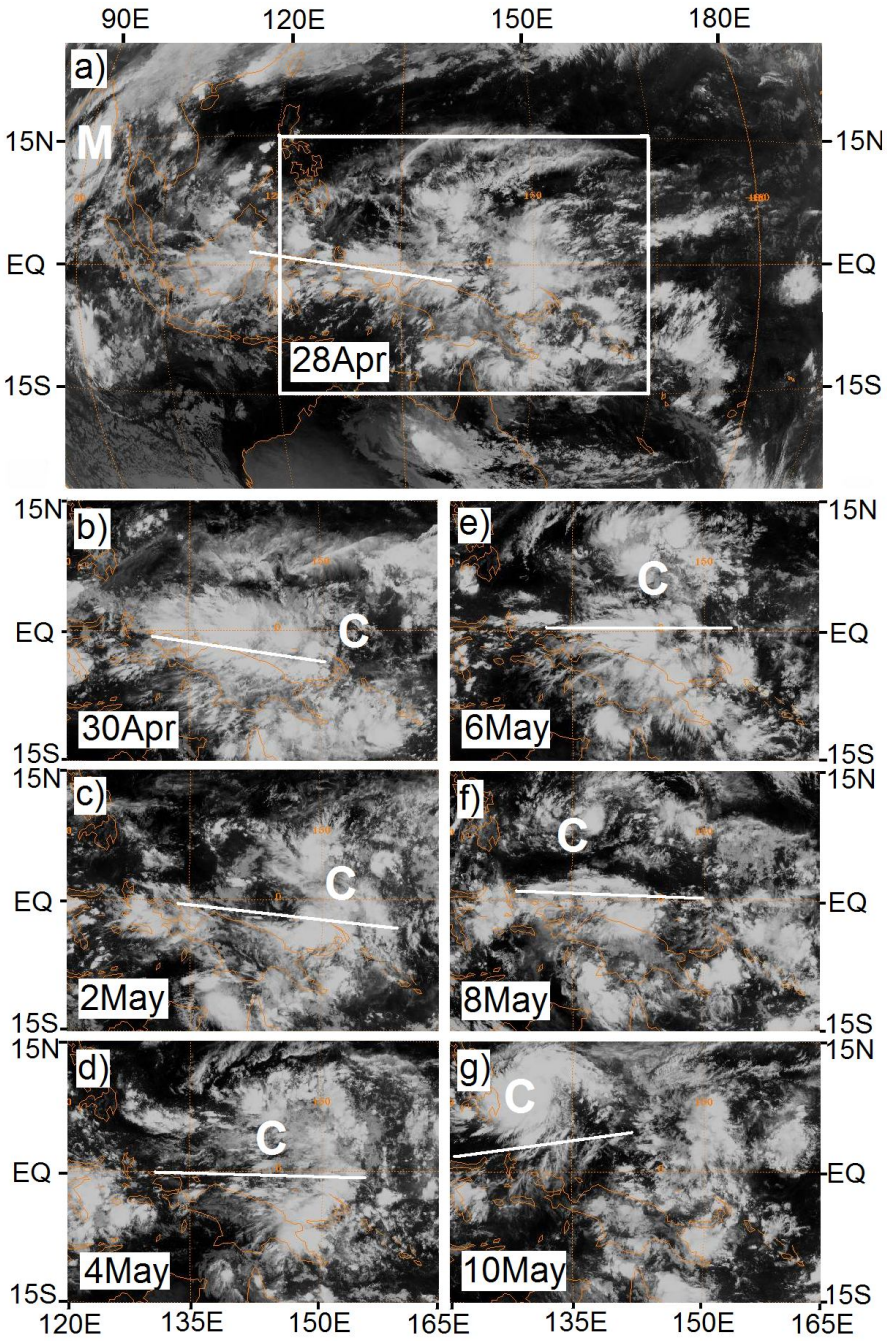

Figure 2.4. Cloud fields as viewed from the MTSAT satellite infrared channel (10.3 – 11.3 μm) at 2-day intervals from 0000 UTC 28 April (a) – 10 May (g) 2006. The box in (a) denotes the region containing the pre-Chanchu disturbance (marked by a "C" during 30 April – 10 May), and the solid line in (a) – (g) denotes the axis of the WWB at 900 hPa. In (a), Cyclone Mala (marked by "M") is shown just prior to its landfall on 28 April. Data source: http://www.ncdc.noaa.gov/gibbs/

As the eastward-moving WWB increased its intensity during 28 April – 2 May, the pre-Chanchu disturbance amplified due likely to the well-known mechanisms of barotropic eddy kinetic energy conversions (Maloney and Hartmann 2001) and wave accumulation (Sobel and Maloney 2000). Once a closed vortex developed (i.e., after April 30), it could persist due to the same mechanisms, plus the continuous deep convection in its vicinity (Fig. 2.4). The pre-Chanchu disturbance did not undergo TCG, however, until it finally ejected poleward of 5°N by 7 May, while the southern disturbance remained in close proximity to PNG and weakened with time (see Figs. 2.3f and 2.3l).

2.2.4. Mean structure of the MJO

Fig. 2.5 shows the composite structures of the WWB and its associated dual (actually triple) vortices that occurred during the pre-genesis phase of Chanchu. Note that the peak mean WWB occurred near 2°S. One could expect the development of twin vortices symmetrically located in each hemisphere if the WWB were symmetric about the equator. But with the mean WWB shown in Fig. 2.5, the southern vortex development should be dynamically favored due to the presence of a larger Coriolis force. However, as discussed earlier, the southern vortex developed in the vicinity of a large landmass, which tended to disrupt intensification. Evidence of the second southern vortex can be seen near 10ºS (Fig. 2.5) in association with the southern (and weaker) split of the WWB. Further, the northward movement of the WWB at later stages favored the northern vortex. So in extraordinarily fortuitous situations twin TCs could develop and exhibit a mirror image about the WWB (e.g., see Zhu et al. 2003), but the present case is not such a scenario due to the large landmass and the

northward movement of the WWB that inhibited the southern vortices. Clearly, the MJO, through enhanced low-level confluence (see "X" symbols marked in Fig. 2.5) associated with the WWB, barotropic eddy growth, and northward movement into the open ocean, created an environment that was favorable for TCG in the northern hemisphere.

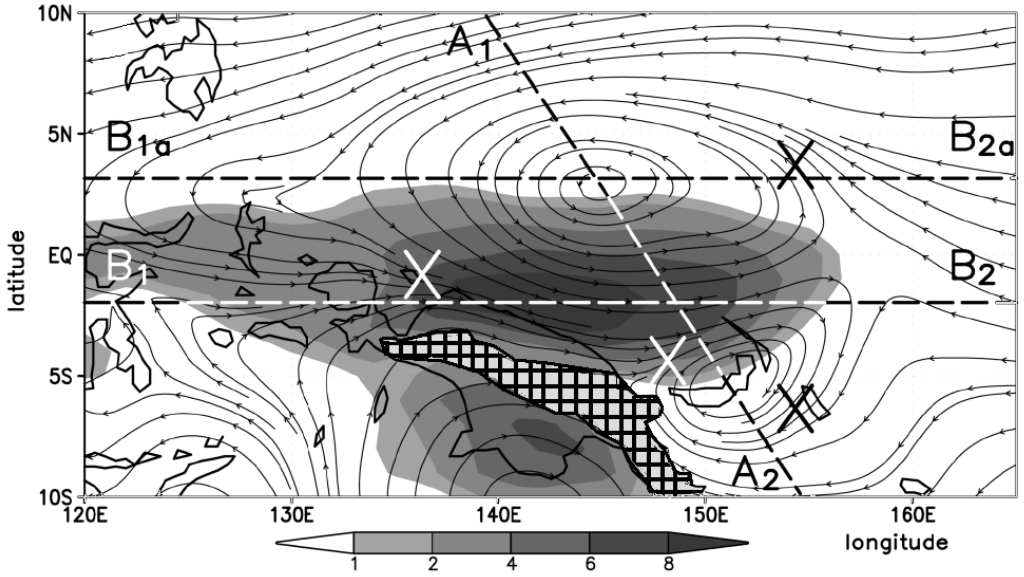

Figure 2.5. The 900 – 800 hPa layer-mean horizontal streamlines, with the westerly flows shaded (m s^{-1}), that are averaged during the period of 30 April – 5 May 2006 from NCEP's FNL. Lines $A_1 - A_2$, $B_1 - B_2$, and $B_{1a} - B_{2b}$ represent the paths of the vertical cross sections, shown in Fig. 2.6, through the centers of the quasi-symmetric cyclonic vortices, along the axis of the WWB, and through the pre-Chanchu vortex, respectively. Symbol "X" marks the areas of obvious low-level confluence, and areas of underneath terrain are hatched.

Fig. 2.6 shows the across- and along-flow vertical structures of the WWB. Across the WWB (Fig. 2.6a), easterly winds dominated the WNP basin, except for the WWB that was confined below 500 hPa with the peak magnitude near 900 hPa. Associated with the WWB were the two lower-tropospheric cyclonic vortices exhibiting peak magnitudes at the interface of the westerly and easterly flow. An along-WWB vertical cross section clearly shows a westward tilt of the WWB with

height (Fig. 2.6b). At 900 hPa, the leading edge of the WWB extended to near 158°E, but only to 138°E at its uppermost location. The westward vertical tilt explains the development of a closed 600-hPa circulation (Fig. 2.3e) over 1000 km to the west of the 900-hPa counterpart. The coherent vorticity structure north of the WWB (Fig. 2.6b) suggests that *the two circulations (i.e., at 900 and 600 hPa) could be considered as part of the same vertically-tilted vortex*, which developed in the presence of large scale easterly vertical shear (Fig. 2.6b). Note that the converging zonal winds at the leading edge of the WWB (Fig. 2.6b) favored wave accumulation, as will be discussed in section 2.5 in the context of the formation of the pre-Chanchu vortex.

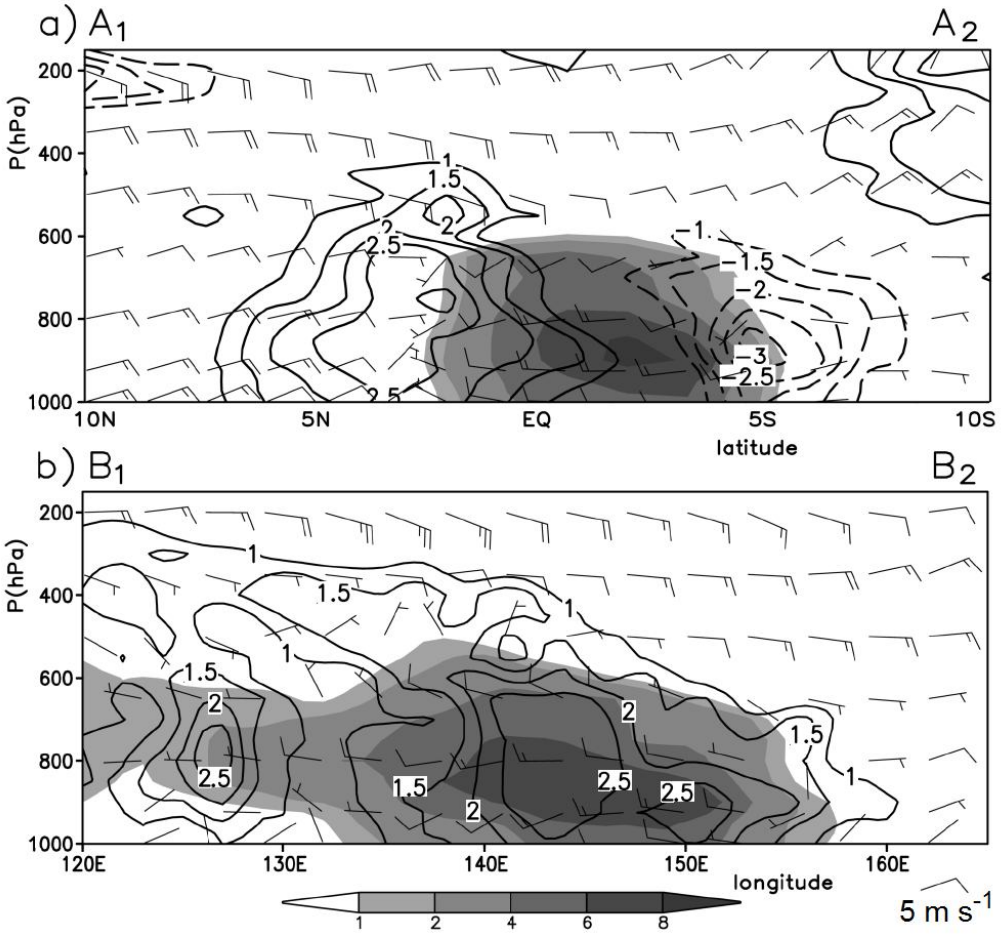

Figure 2.6. Vertical cross sections of horizontal wind barbs (a full barb is 5 m s^{-1}) and the vertical relative vorticity (contoured at intervals of ±1, 1.5, 2, 2.5, and 3 x 10^{-5} s^{-1}), as shown in Fig. 2.5, with westerly flows shaded (m s^{-1}), that are taken (a) across the composite WWB (i.e., lines $A_1 - A_2$), and (b) along the axes of the WWB (lines $B_1 - B_2$) and through the pre-Chanchu vortex (line $B_{1a} - B_{2b}$). Solid (dashed) contours denote positive (negative) relative vorticity, and only the positive values in (b) are shown. Note that in (b) only the relative vorticity field is taken along ($B_{1a} - B_{2b}$) in order to show the WWB-associated vorticity field. Fields are calculated as a five grid point slice-average.

In summary, the development of Chanchu could be traced back more than a week prior to its classification as a depression. It formed at the leading portion of the WWB associated with the eastward propagation of the MJO, and its associated vortex exhibited a westward tilt in the vertical. The ongoing processes during this pre-genesis period, particularly those non-observable from the large-scale analyses, are the subject of many unanswered questions about TCG. The subsequent sections describe a cloud-resolving simulation of this pre-genesis portion of Chanchu that is performed to replicate the above-observed evolution and attempt to gain insight into the processes by which the vertically tilted WWB-vortex could transition into an intense typhoon.

2.3. Model description

The current study utilizes Version 2.2 of the Advanced Research WRF (WRF-ARW, Skamarock et al. 2005) to simulate for a period of 11 days the pre-genesis and genesis of what would eventually become Super Typhoon Chanchu (2006), at the finest cloud-resolving resolution of 2 km. The model physics schemes used include (i) the Lin et al. (1983) cloud microphysics scheme (Tao et al. 1993), which contains six classes of water substance (i.e., water vapor, cloud water, rain, snow, graupel, and cloud ice); (ii) the Yonsei University planetary boundary layer (PBL)

parameterization with the Monin-Obukhov surface layer scheme (Hong et al. 2006); (iii) the rapid radiative transfer model (RRTM) for long waves with six molecular species (Mlawer et al. 1997) and the Dudhia scheme for shortwave radiation; and (iv) a modified version of the Kain-Fritsch (1993) cumulus parameterization scheme for the outer 3 domains in which deep convection and a broad range of shallow convection are both parameterized. Note that no cumulus parameterization is used in the 2-km resolution domain.

Fig. 2.7 shows schematically the WRF model setup, which consists of a quadruply-nested telescoping configuration. Three stationary outer domains A, B, and C have the (x, y) dimensions of 100 × 134, 175 × 136, and 313 × 235 grid points with the grid lengths of 54, 18, and 6 km, respectively; and a moving inner domain D with dimensions of 301 × 301 grid points is used to follow the center of Chanchu at the grid length of 2 km. All domains have 40 vertical sigma levels, and they are 1, 0.993, 0.983, 0.97, 0.954, 0.934, 0.909, 0.88, 0.814, 0.753, 0.695, 0.641, 0.590, 0.542, 0.497, 0.455, 0.416, 0.379, 0.345, 0.313, 0.283, 0.256, 0.230, 0.206, 0.184, 0.163, 0.144, 0.126, 0.110, 0.095, 0.081, 0.069, 0.057, 0.047, 0.037, 0.028, 0.020, 0.013, 0.006, and 0. The model top is defined at 30 hPa.

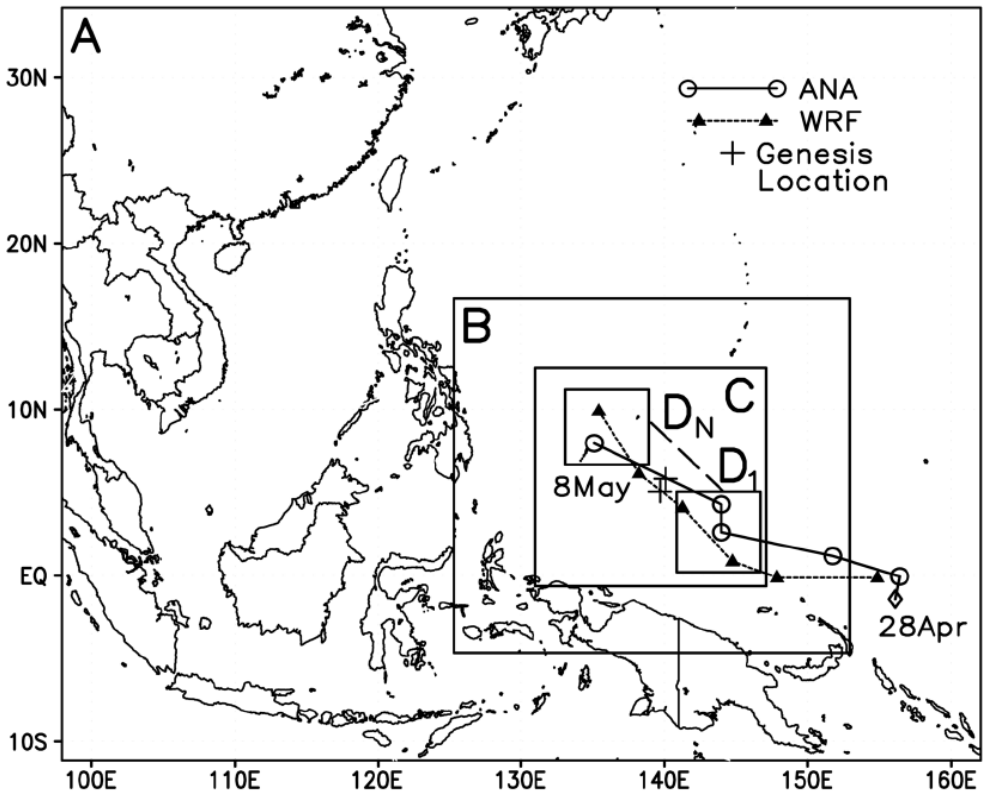

Figure 2.7. Configuration of the nested WRF model domains. Domains A, B, and C remain fixed, while domain D moves with the storm along the dashed line between D_1 and D_N. The observed (solid with open circles) and simulated (dotted with filled triangles) tracks are shown at 2-day intervals from 28 April to 08 May 2006. The observed April 28 marker is diamond-shaped to denote the absence of a closed circulation, and it is placed at the location of peak vorticity near the 900 hPa trough. Symbols "+" along each track denote the approximate location of Chanchu's genesis.

The integration proceeds via a staggered initiation of the nested domains, in which Chanchu is allowed to spin up within each domain before a new domain is initiated. The simulated Chanchu is not permitted to cross the boundary of any nest at any time, and care is taken to prevent the initialization of any nest when precipitation is occurring near the boundaries. The outermost domain (A) is initialized at 0000 UTC 27 April 2006. Domain B begins 4 days later, i.e., at 0000 UTC 1 May. Domain C is activated at 1200 UTC 2 May, and domain D 12 h later at 0000 UTC 3 May. The 11-day simulation is chosen to capture different stages of the genesis of Chanchu,

including the earliest large-scale formation of a WWB associated with the MJO (domain A), the mesoscale pre-genesis (domains B and C), and the storm-scale genesis (domain D). Due to the two-way interactive nature of the nests, we may use only the results from domain A to examine the large and mesoscale flows in Chapter 2 without losing the upscale influences of deep convection and the small-scale processes, which we reserve for subsequent studies.

The model initial conditions and the outermost lateral boundary conditions are obtained from the NCEP FNL with the latter updated every 6 hours. No artificial data (e.g., bogus vortices) are used during the 11-day model integration. Sea-surface temperatures (SSTs) are updated daily using NCEP's data (see Fig. 2.1 for the initial SST distribution), though there is no significant TC-induced variation in SSTs during the simulation, as the disturbance remains weak. Note that the outermost domain A is allowed to spin up from the raw initial conditions, in which the WWB has not yet moved across PNG and the pre-Chanchu disturbance has not yet developed into a closed circulation at any vertical level.

2.4. Model verification

In general, it is not surprising that the WRF model could reproduce well the large-scale features. Thus, in this section we compare the 11-day WRF simulation to available observations of the track, intensity, and some major structures of the pre-Chanchu disturbance. Fig. 2.7 shows that the model reproduces reasonably well the observed track, which was obtained by taking the location of the 900-hPa circulation center from the NCEP FNL prior to Chanchu's depression stage and the JTWC's best track analysis afterward. The simulation captures the formation of a low-level

disturbance evident on 28 April near the equator at 155°E, and its subsequent west-northwestward translation up to May 8.

While the observed disturbance remains quasi-stationary for about 2 days (i.e., April 28-30), the simulated disturbance moves immediately westward. On 2 May, the simulated near-equatorial disturbance is displaced about 800 km to the west of the observed. After 2 May, both the simulated and observed disturbances begin to move northwestward away from the equator, in concert with the WWB (cf. Figs. 2.7 and 2.3), until the end of the 11-day simulation on 8 May. At the final time, the simulated storm exhibits a track error of roughly 200 km northward compared to the observed. Despite these differences, especially for the premature westward translation, we may claim that the WRF model reproduces reasonably well both the formation near the equator and subsequent movement of the pre-Chanchu disturbance for a period of 11 days. This indirectly confirms that the larger-scale flows, in which the weak disturbance evolves, are reasonably simulated.

The JTWC began to estimate the intensity of the pre-Chanchu disturbance on May 7, and their report suggests that the minimum pressure remains above 1000 hPa until 8 May (not shown) when the observed storm could be classified as a tropical depression. Fig. 2.8 shows that the simulated storm intensity remains nearly constant, with minimum pressure above 1000 hPa during the first 8-day (or 192-h) period, when few observations were available. However, it begins to intensify after the 192-h integration, valid at 0000 UTC 5 May (hereafter 5/00-192), which is more than 2 days earlier than the observed. This simulated early intensification is likely associated with its early west- and northwestward translation during the period of

May 2 – 6 (Fig. 2.7), when the simulated storm reaches its genesis position two days prior to that observed. Nevertheless, the geneses of the observed and simulated storms occur at nearly the same position (i.e., near 140°E, 5°N; see Fig. 2.7). Thus, we may assume that the WRF model also reproduces reasonably well the evolution of the storm intensity during the pre-genesis stage.

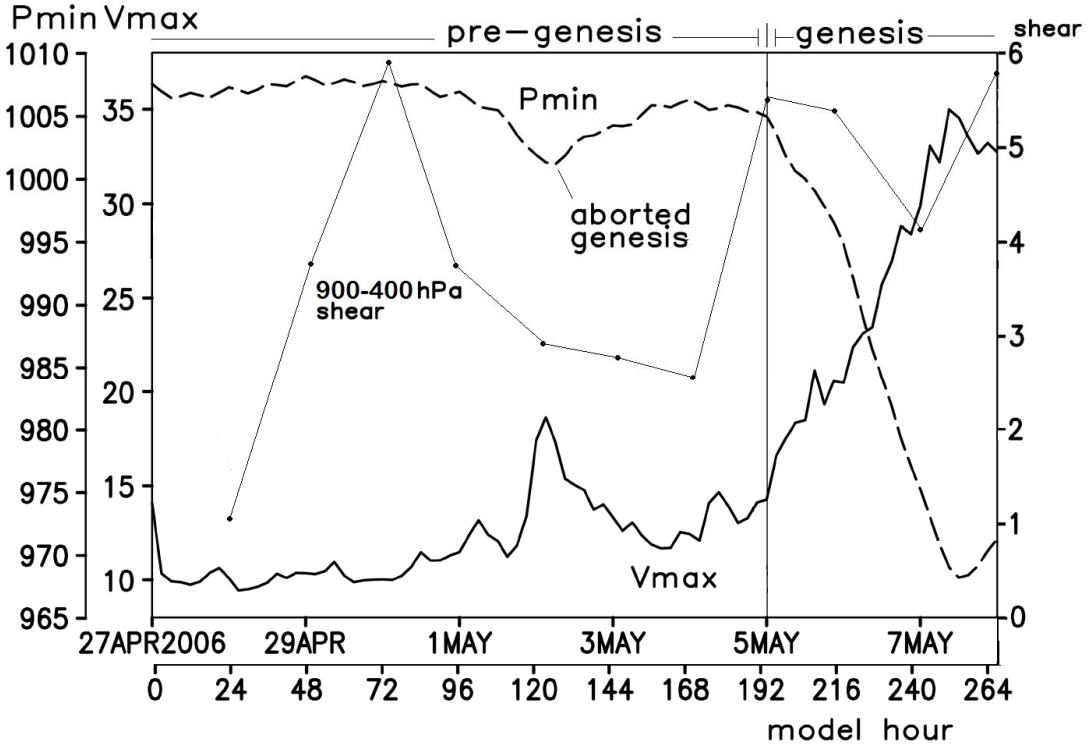

Figure 2.8. Time series of the minimum central pressure (P_{min}, hPa, dashed) and the maximum surface winds (V_{max}, m s^{-1}, solid) at 3-h intervals, from the 11-day (i.e., 0000 UTC 27 April – 0000 UTC 8 May 2006) simulation in Domain A. An area of 1600 km × 1600 km-too large?? is used to estimate the vertical wind shear between 400 and 900 hPa at daily intervals, centered on the 900-hPa circulation center. The thin solid vertical line at 0000 UTC 5 May demarcates the pre-genesis and genesis periods.

Note that the simulated intensity changes, shown in Fig. 2.8, can be clearly divided into two distinct stages, i.e., pre-genesis and genesis stages. During the pre-genesis stage (i.e., April 27 – May 5), the minimum central pressure (P_{min}) fluctuates between 1000 – 1007 hPa, and the maximum surface wind (V_{max}) fluctuates between

10 – 13 m s^{-1}. A noteworthy exception during the pre-genesis stage is a near-equatorial *aborted genesis episode*, i.e., a temporary intensification and subsequent weakening before and after 2/00-120, respectively (Fig. 2.8). It is well known that TCG cannot occur near the equator due to the lack of the planetary vorticity for vortex stretching, but as will be shown in section 2.5, TCG can *temporarily* occur at this time because of increasing deep convection near the center of the pre-Chanchu vortex. The *sustained* intensification stage begins at 5/00-192, which marks the end (beginning) of the pre-genesis (genesis) stage. Subsequently, the storm deepens until 7/12-252 with a 36-hPa drop in P_{min} and an increase in V_{max} to about 35 m s^{-1}, just reaching typhoon intensity.

An examination of the large-scale vertical wind shear (VWS) in the 900 – 400 hPa layer indicates that the synoptic environment in which the pre-Chanchu disturbance develops remains relatively quiescent (see Fig. 2.8), with VWS fluctuating between 2 - 6 m s^{-1} during pre-genesis and genesis. Note that a much larger area average than that typically used in previous studies is used here because of the large tilt of the WWB-vortex. The VWS during the early stages of pre-genesis is easterly because the 400-hPa flow over the equatorial region remains easterly (see Fig. 2.6) while the low-level WWB surges eastward. During the later stages of pre-genesis, the VWS shifts to westerly (not shown) due to preferential enhancement of low-level easterly winds in the northern semicircle of the circulation, associated with convection there. Generally, large-scale VWS remains weak and favorable for TCG, especially during the aborted genesis.

Because direct observations of the storm intensity during pre-genesis are not available, we compare in Fig. 2.9 the simulated sea-level pressure and the vertically-integrated cloud hydrometeors to the NCEP FNL and the satellite-observed outgoing longwave radiation (OLR) during the 11-day integration period. On 30 April, the model produces a loosely closed isobar of 1009 hPa at the equator - a surface manifestation of the pre-Chanchu disturbance, with dense cloud coverage near the circulation center (Fig. 2.9d). Though the simulated circulation translates to the west faster than the observed (cf. Figs. 2.9a and 2.9d), as also indicated in Fig. 2.7, the model does capture the large area of cloud coverage observed to the north and west of the circulation as well as the cloud-free region to the southeast. Since the easterly trades increase with height (Fig. 2.6b), the upper-level hydrometeors tend to be advected downstream of the low-level convergence zone, forming a large area of stratiform clouds and precipitation to the northwest of the vortex (cf. Figs. 2.9d and 2.5).

Note that while the observed 900-hPa wind fields show closed circulations (denoted by "C" and "L" in Figs. 2.9a-c), there are no associated closed surface isobars for either the pre-Chanchu or the southern hemispheric disturbance on 4 May (cf. Figs. 2.3i and 2.9b). Such a poor correspondence between the wind and mass fields is common over the equatorial area. Both the observed (Fig. 2.9b) and simulated (Fig. 2.9e) maximum cloud coverage shifts from the western to the northern portion of the vortex during 30 April – 4 May. Meanwhile, a cloud-free area develops to the south, suggesting large-scale dry intrusion and subsidence to the south of the vortex. Although the southern vortex evolves in close proximity to land with

little intensity changes, the simulation captures well its associated cloud field on 4 May (Fig. 2.9e).

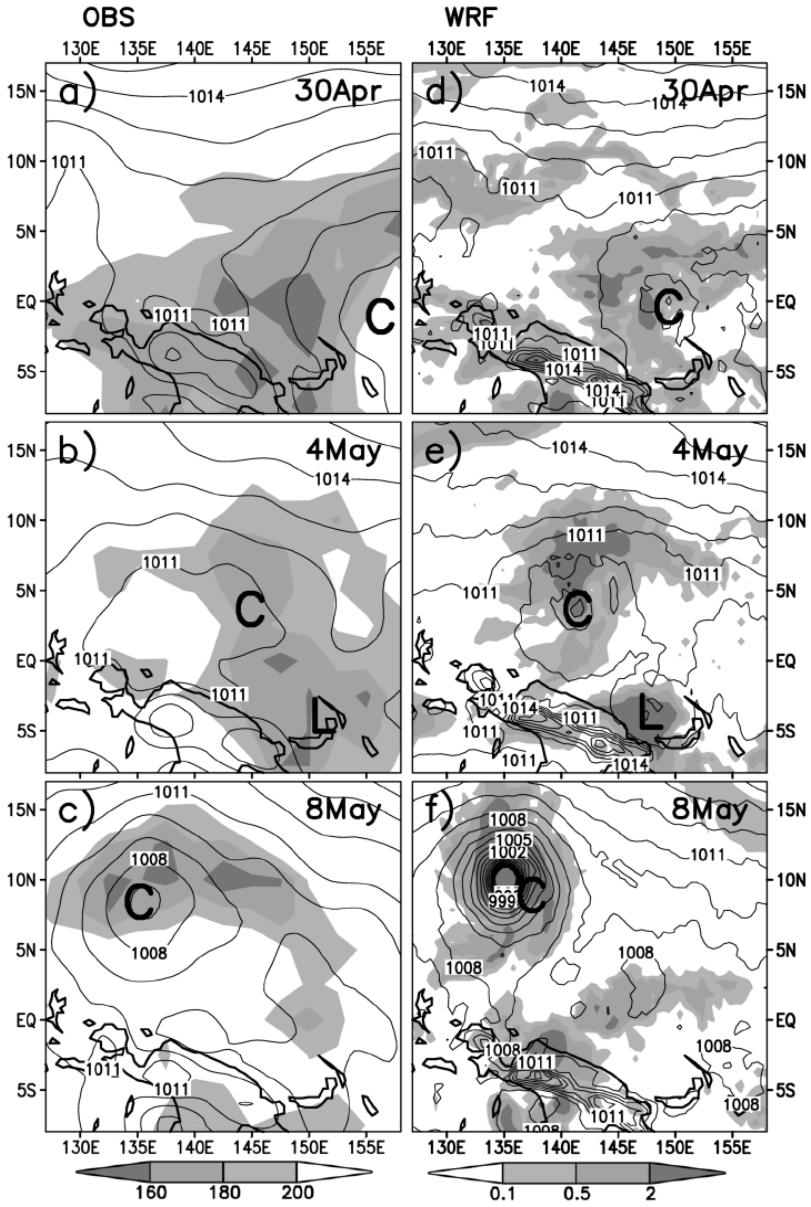

Figure 2.9. Comparison of (a) – (c) the observed outgoing long-wave radiation (OLR, W m^{-2}, shaded left panel) at the top of cloud columns to (d) – (f) the simulated vertically mass-weighted cloud hydrometeors (g kg^{-1}, shaded, right panel), and superimposed with contours of the sea-level pressure (every 1 hPa) at four-day intervals during the period of 0000 UTC 30 April (top) – 8 May (bottom) 2006. Fields in (d) – (f) are averaged during a 12-h period. OLR data source: ftp://ftp.cdc.noaa.gov/Datasets/interp_OLR/olr.day.mean.nc

By 8 May both the observed and simulated storms exhibit easily identifiable centers in the sea-level pressure fields as they eject poleward and continue to intensify. The simulated Chanchu is much more intense than the observed on 8 May due to its premature intensification. However, despite the differences in intensity and some differences in the cloud coverage between the simulation and observations, their general agreements lends credibility to the 11-day simulation of the larger-scale environment.

2.5. Formation and evolution of the pre-Chanchu vortex

In this section we discuss in chronological order the formation of the closed pre-Chanchu circulation, the implications of the vertical tilt, the processes associated with the aborted genesis, and finally the transition of the tilted WWB-vortex to an upright TC.

2.5.1. The formation of a closed TC circulation

Understanding the origin of low-level disturbances is a challenging problem, and thus most TCG studies focus only on the amplification of pre-existing disturbances. In the present case, the eastward progression of the WWB appears to account directly for the formation of the pre-Chanchu disturbance. Although the MJO owes its existence to large-scale deep convection, the WWB and its associated vortices can be maintained in the absence of deep convection, at least within this regional simulation. This is confirmed by a sensitivity simulation in which the effect of latent heating is turned off, hereafter referred to as the DRY run, while holding all the other conditions identical to the control run shown in section 2.4. It is found that

the incipient disturbance in DRY forms at nearly the same location as that in the control run, but it fails to intensify (not shown), as expected.

To help visualize the formation of the pre-Chanchu disturbance, Fig. 2.10 shows a 3-day (i.e., 27/06-06 - 30/06-78) window of the simulated low- and mid-level flows in the vicinity of the WWB. In general, the model captures the eastward progression of the WWB (Figs. 2.10e-h), an inverted trough at both 600 (Fig. 2.10a) and 900 hPa (Fig. 2.10e), and the eventual development of closed circulations during this 3-day period (Figs. 2.10d,h). Note that the inverted trough is already present in the model initial conditions due to the preexistence of the WWB (not shown), but it is quite weak. Note also that a short easterly wave (SW) approaches the WWB-related trough axis from the east at 28/06-30 (Fig. 2.10f). According to Chang and Webster (1990), any wave approaching a major trough tends to congregate its associated cyclonic vorticity at the trough axis, serving to amplify the trough. This phenomenon is apparent between 28/06-30 and 29/06-54 (Figs. 2.10f,g) as the SW approaches the primary trough axis from the east.

Figs. 2.10i-l show at higher time resolution the formation of the closed circulation at 900 hPa, which develops by 29/03-51 to the northeast of PNG where the SW merges into the preexisting trough axis. This suggests that *the initial closed circulation in the lower troposphere forms through the wave accumulation process*. While deep convection may contribute to the SW intensity at earlier times, it is not essential for the formation of the low-level closed circulation since it also occurs in the DRY simulation (not shown). As the WWB continues to penetrate eastward, the incipient 900-hPa disturbance progresses west-northwestward under the influence of

the easterlies, with precipitation concentrated to the northwest of the 900-hPa center (Fig. 2.10h).

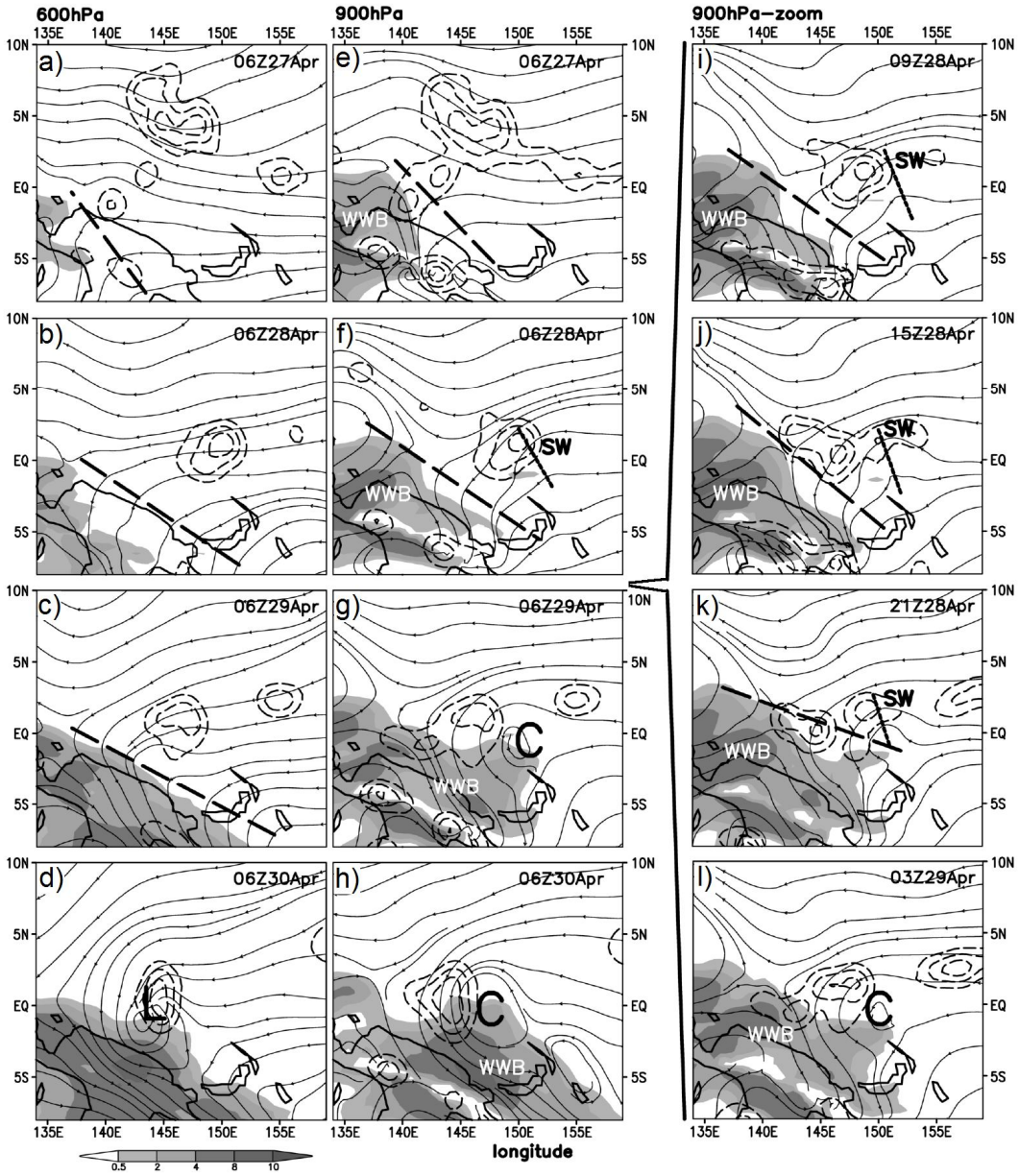

Figure 2.10. As in Fig. 2.3 for the two left panels (a) – (h), but with radar reflectivity (dashed contours at 5, 15, 25 dBZ) from 0600 UTC 27 (top) to 0600 UTC 30 (bottom) April 2006 at daily intervals. In the right panel, as in (e) – (h), but at 6-h intervals during 0900 UTC 29 (i) – 0300 UTC 30 April (l). Heavy dashed (dotted) diagonal lines denote major trough (short wave, SW) axes. Symbols "C" ("L") represent pre-Chanchu closed circulations at 900 hPa (600 hPa). Fields in the left panels (right panel) are averaged during a ±6-h (3-h) period.

Although the SW does not show a clear signal in the 600-hPa streamlines (cf. Figs. 2.10b and 2.10f), its precipitation field approaches the preexisting trough axis in a manner similar to that at 900 hPa but at a later time. That is, a closed cyclonic circulation does not occur at 600 hPa until 30/06-78 (Fig. 2.10d), which is 21 h later than that seen at 900 hPa due to the phase difference between the two levels. Both circulation centers develop roughly on the equator (Figs. 2.10d,h). In the DRY simulation, an inverted trough exists at 600 hPa at 30/06-78, but it does not exhibit a closed circulation (not shown). Thus, the distribution of a large area of mostly stratiform precipitation near the trough axis (Fig. 2.10d) suggests an important role of midlevel convergence in stretching the preexisting vorticity for the formation of the pre-Chanchu vortex. This will be detailed in Chapter 3.

2.5.2. Effects of the vertically tilted vortex -on convective development??

An important characteristic of the tilted WWB-vortex is that significant upward motion occurs exclusively to the northwest of the vortex, i.e., to the right of the tilt, in association with convective precipitation there (Fig. 2.10h). Among numerous studies of TCG associated with the MJO, little attention has been given to the impact of the vertical tilt of the WWB-vortex on TCG. In this regard, we may invoke the idealized TC modeling study of Jones (1995), who showed that vertically tilted barotropic TC-like vortices tend to induce negative (positive) potential temperature anomalies (θ') on the downtilt (uptilt) side such that cyclonic flows must ascend (descend) isentropically on the downtilt-right (-left) side of the vortex. Her study suggests that in the real atmosphere precipitation should be favored on the downtilt-right side of the vortex. This result is distinct from that of mature TCs which exhibit enhanced

upward motion on the downshear side (Zhang and Kieu 2006) and more clouds and precipitation on the downshear left side (Frank and Ritchie 1999; Black et al. 2002).

Despite the different horizontal scales, formation mechanisms, and degree of vertical tilt (i.e., the aspect ratio) compared to Jones' study (i.e., near the equator where conventional balanced dynamics may not apply), Fig. 2.11 shows that the pre-Chanchu vortex generally adheres to the tilted-vortex dynamics conceptualized by Jones (1995), except for the effect of latent heat release that was not considered. Specifically, a dipole of θ-anomalies appears in the vicinity of the incipient tilted WWB-vortex, with cold (warm) anomalies on the down- (up-) tilt side. A similar dipole of θ-anomalies also appears in the DRY run (not shown). Of interest are the phase lags between the thermal anomaly, upward motion, and precipitation, along any cyclonic streamline within the vortex. That is, the low-level incoming moist easterly flow begins to slowly ascend isentropically on the northern side of the vortex, triggering latent heat release and precipitation with increased upward motion after passing the warm anomaly. The cyclonic-downstream advection of cloud/precipitation particles results in the development of higher radar reflectivity on the downtilt-right side. Evaporative cooling, inducing concentrated moist downdrafts, occurs prior to reaching the cold anomaly core on the downtilt-left side. The downtilt-left semicircle remains unfavorable for convective development due to the presence of mesoscale isentropic descent.

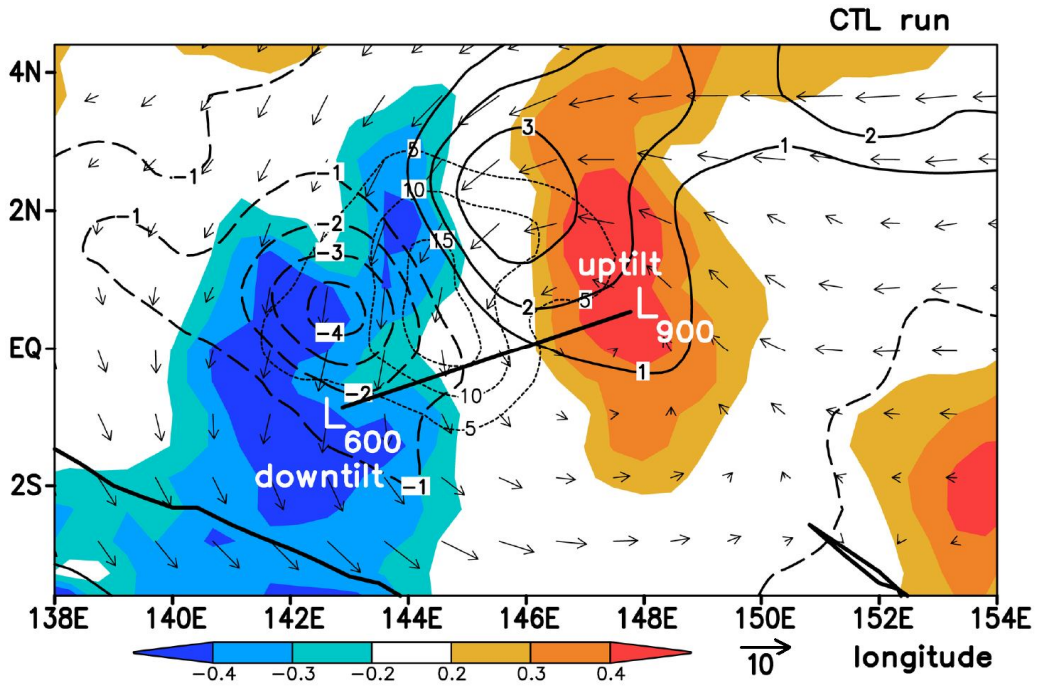

Figure 2.11. Horizontal distribution of 700-hPa simulated potential temperature (θ) anomalies (K, shaded), radar reflectivity (light dotted contours at intervals of 5 dBZ), and vertical motion anomalies (heavy contours at intervals of 1 cm s^{-1}) at 0600 UTC 30 April (12-h time mean). Horizontal wind vectors (900 – 500 hPa layer-mean) and the vortex tilt (heavy solid line) between 600 hPa (L_{600}) and 900 hPa (L_{900}) are shown.

Because of the convective development on the downtilt-right side, lower surface pressures tend to be generated to the north as a result of the associated compensating subsidence, thus forcing the low-level vortex center to move northward toward the area of intense latent heating (Wang and Holland 1996). Meanwhile, convectively generated upright vortices, to be examined in Chapter 3 of this dissertation, increase the midlevel cyclonic vorticity to the north, and tend to "absorb" the background vorticity associated with the WWB-vortex through horizontal convergence, thereby leading to an increasingly vertically erect vortex that could commence intensification as an upright, barotropic TC. In their study of westward-tilting equatorial waves during the MJO, Dickinson and Molinari (2002) found that precipitation occurred to the north of the waves, causing their "transition" into TD-type disturbances, but no

mechanism for the "transition" was discussed. Thus, the above result suggests that the westward-tilted WWB-vortex provides a favorable environment for the organization of deep convection on the downtilt-right side, and it is deep convection that plays an important role in vertically aligning the cyclonic circulations, causing the genesis of Chanchu.

2.5.3. The aborted genesis

Although it is not possible to validate the aborted genesis, it is of interest to examine why TCG could temporarily occur near the equator and why it is later aborted. Prior to the aborted genesis at 1/15-111, the tilted vortex is characterized by an elongated area of precipitation in its northern semicircle (Fig. 2.12e). Thus, the genesis scenarios similar to those discussed in the preceding subsection appear during the 1/15-111 – 2/18-138 period, including the increased midlevel cyclonic vorticity by deep convection north of the surface low, and the absorption of the WWB-vortex related vorticity. As a result, the vortex becomes nearly upright by 1/15-111, in association with an inner-core convective band that develops in a convergence zone about 30 km to the north of the vortex center (see Fig. 2.12f). Because the latent heating occurs in the inner-core region, it is much more effective in spinning up the vortex than that in the outer region (Hack and Schubert 1986). It is important to note that even though the midlevel circulation center becomes nearly upright with its low-level counterpart in the vicinity of the convective band, the outer regions of the vortex continue to exhibit vertical tilt, as indicated by the highly asymmetric circulation at 600 hPa. Thus, the tilted WWB-vortex continues to support precipitation generation

on the downtilt-right during the aborted genesis period (Fig. 2.12). Almost no precipitation occurs to the south of the vortex, i.e., downtilt-left.

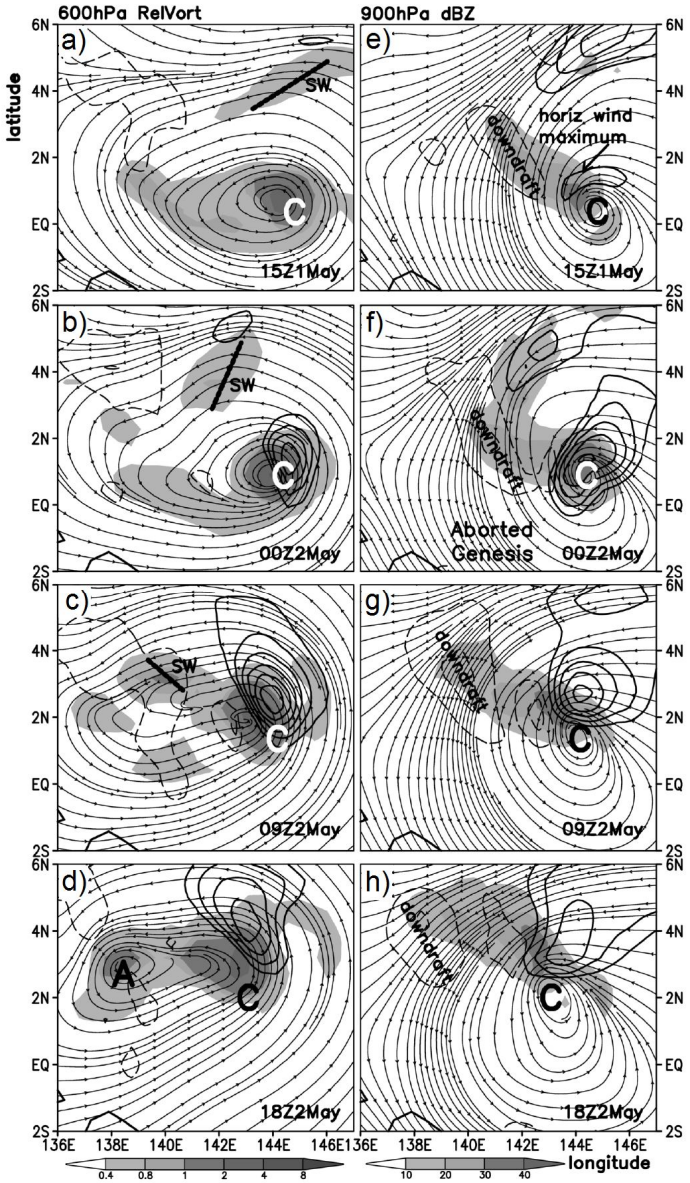

Figure 2.12. Horizontal distribution of (a) – (d) 600-hPa relative vorticity (shaded, x 10^{-5} s^{-1}) and (e) – (h) 900-hPa radar reflectivity (shaded, dBZ) at 9 h intervals, from 1/15-111 (top) – 2/18-138 (bottom) and superimposed with streamlines during the aborted genesis. Horizontal wind magnitude (thick solid contours at 14, 15, 16, 17, and 18 m s^{-1}), and descending moiton (light dashed contours at 1, 5, 10, 20, 40 cm s^{-1}) are shown. Symbol, "C" denotes the center of the 900-hPa closed circulation, and the heavy solid line in (a) – (c) denotes the location of a SW, which develops into 600-hPa closed circulation "A". Fields are averaged within a ±3-h period and a ±50-hPa layer.

As convection intensifies in the inner-core region, the maximum tangential winds increase rapidly (about 30 - 40%) in a deep layer between 1/15-111 and 2/00-120 (Fig. 2.12e,f), while P_{min} falls from 1005 hPa to nearly 1000 hPa (Fig. 2.8). With the nearly upright vortex structure and organized deep convective bands in the inner-core regions, one may expect the beginning of TCG at 2/00-120 (Fig. 2.12b,f). However, the convective band weakens shortly after 2/00-120 due likely to the spread of cold downdraft air into the core region. That is, the intrusion of dry northwesterly flow causes evaporation of hydrometeors, which in turn induces mesoscale downdrafts in the trailing regions of the convective band (Figs. 2.12e-g), thereby aiding in the suffocation of deep convection in the inner-core region. Although the magnitude of moist downdrafts at 900 hPa in the trailing stratiform region is generally less than 10 cm s^{-1} during the aborted genesis (Fig. 2.12f), they cover a large area of the western half of the vortex. Of course, TCG is not generally favored at such low latitudes (~1ºN).

Once the inner-core deep convection weakens (Fig. 2.12g), convectively generated cyclonic vorticity tends to be advected within the larger-sized tilted pre-Chanchu vortex, especially at the mid- and upper-levels (Figs. 2.12c,d), and thus an increased vertical tilt appears again. Meanwhile, outside of the core region, another shortwave becomes trapped within the midlevel circulation during the aborted genesis, assisting in the formation of a new closed vortex circulation "A" at 2/18-138 within the pre-Chanchu vortex (Fig. 2.12d). As a result, a broad west-east oriented elliptically-shaped midlevel vortex is situated northwest of the low-level circulation center (Figs. 2.12d and 2.12h).

2.5.4. Relationship between vertical tilt and TCG

Fig. 2.13 shows the subsequent evolution of the pre-Chanchu disturbance after the aborted genesis, ultimately leading to sustained genesis. At 2/21-141, i.e., 21 h after the aborted genesis, (cf. Figs. 2.12b,f and 2.13a), the vortex still exhibits a significant westward vertical tilt, with a distance of about 500 km between the 900- and 600-hPa circulation centers (Fig. 2.13a). Of importance is that deep convection is still confined to the downtilt-right half of the vortex, as dictated by the tilted vortex dynamics (see Fig. 2.11), despite the enhanced vertical tilt of the pre-Chanchu vortex following the aborted genesis. However, the major rainband, to be detailed in Chapter 3, is shifted far away from the 900-hPa circulation center (Fig. 2.12h) and not as intense as that occurring during the aborted genesis. In the upper troposphere, easterly and southeasterly flows are diffluent (Fig. 2.13e) and generally favorable for system intensification when combined with the vertical shear of below 10 m s^{-1} (Fig. 2.8). A large area of stratiform precipitation occurs to the northwest of the peak radar reflectivity (Fig. 2.13a) due to the presence of ascending southeasterly flow associated with the tilted rotational flows.

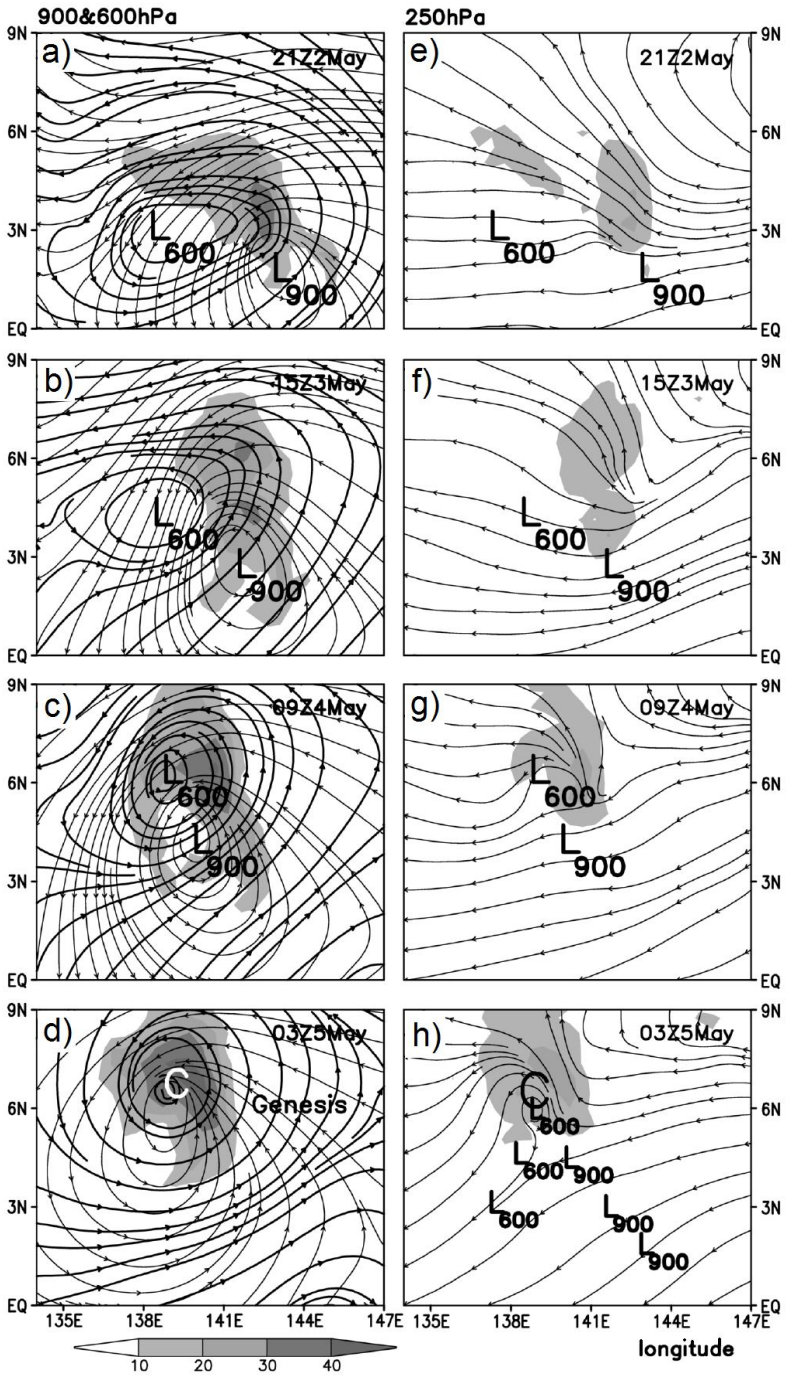

Figure 2.13. Horizontal distribution of the radar reflectivity (shading, dBZ) and streamlines at (a) – (d) 900 hPa and (e) – (h) 250 hPa from 2/21-141 (top) – 5/03-195 (bottom) at 18 h intervals. In (a) – (d) 600-hPa streamlines are superposed to show the diminishing vertical tilt of the pre-Chanchu vortex. The 600- and 900-hPa circulation centers are denoted by "L_{600}" and "L_{900}," respectively, until the genesis of Chanchu ("C") has commenced.

By 3/15-159 (Fig. 2.13b), the orientation of the vortex tilt becomes more northwest-southeast (cf. Figs. 2.13a,b or 2.13h) as a result of differing movements between the low and midlevel circulations. That is, as discussed for the aborted genesis, the convectively generated vortices (or lower pressures) steer the surface low northwestward, while the convectively generated midlevel vortices, or MCVs to be discussed in Chapter 3 of this dissertation, tend to force the midlevel circulations to move northeastward. Thus, the distance between the lower and midlevel circulation centers, i.e., the vertical vortex tilt, decreases with time as long as the convective bands and associated stratiform regions can be maintained on the downtilt-right side. At 250 hPa, convective blocking leads to the northward deflection of the incoming easterly flow and pronounced diffluence behind the convective bands (Fig. 2.14f).

Subsequently, as the vertical tilt diminishes at 4/09-177, precipitation begins to wrap into the midlevel vortex (Fig. 2.13c), accelerating its spinup. By 5/03-195, the pre-Chanchu vortex becomes vertically coherent (Fig. 2.13d), nearly at the same time when the steady decrease in P_{min} commences (Fig. 2.8), signifying the beginning of TCG. A closed vortex circulation even could be seen at 250 hPa at this time (Fig. 2.13h). Note that even though the circulation *centers* are vertically coherent from 900 to 250 hPa, significant 900 – 600-hPa vertical shear (Fig. 2.13d) still exists in the far-field flow. This highlights further the result of Jones (2004), who found that even though the vortex centers exhibit little vertical tilt, the far field flow may still exhibit tilt. In fact, this is the case at TCG herein, when the northwest-southeast tilt still exists outside of the inner core (Fig. 2.13d). The resulting downtilt-right convection appears now as a spiral band, and the downtilt-left environment remains nearly

precipitation-free. To summarize, the final two days of pre-genesis can be characterized by an increasingly vertically upright, northward moving vortex (i.e., from 900 to 250 hPa) as determined by the development of deep convection on the downtilt-right portion of the pre-Chanchu disturbance, leading to the surface cyclogenesis by 5/00-192 (Fig. 2.13h).

2.6. Summary and conclusions

In this chapter, the larger-scale structures and evolution prior to and during the genesis of Typhoon Chanchu are analyzed in the context of the early 2006 tropical season using NCEP's FNL, satellite observations, and 11-day numerical simulations with the WRF-ARW model. It is found that the active phase of the MJO provided the necessary low-level convergence and rotation for the development of a precursor disturbance, particularly through a WWB that propagated near the equator from the Indian Ocean into the Pacific Ocean during late April 2006. It is shown that the 11-day simulation captures well many larger-scale aspects for the formation of Chanchu, including the propagation and structure of the WWB, the initial spinup of the pre-Chanchu disturbance at the eastern periphery of the WWB, and the general track and intensification of Chanchu. Although the simulated intensification begins two days prior to that observed, genesis occurs at nearly the same location along the track.

Fig. 2.14 shows a conceptual model of several larger-scale processes leading to the genesis of Chanchu (2006), based on both the observations and model simulation. First, an eastward-moving WWB facilitates the development of a westward tilted cyclonic disturbance where the WWB interfaces with the easterly trades (Fig. 2.14a). Wave accumulation plays an important role in the formation of

the closed circulation associated with the vertically tilted pre-Chanchu disturbance. Second, the tilted WWB-vortex induces mesoscale isentropic ascent to its north (i.e. downtilt-right), which is consistent with the conceptual model of Jones (1995) for a tilted vortex (Fig. 2.14b). During this phase, deep convection is triggered on the downtilt-right side of the vortex as a result of the mesoscale lifting of the tropical maritime moist air in the lower troposphere. Moreover, the vortex circulations at individual levels deviate northward toward the area of ongoing deep convection and associated enhanced vorticity, causing a decrease in the vertical tilt with time. Third, sustained surface cyclogenesis commences as the vortex becomes more upright in the vertical (Fig. 2.14c), despite the fact that the periphery still remains tilted and downtilt-right convection continues as a spiral rainband.

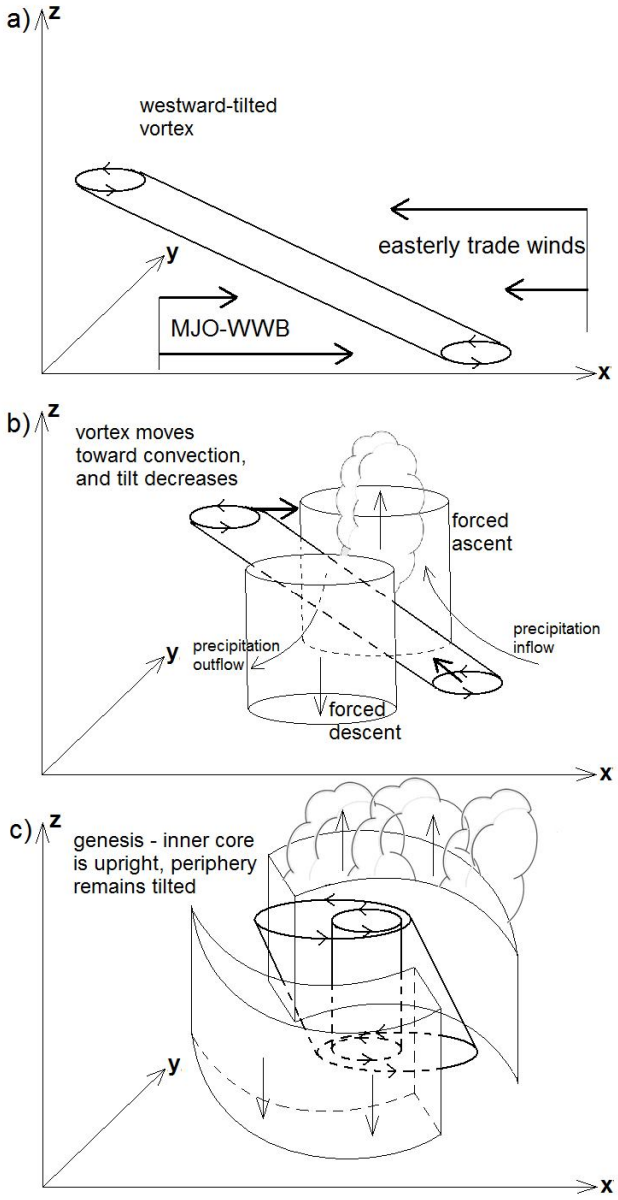

Figure 2.14. Conceptual model for (a) the development of a westward-tilted vortex at the interface of the WWB and easterly trades, (b) its associated ascent (descent) on the downtilt-right (downtilt-left) side and the distribution of deep convection on the downtilt-right of the vortex, and (c) the final vertical alignment of the vortex centers leading to the self-sustained genesis.

Although previous studies have shown the westward-tilting structure of the WWB in the West Pacific (e.g., Sperber 2003), none have discussed the implications of the tilt on TCG. Of particular importance are the processes, associated with the

diabatic heating on the downtilt-right side that precede the transition of the precursor tilted vortex into a vertically coherent tropical cyclone. A comparison with a dry sensitivity simulation suggests that the diabatic heating indeed plays an important role in determining the northward deviation. Note that this chapter serves to establish a baseline for the genesis of Chanchu using only the coarse mesh of the quadruply-nested simulation. In Chapter 3, we will conduct analyses of mesoscale processes ongoing during the final two days of pre-genesis using the finer nested simulation dataset, with the goal of clarifying the evolution of the downtilt-right convective processes and their impact on impending TCG.

Chapter 3: Mesoscale evolution of precipitation and tropical transition of the baroclinic vortex

3.1. Introduction

Tropical cyclogenesis (TCG) remains an enigmatic phenomenon because many of the processes that precede genesis are not well observed at the mesoscale. While the pre-conditions for TCG are well established (e.g., Gray 1998) and persist year round in the Western North Pacific (WNP), the organization of deep convection that precedes and causes TCG is not yet well understood. However, as our ability to observe the tropical atmosphere has improved over the years, much progress has come toward the understanding of TCG at smaller scales.

Recent observational and modeling studies view TCG as a stochastic phenomenon (Simpson et al. 1997) involving various mesoscale interactions that lead to the upscale growth of cyclonic vorticity and eventually result in a self-sustaining surface cyclonic circulation. Ritchie and Holland (1999) found that almost all TCG cases in the West Pacific develop in association with at least one mesoscale convective system (MCS), which can often spawn mesoscale convective vortices (MCVs) (Zhang and Fritsch 1987; Bartels and Maddox 1991; Fritsch et al. 1994; Harr and Elsberry 1996). MCVs often persist in the lower to mid-troposphere after MCSs decays, and several studies have identified MCVs (Harr et al. 1996; Zhang and Bao 1996) and vortex mergers (Simpson et al. 1997; Ritchie and Holland 1997; Kieu and Zhang 2008) as precursors to TCG. As individual MCVs develop within close proximity, they may interact and merge into a larger and stronger MCV, particularly if several small MCVs exist within a larger cyclonic circulation, such as the West

Pacific monsoon trough (Simpson et al. 1997). The phenomenon of vortex mergers is widely believed to play a role in some TCG cases, and Houze (2004) suggested that MCVs are the building blocks of tropical cyclones (TCs). Recently, Kieu and Zhang (2008) found that the genesis of Tropical Storm Eugene (2005) resulted from the merging of two mesovortices, spawned from MCSs within the Intertropical Convergence Zone (ITCZ). Obviously, the result of merging vortices is the formation of a larger and stronger lower-tropospheric vortex. But for a sustained TCG process to take place, cyclonic circulation must increase near the surface.

Two pathways have been proposed to understand the development of near-surface vorticity, and they are often referred to as top-down and bottom-up, in reference to the vertical direction of vorticity growth. The top-down theory of Bister and Emanuel (1997) suggests that microphysical processes in the stratiform precipitation region aid in the downward advective transport of vorticity associated with an MCV. After the MCV reaches the surface, the equivalent potential temperature θ_e increases via surface fluxes, and downdraft-free convection erupts in the center of the surface circulation, leading to a self-sustaining TC via the so-called wind-induced surface heat exchange (WISHE, Emanuel 1987). Zhang and Bao (1996a,b) show that an MCV provides the necessary quasi-balanced forcing for the initiation and organization of deep convection, leading to the generation of cyclonic vorticity in the maritime boundary layer (MBL). The associated absolute angular momentum is then advected upward by convective updrafts to intensify the cyclonic flows above (see Zhang et al. 2001). This bottom-up mechanism was later advanced by Hendricks et al. (2004) and Montgomery et al. (2006) who showed that within the

broad envelope of an MCV, deep convective processes tilt ambient horizontal vorticity and stretch convectively generated vorticity to form vortical hot towers (VHTs). Subsequently the VHTs merge, leading to an increase of the system-scale cyclonic vorticity, and eventually the WISHE process is invoked.

Both the bottom-up and top-down hypotheses focus on the development of cyclonic vorticity from small to larger scales. In essence, the point of dissonance is the relative importance of convective versus stratiform precipitation, which unfortunately coexist in close proximity and thus present an observational challenge. Many recent studies support the bottom-up mechanism because of the ability of convective processes to rapidly generate large amounts of cyclonic vorticity in the MBL through vortex stretching. Nonetheless, the conundrum remains that while the upscale growth of cyclonic vorticity, e.g., via mergers, happens ubiquitously, TCG does not. Thus, more case studies are needed to understand different processes leading to TCG.

A better understanding of the organization of MCSs and the resulting cyclonic vorticity may shed light on the TCG processes. Zipser and Gautier (1978), hereafter ZG78, analyzed the largest MCS during the GARP Atlantic Tropical Experiment (GATE) that occurred within an intensifying tropical depression. ZG78 found that as the MCS' cloud shield evolved from circular in shape to more comma-shaped with time, the midlevel circulation center occurred westward of that at the low levels (see Figs. 6 and 7 therein). Despite the large sized MCS, ZG78 detected no low-θ_e downdrafts. In a recent study, Houze et al. (2009), hereafter H09, discussed a similar large MCS that occurred in the early stages of Hurricane Ophelia (2005) during the

Hurricane Rainband and Intensity Change Experiment (RAINEX). The giant MCS also exhibited little cold downdrafts and preceded TCG with a large comma cloud pattern (see Fig. 5e in H09). They concluded that the large convective production of cyclonic vorticity within the MCS supports the bottom-up TCG. Thus, the development of MCSs is increasingly recognized as critical to TCG, but their roles remain uncertain.

In Chapter 2 of this dissertation, we presented an 11-day (i.e., 0000 UTC 27 April – 0000 UTC 8 May) cloud-resolving simulation of the genesis of Typhoon Chanchu (2006) that occurred in the near-equatorial West Pacific during the active phase of the Madden-Julian oscillation (MJO) using the quadruply nested (54/18/6/2 km) version of the Weather Research and Forecast (WRF) model. Results show that a synoptic westerly wind burst (WWB) associated with the MJO accounts for the generation of a westward-tilted vortex with organized cyclonic rotation up to 400 hPa, hereafter the titled WWB-vortex, which gives rise to the development of deep convection at a preferred location (i.e., on the downtilt-right side). Genesis of Chanchu from the WWB-vortex, which develops near the equator early in the simulation, takes place near 192 h into the model integration, which is valid at 0000 UTC 5 May 2006 (hereafter 5/00-192), and after a long incubation period of the incipient tilted WWB-vortex. This incubation period is characterized by an increasingly upright vortex as a result of persistent convective overturning on the downtilt-right side of the vortex. Although the simulated genesis begins 2 days prior to that observed, it occurs at nearly the same location along the track.

The objectives of the present chapter are to (i) examine the three-dimensional (3D) structures and evolution of several MCSs and an MCV in relation to the tilted WWB-vortex during the pre-genesis stage; (ii) clarify the impact of convectively generated cyclonic vorticity and vortex mergers on the genesis of Chanchu; and (iii) gain insight into the trigger of TCG as the tilted WWB-vortex transitions to an upright vortex prior to TCG. They will be achieved using the 11-day cloud-resolving simulations of the case mostly from the 6-km resolution domain.

The next section summarizes the general distribution of precipitation with respect to the evolution of the vertically tilted WWB-vortex up to the genesis of Chanchu. Section 3.3 describes the 3D structures and evolution of four MCSs in relation to the tilted WWB-vortex as well as their contributions to the system-scale rotation during a two-day period prior to TCG. Section 3.4 presents the transition of the WWB-vortex from a weak barolinic system to a warm-cored TC and discusses the trigger of TCG. A summary and concluding remarks are given in the final section.

3.2. Overview of pre-genesis

Fig. 3.1 provides an overview of the low- and midlevel evolution of the horizontal flows and relative vorticity as well as the simulated radar reflectivity prior to and at the early stage of the genesis of Chanchu. At 3/00-144 (i.e., 48 h prior to genesis; see Figs. 3.1a,e), the vertically tilted WWB-vortex circulations occur at horizontal scales of more than 1000 km, with the 600-hPa center (denoted as "A" in Fig. 3.1a) located about 400 km to the west-northwest of the 900-hPa center (denoted as "C" in Fig. 3.1e); the horizontal distance between A and C represents the vertical tilt of the WWB-vortex between 600 and 900 hPa. A south-north-oriented convective

rainband, as defined by a large gradient of radar reflectivity, develops to the north of C on the downtilt-right side of the tilted WWB-vortex. The downtilt-right is a favorable location for isentropic lifting of the moist MBL air (Jones 1995), as discussed in detail in Chapter 2. The mid- and upper-level cyclonic flows account for the generation of extensive trailing stratiform clouds to the north (Fig. 3.1e). A convectively generated cyclonic vorticity (ζ^+) band, denoted by "V," will be shown in section 3.3 as an MCV corresponding to the leading rainband. The MCV depresses the local flow fields into a deep midlevel trough, with another relatively weaker vorticity center situated in the trailing stratiform region (Fig. 3.1a).

Of importance is that A and V are located within a midlevel large cyclonic envelope modulated by the WWB, which is a favorable scenario for merger (Simpson et al. 1997). Indeed, A and V begin to merge by 4/00-168 (Fig. 3.1b). The resulting vortex AV contracts and exhibits a more circular shape with the peak ζ^+ of greater than 2 x 10^{-5} s^{-1} near the vortex center at 5/00-192 (Fig. 3.1c). Meanwhile, the centers of AV and C become nearly collocated, signifying the genesis of Chanchu with a comma-shaped cloud band in its inner-core region.

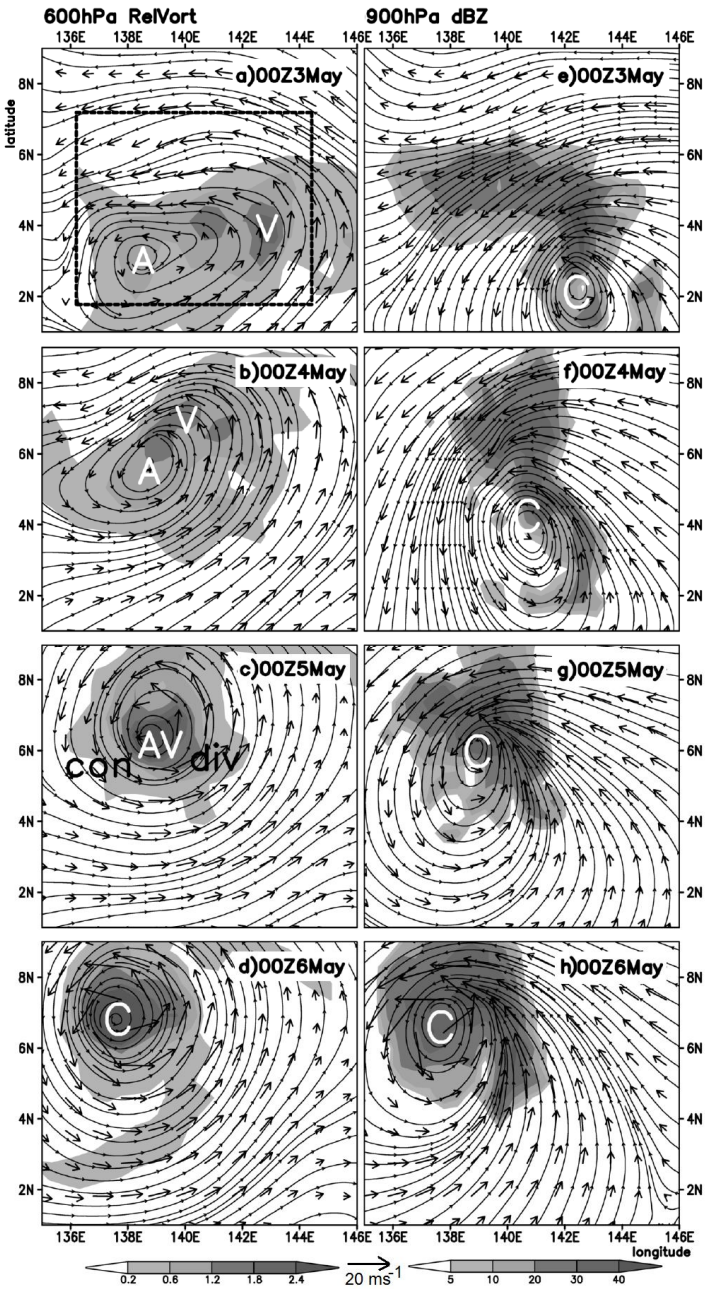

Figure 3.1. Horizontal distribution of the (a) – (d) 600-hPa flow vectors, streamlines, and the (500-700 hPa) layer-averaged relative vorticity (shaded, 10^{-5} s^{-1}); and the (e) – (h) 900-hPa flow vectors, streamlines, and radar reflectivity (shaded, dBZ), given at 24-h intervals from the 7 – 10 day simulation, valid between 0000 UTC 3 – 0000 UTC 6 May 2006, over the 54-km resolution domain. Letters, "A", "C", and "V", denote the location of the peak relative vorticity associated with the Pre-Chanchu vortex at 600-hPa and 900-hPa, and an MCV, respectively. "AV" represents the merging of A and V (prior to 5 May), and the heavy box in (a) denotes the area of focus for Fig. 3.3.

The time series of the minimum sea-level central pressure (P_{min}) at high temporal resolution, given in Fig. 3.2a, shows that the storm intensity fluctuates during pre-genesis, but it does not deepen continuously until 5/00-192. During the pre-genesis period, P_{min} remains above 1000 hPa, which is even higher than the value at the earlier stages, and the maximum surface wind (V_{max}) generally remains below 20 m s^{-1}. [Note that the magnitudes of P_{min} and V_{max} shown herein are greater than those shown in Chapter 2 due to the use of different (6- vs. 18-km) resolution data.] While the magnitude of V_{max} exceeds the threshold for a tropical depression throughout pre-genesis, the location of V_{max} during 3 – 5 May appears to be closely associated with the distribution of *four distinct MCSs*, referred to as MCS1-4 (their durations are marked in Fig. 3.2a), that develop to the north of the low-level circulation center C. Of interest is that the life cycles of the four MCSs coincide well with the fluctuation of P_{min}, but have little long-lasting impact on the storm intensity, as TCG does not occur until near the end of the final MCS. The area-averaged surface wind speed (V_{mean}) also shows little increases during the pre-genesis stages in spite of continued MCS development (Fig. 3.2a). Furthermore, Fig. 3.2b shows that little changes occur in the low-level relative vorticity, despite the existence of a closed circulation throughout the period of interest. On the other hand, the midlevel cyclonic vorticity begins to rapidly increase at 4/00-168, i.e., 24 h prior to genesis, due to the merging of convectively generated vortices (see Chapter 2). As will be shown in the next section, the four MCSs contribute in different ways to the genesis of Chanchu through the enhancement of midlevel cyclonic vorticity.

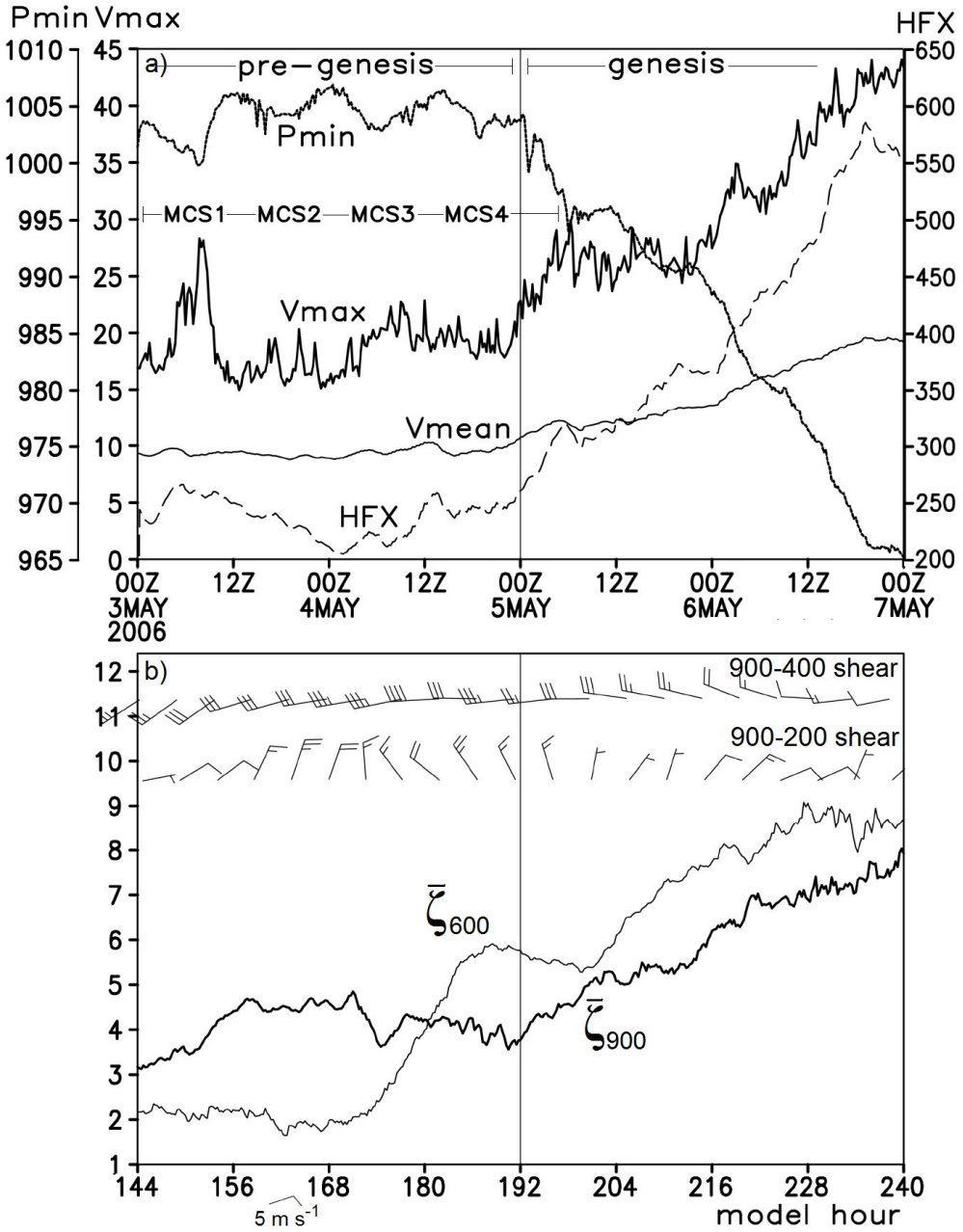

Figure 3.2. (a) Time series (at 15-min intervals) of the minimum central pressure (P_{min}, hPa), the maximum surface winds (V_{max}, m s^{-1}), and the area-averaged (500 km × 500 km, centered at the low-level circulation center) surface latent and sensible heat fluxes (HFX, W m^{-2}, dashed) and surface wind (V_{mean}, m s^{-1}) during the 4-day period of the finest nested (Δx = 2 km) simulation (i.e., 3/00-144 – 7/00-240; (b) as in (a), but for the area-averaged relative vorticity (10^{-5} s^{-1}) at 600 hPa (ζ_{600}) and 900 hPa (ζ_{900}), and the area-averaged vertical shear (m s^{-1}, barbs) between 400 and 900 hPa-centered at C??. The thin vertical line at 0000 UTC 5 May demarcates the pre-genesis and genesis periods.

The simulated Chanchu begins to intensify by 5/00-192, after the midlevel vortex AV aligns vertically with the low-level vortex (Figs. 3.1c,g). Note that TCG in the present case occurs after more than 5 days of pre-genesis, during which time the near-surface circulation with $V_{max} > 15$ m s^{-1} is a persistent feature. Apparently, such a long time scale for the onset of TCG is attributable to the vertical tilt of the WWB-vortex, despite the development of organized deep convection and an increase in the midlevel rotation through the convective enhancement and vortex-merging processes (Figs. 3.1a and 3.2b). *TCG does not occur until the 600-hPa and 900-hPa circulation centers become vertically coherent* at 5/00-192. Nevertheless, even though the circulation centers become coherent in the vertical at the onset of TCG, the vertical wind shear (VWS) between 900 and 400 hPa in the near-storm environment remains significant (i.e., > 15 m s^{-1}, Fig. 3.2b).

In summary, while the MJO accounts for the formation of the tilted WWB-vortex, as detailed in Chapter 2, it is the convectively generated vortices and the subsequent merging into the WWB-vortex (e.g., A-V merger) that play some roles in the intensification of the midlevel vortex. When the vortex becomes upright, TCG commences and continues as long as deep convection could persist in the inner-core regions. In Chapter 2, we have shown an example of aborted genesis with V_{max} reaching 18 m s^{-1} near 2/00-120, at which time an upright vortex forms as a result of the interaction between convectively generated vortices and the WWB-vortex. However, TCG is aborted shortly after deep convection weakens, and subsequently the WWB-vortex tilts westward again. Thus, our discussion of pre-genesis that

follows will involve mesoscale events after the aborted genesis, i.e., beginning from 3/00-144.

3.3. Mesoscale evolution during pre-genesis: Four MCSs

In this section, we focus on the important roles of four MCSs in achieving the transition from a tilted to an upright vortex leading to TCG. Their general precipitation structures and their role in the formation of the above-mentioned MCV will be examined.

3.3.1. Mesoscale structures at an early pre-genesis stage

At 3/00-144, the near-surface disturbance exhibits a closed circulation with P_{min} ~ 1004 hPa near 3ºN (Fig. 3.3d). An elongated, north-south-oriented flow (and moisture) convergence line, as indicated by intersecting streamlines, appears in the MBL to the north of C (i.e., on the downtilt right side). Convergence is associated with a tropical squall line, or MCS1, which corresponds to the above-mentioned leading rainband, with strong radar reflectivity (cf. Figs. 3.3c and 3.1e). This MCS is still at its early development stage at this time. To the northwest of the leading convective line is an extensive area of trailing stratiform precipitation due to the presence of the pronounced easterly flows in the mid- to upper- levels (Figs. 3.3a-c).

A west-east vertical cross section, taken through MCS1 (Fig. 3.4a), shows a vertical mesoscale flow pattern that is similar to that shown by Gamache and Houze (1982) for a typical tropical squall line, including the lifting of high-θ_e air in the MBL easterly flow, strong ascent in the leading convective line, weak ascent (descent) above (below) the melting level in the trailing stratiform region, and a deep layer of front-to-rear (FTR) moist inflows. This flow pattern acts to continually generate

precipitation particles to maintain the large stratiform region, covering an area of nearly 80000 km^2 (Fig. 3.3c), which is about twice of the maximum size documented by Yuter and Houze (1998) in a study of WNP MCSs.

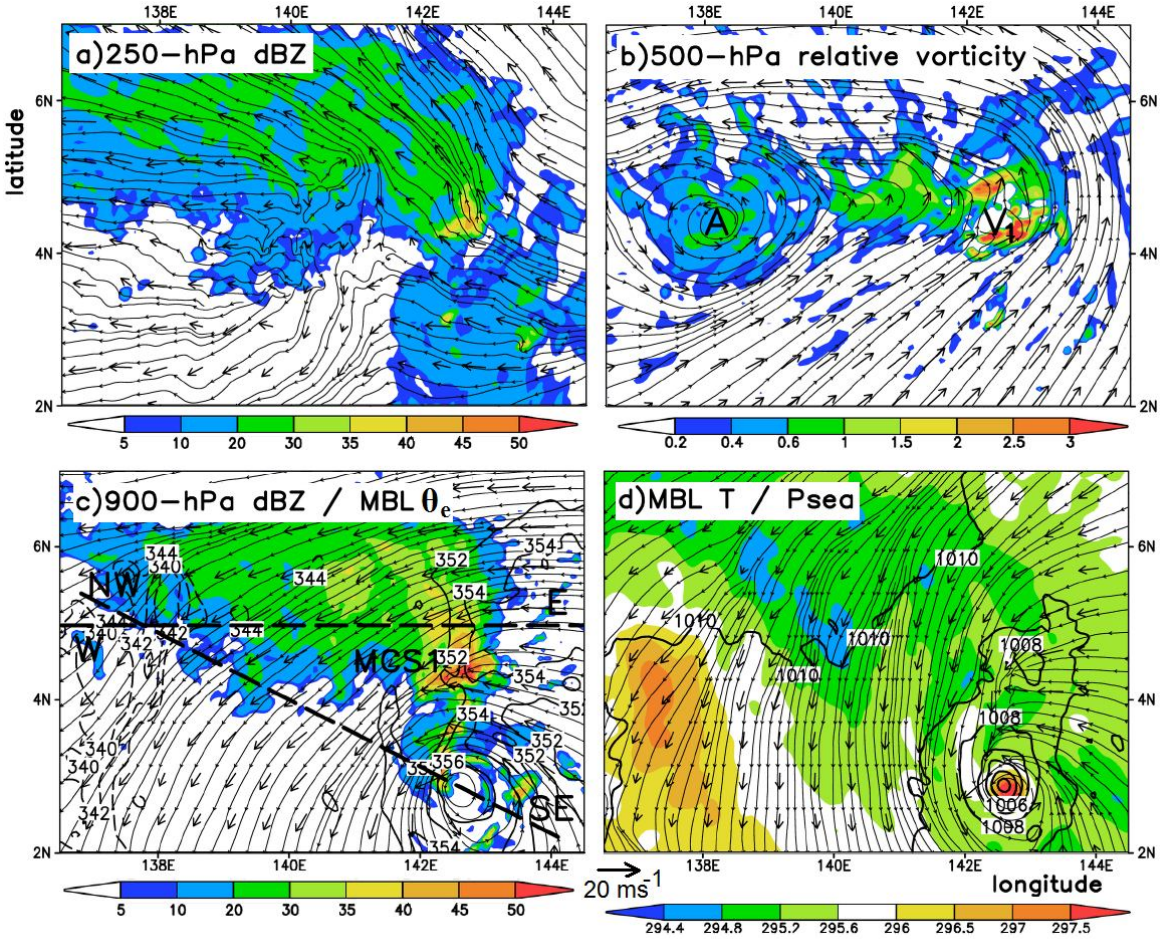

Figure 3.3. Horizontal distribution of (a) the 250-hPa radar reflectivity (shaded, dBZ); (b) the 500-hPa relative vorticity (shaded, 10^{-5} s^{-1}); (c) the 900-hPa radar reflectivity (shaded, dBZ) and the near-surface layer-averaged (i.e., between the surface and 900 hPa) equivalent potential temperature (contoured at 340, 342, 344, 352, 354, and 356 K); and (d) the near-surface layer-averaged temperature (shaded, °C) and the sea-level pressure (contoured at 1-hPa intervals), superposed with the horizontal flow vectors and streamlines at the individual levels, that are taken at 3/00-144 from the 6-km resolution domain. Symbols, "A" and "V_1" in (b), denote the WWB-related vortex and convectively vorticity centers, respectively (see text). The heavy dashed lines W – E and NW – SE in (c) denote the location of the vertical cross sections used in Fig. 3.4.

It is evident from Fig. 3.3b that MCS1 produces an upright column of significant cyclonic vorticity ($\zeta^+ \sim 3 \times 10^{-5}$ s^{-1} at 500 hPa) along the leading line and

weaker vorticity ($\zeta^+ \sim 1\times10^{-5}$ s^{-1}) in the stratiform region, which are superimposed with a *broad but shallow* cyclonic circulation ($\zeta^+ \sim 0.5 \times 10^{-5}$ s^{-1}) associated with the WWB-vortex (Fig. 3.4b) that tilts northwestward from its surface location C to the back edge of the stratiform region at 500 hPa (Figs. 3.3b-d, and 3.4b). The deep tilted vortex has a shallow layer of roughly 100 hPa, as defined by $\zeta^+ \sim 0.5 \times 10^{-5}$ s^{-1} (Fig. 3.4b), with little cyclonic vorticity above or below the layer, e.g., below (Fig. 3.3c) or above (Fig. 3.3a) the 500 hPa level. In short, the northwest-southeast tilted vortex is that which developed several days prior, while the midlevel vorticity to the east of A (Fig. 3.3b) is generated by convective processes.

Of importance is that the tilted WWB-vortex has a cold-cored baroclinic structure with large VWS and a weak warm layer above A, as compared to the warm-cored low-level circulation C with little VWS below 700 hPa (Fig. 3.4b). Because of the tilted circulations, the meridional flow changes direction with height, with large VWS across the vortex layer. One may note that the vertical cross-plane flow structures, i.e., the near-northerly flow below and a near-southerly flow above the vortex layer, resemble those associated with a midlatitude cold front, with the vortex layer corresponding to the "frontal zone". A thermal gradient of 2.8°C $(300\ km)^{-1}$ between the cold and warm cores coincides qualitatively well with the large VWS in the vortex layer. This thermal gradient is weaker than that in cold-cored systems that have developed into TCs in higher latitudes (e.g., Bracken and Bosart 2000; Davis and Bosart 2003).

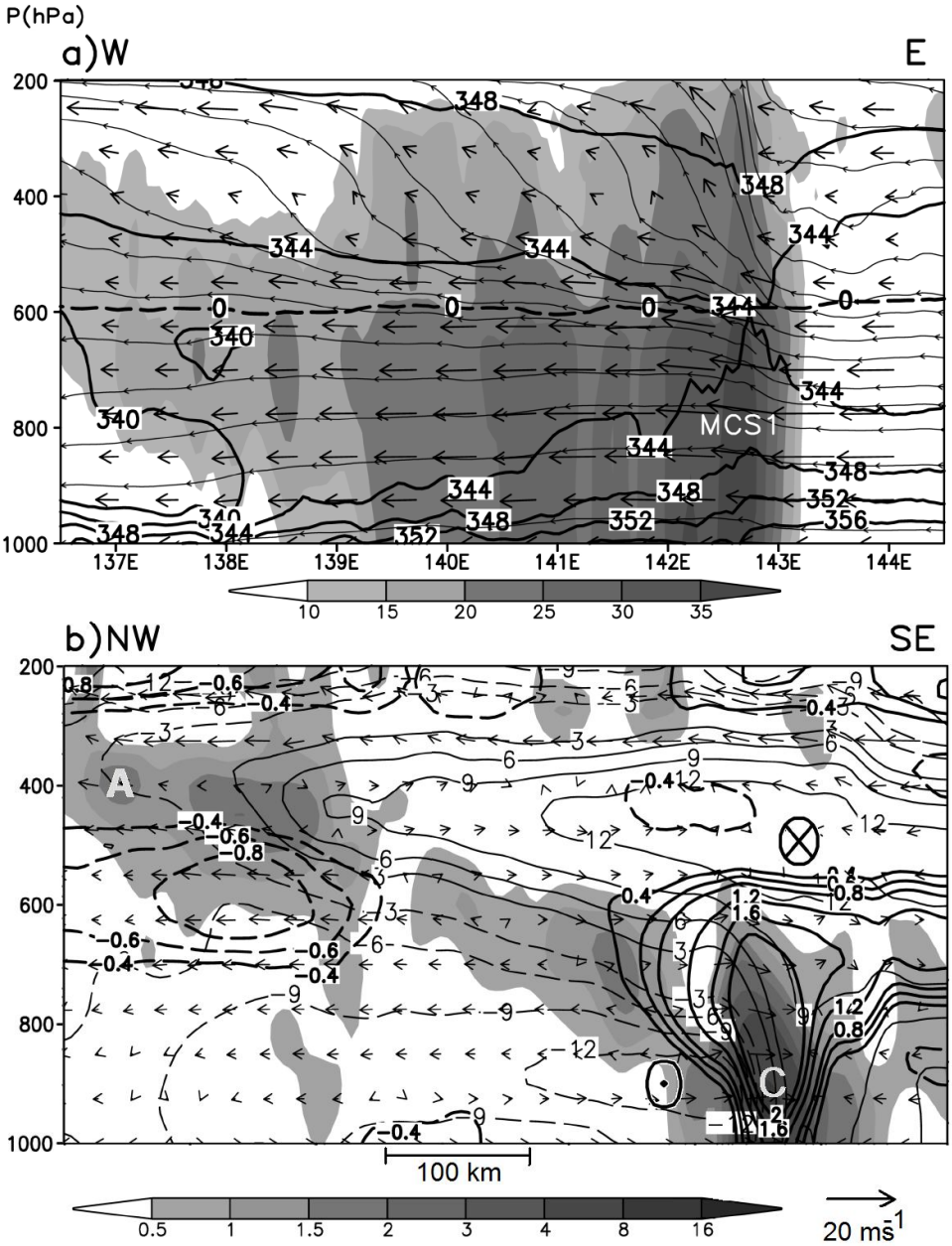

Figure 3.4. (a) West-east vertical cross section of in-plane flow vectors (vertical motion multiplied by a factor of 10) and streamlines, radar reflectivity (shaded, dBZ), equivalent potential temperature (at intervals of 4 K), superimposed with the melting level (heavy dashed line); and (b) Northwest-southeast vertical cross section of the relative vorticity (shaded, x 10^{-5} s^{-1}), the cross-plane wind speed (contoured, ± 3, 6, 9, 12, and 15 m s^{-1}) into (out of) the vertical plane with their maximum magnitude marked by a cross (dot) symbol, superimposed with deviation temperatures (heavy contours, ± 0.4, 0.6, 0.8, 1.2, 1.6 and 2.0 °C) and the location of the midlevel (low-level) vortex center A (C). They are taken at 3/00-144 from the 6-km resolution domain. Note that all the fields have been averaged within (a) 0.5° latitude and (b) a 3-h period to capture the basic structures of (a) MCS1 and (b) the northwestward tilt of the WWB-vortex. Deviation temperatures are obtained by subtracting the area-mean at individual levels in the cross section. See Fig. 3.3c for the locations of the cross sections.

As shown in Chapter 2, TCG occurs as this tilted vortex is transformed into an upright one. Davis and Bosart (2004) referred to the transformation of such a baroclinic disturbance to a warm-cored TC as tropical transition (TT), in contrast with extratropical transition (ET) from a TC to an extratropical disturbance. This transition has not been documented at such low latitudes and will be discussed explicitly in section 3.4. It should be noted that because of the shallowness, the closed cyclonic circulations associated with the tilted WWB-vortex at individual levels are not always aligned in one vertical cross section between the lower- and mid-level centers (i.e., A and C). The horizontal flow fields at different levels are used herein to help gain insight into the 3D structures and evolution of the pre-Chanchu disturbance.

Note that the tilted vortex core (or its peak cyclonic vorticity) at 3/00-144 is mostly distributed along the southern edge of the cloud/precipitation regions (Fig. 3.3c) at each level, confirming again the favorable location of the northern semicircle (i.e., downtilt-right) for convective development. In particular, the northern semicircle provides both a lifting mechanism (isentropic ascent) and the necessary background vorticity for vortex stretching near the equator. In fact, convectively generated cyclonic vorticity along the downtilt-right leading line is much stronger than that associated with the WWB-vortex, and it induces a deep trough that is superimposed with the broad closed circulation in the midtroposphere (Fig. 3.3b). Twenty hours later, this trough becomes a closed MCV at 600 hPa (see Figs. 3.5a-f). As will be seen in the next section, the midlevel vortex-vortex interaction (i.e., that between the WWB-vortex and the convectively-generated MCV) plays an important role in

aligning the WWB-vortex in the vertical because the circulation centers tend to approach regions of rapid vorticity production.

It should be mentioned that the horizontal flow structures shown in Fig. 3.3 appear similar to an intensifying tropical depression analyzed by ZG78 in which an MCS developed in the northern semicircle and the midlevel circulation is located westward of the low-level counterpart. Data limitations prevented ZG78 from ascertaining the complete 3D structures (i.e., any tilt that may have existed) of the developing depression. Our results show clearly how the tilted vortex and its associated vorticity are related from the surface to 400 hPa levels (cf. Figs. 3.3b,c and 4b), thus favoring northern semicircle precipitation generation. As shown in Chapter 2, the coherent vertical tilt can be clearly seen as early as April 30 when the closed circulations form.

While the WWB-vortex core remains mostly free of precipitation, its northwestern one-third portion is situated above the stratiform region, where some stratiform clouds/precipitation appear as a result of the advection by the northerly flow beneath the vortex layer (Fig. 3.4b). As precipitation falls through the low-θ_e layer below (Fig. 3.4a), evaporatively- and melting-driven moist downdrafts occur at the back edge of the trailing stratiform region (cf. Figs. 3.4a,b). This accounts for the generation of the lowest-θ_e air at 900 hPa, with a θ_e value (i.e., 340 K) similar to that in the 600-800 hPa layer, and a west-east θ_e gradient in the lower troposphere (Fig. 3.3c). Because the precipitation available for evaporation in the downdrafts diminishes below 800 hPa (Fig. 3.4a), the forced descent tends to occur dry adiabatically, leading to the local warming near the surface (Fig. 3.3d). As will be

seen later, the development of moist downdrafts helps to understand the life cycle of each MCS under study.

In the next subsections, we discuss the structure and evolution of MCS1 – MCS4 in turn as well as their implications to TCG. For this purpose, we have superimposed in Fig. 3.5 the simulated radar reflectivity with streamlines at 600 and 900 hPa at 4-h intervals in order to visualize the evolution of deep convection with respect to the tilted WWB-vortex and show what impact each MCS produces on the vortex. Fig. 3.5 shows that the transition between the four MCSs is essentially a continuous process, based on their precipitation structure. For discussion, however, we discretize them in accordance with the convective morphology.

3.3.2. Life cycle of MCS1: Squall line

It is evident from Figs. 3.5a-d that the typical tropical squall line structures associated with MCS1 change significantly during the period of 3/00-144 – 3/12-156. Specifically, the extraordinarily large stratiform region, shown in Fig. 3.3a, shrinks with time as the midlevel elliptical circulation shifts from a west-east to southwest-northeast orientation with a growing area of flows in opposite directions to those in the layers below. The stratiform precipitation almost dissipates by 3/12-156 when the 900- and 600-hPa flows behind the leading line become opposite in direction (Fig. 3.5d). Meanwhile, the northern portion of MCS1 evolves into a bow-shaped convective segment that is commonly observed in midlatitude squall lines in the presence of the rear-to-front (RTF) flows (e.g., Houze et al. 1989; Zhang et al. 1989), while the southern convective segment is displaced to the west semicircle of the low-

level circulation. As a result, the leading convective line changes its orientation from north-south to northeast-southwest (cf. Figs. 3.5a and 3.5d).

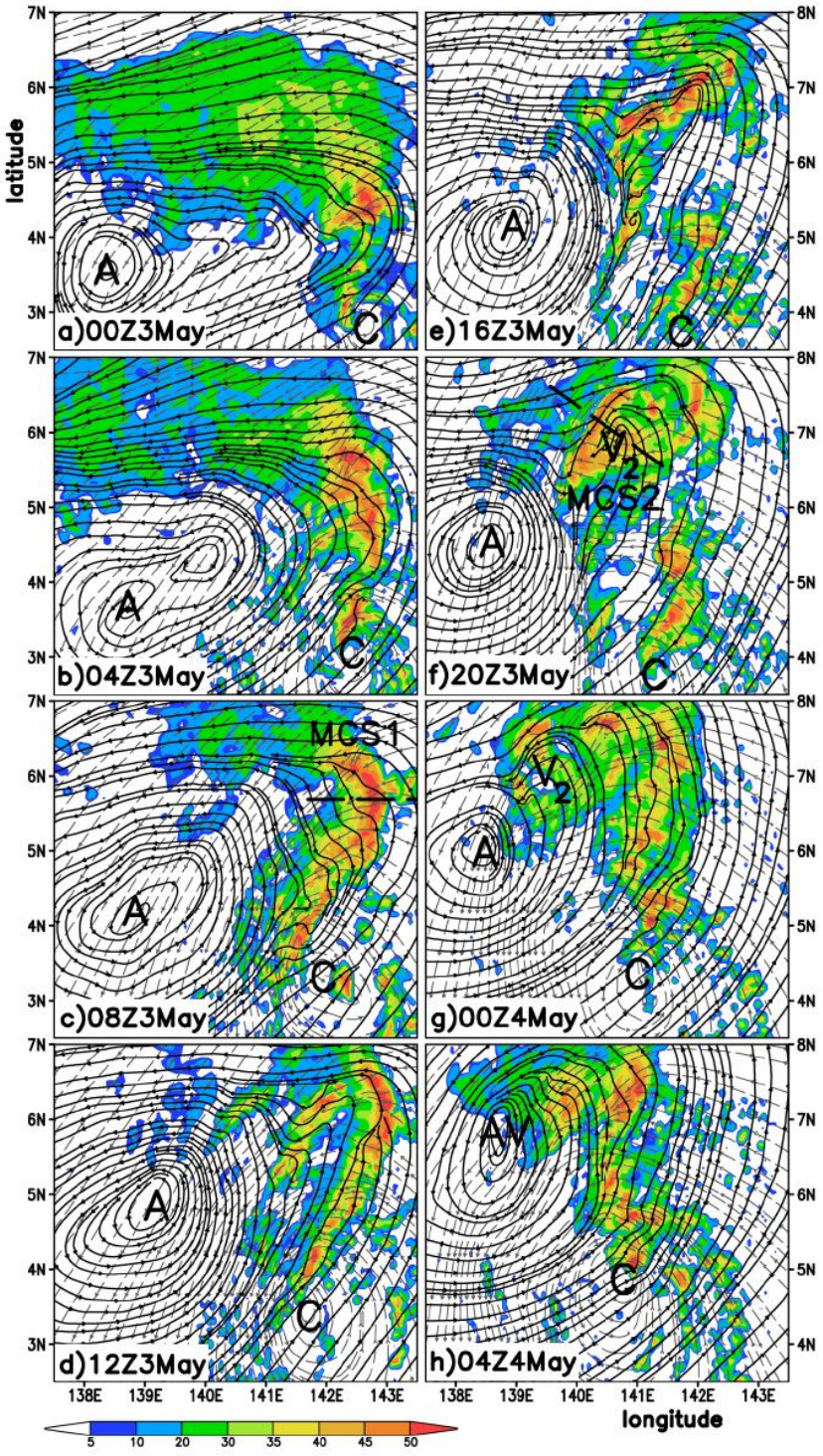

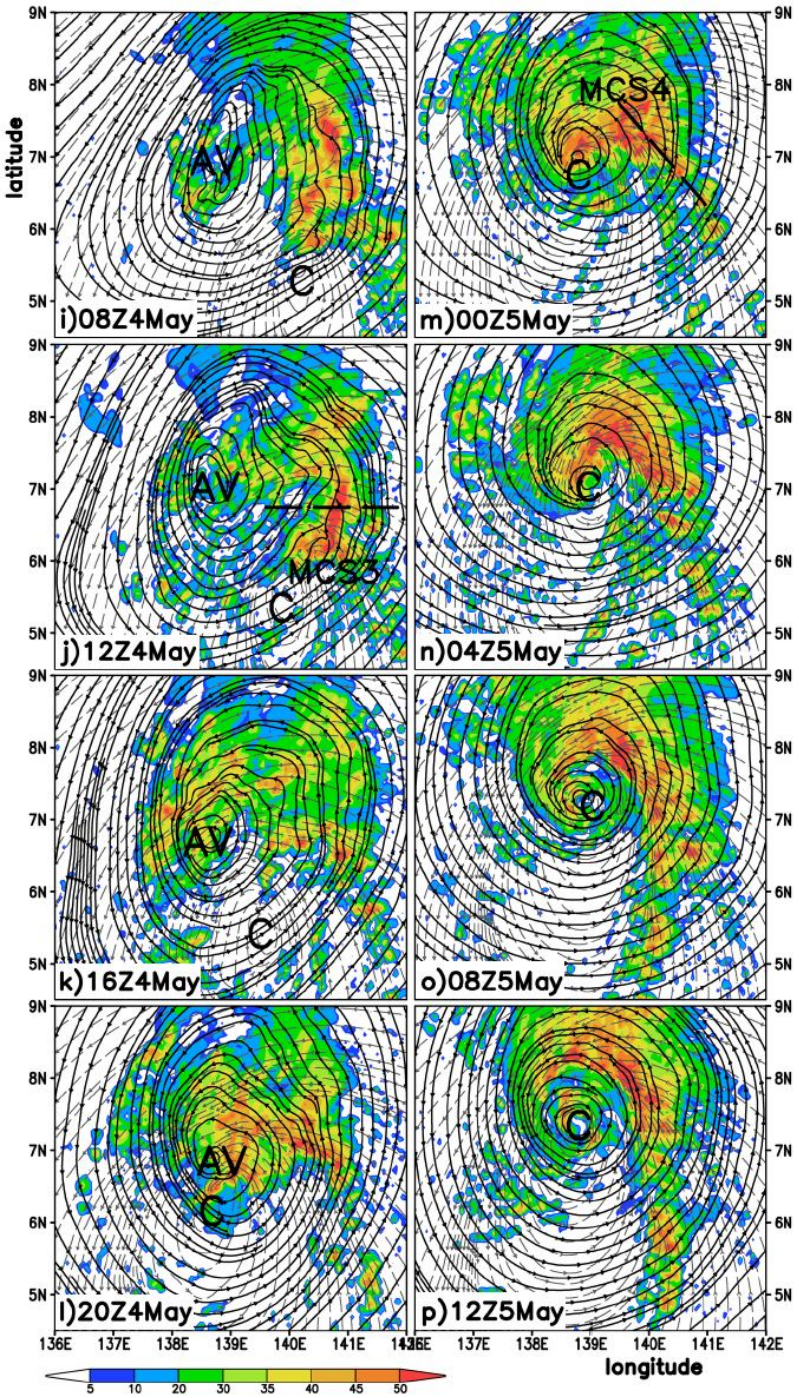

Figure 3.5. The evolution of the 900-hPa radar reflectivity (shaded, dBZ) at 4-h intervals between (a) 3/00-144 and (p) 5/12-204 from the 6-km resolution domain, superimposed with the 600-hPa (heavy solid) and 900-hPa (light dashed) streamlines. The path of vertical cross sections (heavy dashed) during the mature stage of (c) MCS1, (f) MCS2, (j) MCS3, and (m) MCS4 are denoted. Letter(s) "A", "AV", and "V_2" ("C") denote the center(s) of the 600-hPa (900-hPa) circulations, respectively.

Although no RTF flow is evident in the present case due to the presence of intense along-line and FTR flows, the increasing streamline curvature at the northern end of the squall line suggests a developing MCV in the midlevels. By 3/12-156 (Fig. 3.5d), a southwest-northeast oriented inverted trough develops behind the leading line and becomes almost a separate MCV entity at 3/20-164 (see V_2 in Fig. 3.5f). As shown in Zhang (1992), the northern segment of a squall line favors the generation of an MCV due to the tilting of horizontal vorticity associated with the local large VWS, the so-called bookend vortex (Weisman and Davis 1998). Convectively generated MCVs like V_2 are typical mesoscale phenomena that occur near the end of the life cycle of MCSs (Zhang and Fritch 1988; Menard and Fritsch 1989; Bartels and Maddox 1991). The increasing streamline curvature associated with V_2 effectively shrinks the stratiform region because the reduced FTR flows behind the leading convective line suppress the generation of hydrometeors.

A vertical (normal-line) cross section through the central portion of the bow-shaped convective line, given in Fig. 3.6a, shows a deep FTR inflow layer that decreases in magnitude up to 600 hPa, where the low-level easterly flows veer to the along-line direction with little normal-line flow above. Strong upward motion occurs in the leading line with intense cyclonic vorticity in the midlevel, which is consistent with the subsequent generation of an MCV (cf. Figs. 3.6a and 3.5a-f). Fig. 3.6a also shows that weak RTF flow does occur in the 600 – 400 hPa layer, but it does not penetrate to the leading line as that described in a typical squall system (Houze et al. 1989). This helps explain the very slow eastward movement of the leading line (Figs.

3.5a-d). The RTF flow becomes more pronounced as the MCV enters its mature stage (see Figs. 3.5f and 3.6b).

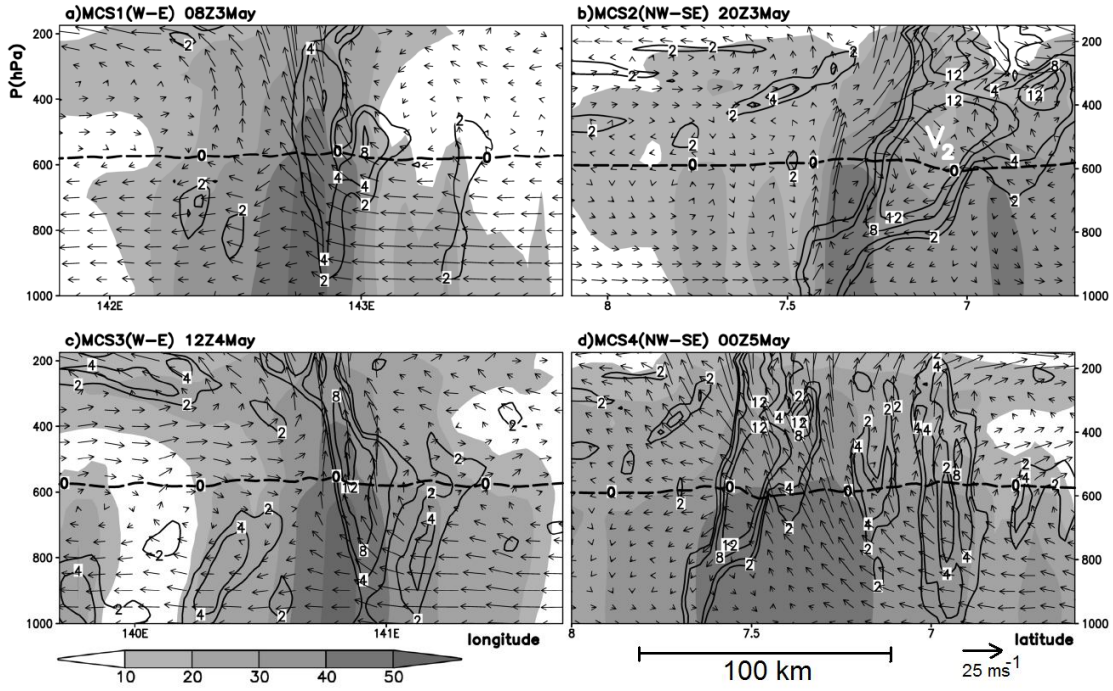

Figure 3.6. Vertical cross sections of the radar reflectivity (shaded, dBZ), and relative vorticity (contoured at 2, 4, 8, and 12 × 10^{-5} s^{-1}), superimposed with in-plane flow vectors, associated with (a) MCS1; (b) MCS2; (c) MCS3; and (d) MCS4, that are taken nearly along the low-level flows given in Figs. 3.5c, 3.5f, 3.5j, and 3.5m, respectively. Vertical motion for in-plane vectors has been enhanced by a factor of 10, and the heavy dashed lines denote the distribution of the melting level.

The MCV, together with the cyclonic vorticity along the leading line, represents the contribution of MCS1 to the *midlevel* storm-scale rotation. Because MCS1 becomes most intense more than 200 km north of the surface circulation center, it can have no direct impact on the intensity of the surface P_{min} (i.e., associated with C).

3.3.3. Development of MCS2: Development and merger of the MCV

The midlevel streamlines exhibit confluence immediately behind the leading line (Figs. 3.5d) of the bow-shaped segment of MCS1, where the RTF and FTR flows meet. While the RTF flows are not very strong, the convergence tends to cause the

development of descending motion along the flow interface (e.g., see Houze et al. 1989), and moist downdrafts below (see Fig. 3.7a), leading to the subsequent suppression of deep convection along the leading line (cf. Figs. 3.5d and 3.5e). As the leading line of MCS1 dissipates on the eastern side of the developing MCV trough (Fig. 3.5d), MCS2 begins to develop on its western side. The near-MCV environment is well known as favorable for the rejuvenation of convection, and MCS2 develops where low-level flow impinges on the cold pool left by MCS1 (Fig. 3.7a).

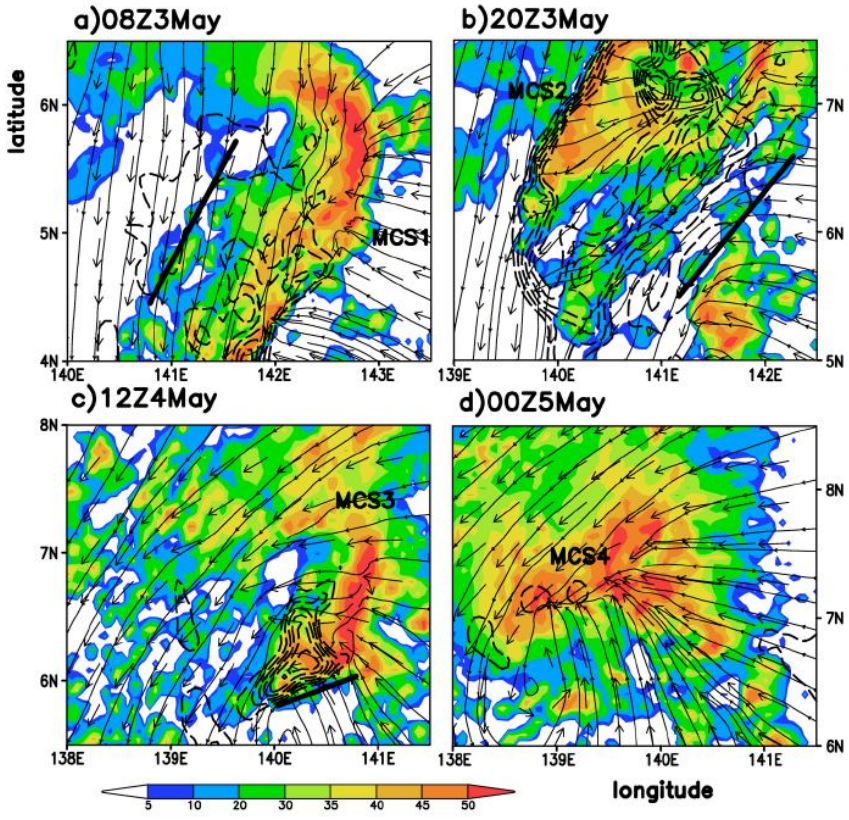

Figure 3.7. Horizontal distribution of the horizontal flow vectors, streamlines, and radar reflectivity (shaded, dBZ) at 900 hPa, superimposed with the 950-hPa temperature (dashed at intervals of 0.2°C between 22 and 23°C) showing the cold pool associated with (a) MCS1 at 3/08-152; (b) MCS2 at 3/20-164; (c) MCS3 at 4/12-180; and (d) MCS4 at 5/00-192, from the 6-km resolution domain. Heavy solid lines in (a) – (c) denote the edge of the cold pool where the subsequent MCS develops.

MCV V_2 continues to intensify behind the leading line of MCS2 (Fig. 3.5f), and a vertical cross section through V_2 shows that the midlevel MCV at its mature stage has a diameter of about 50 km and a depth of 400 hPa (Fig. 3.6b). It intensifies through vortex stretching associated with the midlevel convergence. The leading line of MCS2 loses its convective signature by 4/04-172, but V_2 persists and merges with A (see AV in Fig. 3.5h). Note that similar to the conceptual model of Houze et al. (1989), the MCV coexists with stratiform clouds as it moves northwestward. This vortex-vortex merger of a convectively generated vortex with the WWB-vortex A, and the resulting intensification of the midlevel cyclonic vorticity, can be considered as the "storage" of cyclonic vorticity for the subsequent TCG after the cyclonic circulations at all levels become vertically coherent. Of course, even after the midlevel merger discussed above, the vortex still exhibits significant tilt (Fig. 3.5h), so TCG is not yet impending.

It is evident from Figs. 3.5e-h that this pre-genesis stage consists of two related convective episodes: the decay of an eastward-propagating bow segment MCS1 and development of a weaker northwestward-propagating bow segment MCS2, both associated with the MCV (i.e.,V_2) formation. Together they appear to account for the amplification of the midlevel rotation. Apparently, the present pre-TCG convective features differ substantially from those shown in other TCG cases (e.g., Kieu and Zhang 2009; Braun et al. 2010), likely because the rotation is still very weak at this stage of genesis, while other studies focus on more intense circulations.

3.3.4. MCS3: Transition to a full spiral rainband

Until now, we have ignored the auxiliary precipitation features, including those occurring north of the shallow lower-tropospheric warm-cored vortex C. After the merger of V_2 and A into AV in the midtroposphere, another cycle of squall-line development (MCS3), closely resembling MCS1, takes place on the downtilt right side of the tilted WWB-vortex. MCS3 is likely triggered by the low-level flow that impinges on the cold pool left by MCS2 (Fig. 3.7b). This convective episode includes the generation of a squall line, a trailing stratiform region in the northern semicircle of AV (Fig. 3.5i), albeit much less extensive than that of MCS1 due to the smaller spatial extent of FTR flows (cf. Figs. 3.5i and 3.5a), and a bow-shaped convective segment with significant midlevel confluence/convergence (Fig. 3.5j). Associated with the bow-shaped convective region is the development of a RTF flow at the central portion and a FTR ascending flow with intense cyclonic vorticity along the leading line, which all resemble those associated with MCS1 (cf. Figs. 3.6a and 3.6c).

Two significant differences between MCS1 and MCS3 are apparent from Fig. 3.6c. The magnitude of midlevel vorticity is greater, and the RTF flows are stronger. Both differences are likely attributable to the fact that the midlevel vortex in which MCS3 develops is stronger after the merger. However, even though the RTF flow at 4/12-180 is more extensive than that of MCS1 at 3/08-152, a well-developed MCV fails to develop in MCS3 (Fig. 3.5j) because of the reduced vertical tilt of the WWB-vortex. That is, the horizontal distance between the midlevel and 900-hPa vortex centers (i.e., AV and C) has decreased from about 450 km at 3/00-144 to 200 km by 4/16-184. As a result, an arc-shaped rainband associated with low-level vortex C is

displaced northward to intersect with the southern part of MCS3 (cf. Figs. 3.5i and 3.5j), gradually eliminating the bow-shaped portion of the leading line (cf. Figs. 3.5j and 3.5k). The convective remnants of MCS3 advect within the midlevel circulation.

As the vertical tilt of the WWB-vortex centers is further reduced, convection along the arc segment intensifies after 4/16-184, likely associated with enhanced lifting associated with a cold pool left by MCS3 (Fig. 3.7c). Of importance is that deep convection now occurs within 100 km from the vortex centers, with convective precipitation occurring at the midlevel vortex (AV) center and initiating to the north of the low-level vortex C. This latent heat release near the vortex center is more effective than before in deepening the surface cyclone (Hack and Schubert 1988). Thus, the genesis of Chanchu takes place shortly after the initiation of MCS4 (Figs. 3.5l,m).

3.3.5. MCS4: Formation of a spiral rainband of Chanchu

While the WWB-vortex becomes upright as a result of more than 5-days of convective organization and TCG begins at 5/00-192, its larger-scale rotational flows at individual levels still remain highly asymmetric, as indicated by the near-perpendicular streamlines at 900 and 600 hPa (Fig. 3.5m). The asymmetric circulations allow the generation of deep convection close to the surface cyclone center (e.g., see Fig. 3.7d). Moreover, the low-level inflow into (outflow from) the rainbands is highly convergent (divergent), leading to the formation of a well-developed spiral rainband, defined as MCS4, along nearly the low-level streamlines (Figs. 3.5n-p). Another way to explain the asymmetric precipitation structures is via the vertical wind shear, i.e., precipitation occurs on the downshear left (Frank and

Ritchie 1999; Black et al. 2002). Fig. 3.2b shows that the 900 – 400-hPa shear is westerly, and thus peak convection occurs to the north. This result highlights the importance of (low-level) asymmetric flows in determining the distribution of deep convection, in addition to the vertical wind shear and other environmental factors.

Unlike MCS1 – MCS3, MCS4 does not exhibit significant moist downdrafts due to the continued moistening of columns in the inner-core region (Fig. 3.7d). A vertical cross section along the inner-core portion of the spiral rainband (Fig. 3.6d) shows prevailing cyclonically slantwise upward motion that is peaked at the midlevel, and convectively generated vortices in the inner core of MCS4, just like those typically seen in the eyewall of a mature TC. In this sense, MCS4 is unique compared to MCS1 – MCS3. In fact, the four MCSs have different characteristics in terms of orientation and shape, generation of MCVs and moist downdrafts, and dynamical lifting mechanisms. Although more case studies are needed, the evolution of the different MCS modes may be somewhat representative of convective characteristics leading to TCG from a larger-scale tilted vortex.

3.3.6. Convective contribution to the system vorticity

Fig. 3.8 summarizes the vorticity contributions of the MCSs to the system-scale rotation at 12 h intervals; the system scale is defined by an area of 800 km × 800 km centered between the peak convection and the lower- and midlevel circulation centers. In general, the vertical profiles of the system-scale relative vorticity show a peak value in the midlevels (low levels) prior to (after) 4/12-180. The local midlevel peak is most pronounced for the 3/00-144 profile, which is likely related to the enhancement of midlevel vorticity in the vicinity of the large area of stratiform

precipitation (cf. Figs. 3.8 and 3.3c). Continued convective development accounts for the amplification of the system-scale low-level cyclonic vorticity, though not necessarily near the low-level center. To see the net convective contribution to the system-scale vorticity, we also plotted in Fig. 3.8 the vertical profile of the mean relative vorticity from the dry run at 3/00-144. The differences in the 3/00-144 profiles between the ctl and dry runs is dramatic. The dry vortex is peaked near 850 hPa, while the full physics vortex is peaked in the midlevels. This difference is due entirely to the influence of precipitation processes.

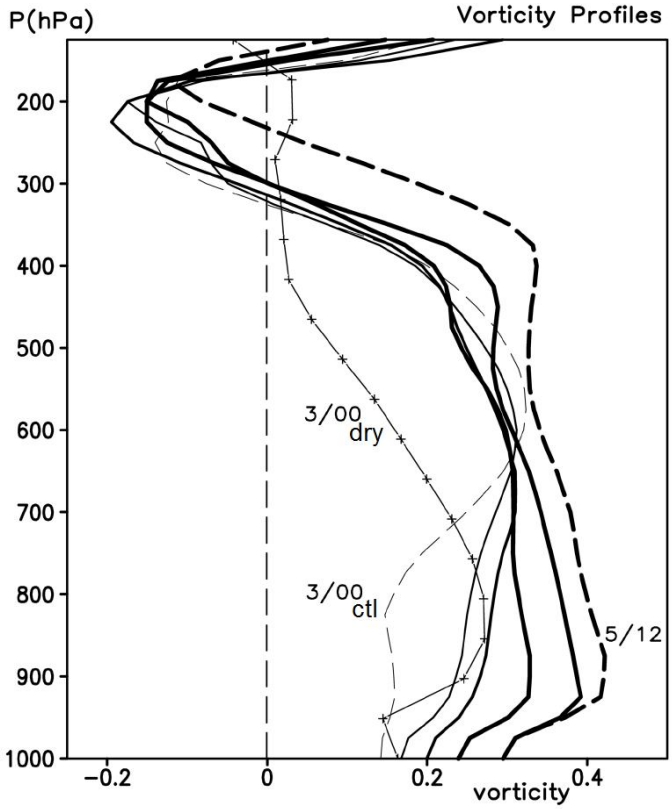

Figure 3.8. System-following area-averaged (800 km × 800 km) vertical profiles of relative vorticity ($x10^{-5}$ s^{-1}) at 3/00-144 (light dashed), 3/12-156 (lightest solid), 4/00-168, 4/12-180, 5/00-192 (heaviest solid), and 5/12-204 (heavy dashed) from the 6-km resolution control simulation domain, as compared to a profile from the dry simulation at 3/00-144 (marked with "+" signs).

3.4. Tropical transition of the baroclinic vortex

We have shown above the transformation of the tilted WWB-vortex to an upright one involving the baroclinic to tropical transition, similar to that discussed by Davis and Bosart (2004). Clearly, it is the various MCSs, especially their associated vortices as shown in the preceding section that are responsible for such a tropical transition. However, it remains uncertain how the pre-existing vortex interacts with the convectively generated cyclonic vorticity, leading to TCG. For this purpose, Fig. 3.9 shows the vertical cross sectional evolution of the relative vorticity, tangential winds and thermal fields associated with the WWB-vortex. Note that the direct influences of the MCSs could not be included in the cross sections, because they occur in the northern semicircle of the vortex (see Fig. 3.5). In essence, Fig. 3.9 shows the tilted structure of the vortex, while the precipitation processes occur on the downtilt-right.

It is evident from Fig. 3.9 that the WWB-vortex reduces its vertical tilt during the pre-genesis period (Figs. 3.9a-g). For example, the horizontal distance between the 500- and 900-hPa vortex centers (i.e., A and C) decreases from 550 to 200 km during 3/12-156 – 4/12-180. Meanwhile, the midlevel vortex A amplifies in magnitude and depth as a result of the absorption of the MCV and convectively generated vorticity from several MCSs, as discussed in section 3.4. The lower-level circulation C also intensifies with time, though more irregularly, and its depth remains below 600 hPa until 4/12-180. As a result, the tilted vortex exhibits two vorticity centers with large asymmetries in circulation prior to genesis (see Figs. 3.9a-e), unlike that observed in a dry simulation (not shown), in which the relative

vorticity is more uniformly distributed in a thin layer tilted from 400 hPa to the surface layer (not shown). The dry simulation is performed by turning off diabatic heating while holding all the other parameters identical to the control run presented in Chapter 2.

There are also two radii of maximum wind (RMW): one in the 500-600 hPa layer and the other near the surface, which persist even 12 h after genesis, i.e., at 5/12-204 (see Figs. 3.4b and 3.9h). The midlevel peak tangential wind in the cross sections increases from 12 to 21 m s^{-1} while the RMW decreases from near 500 km at 3/00-144 to 150 km at 4/18-186, and about 40 km at 5/12-204, indicating the spin-up of the midlevel circulation. Note that all the cross-sectional changes take place in a zone where little precipitation is present, as compared to the upright low-level circulation in which deep convection develops near its center.

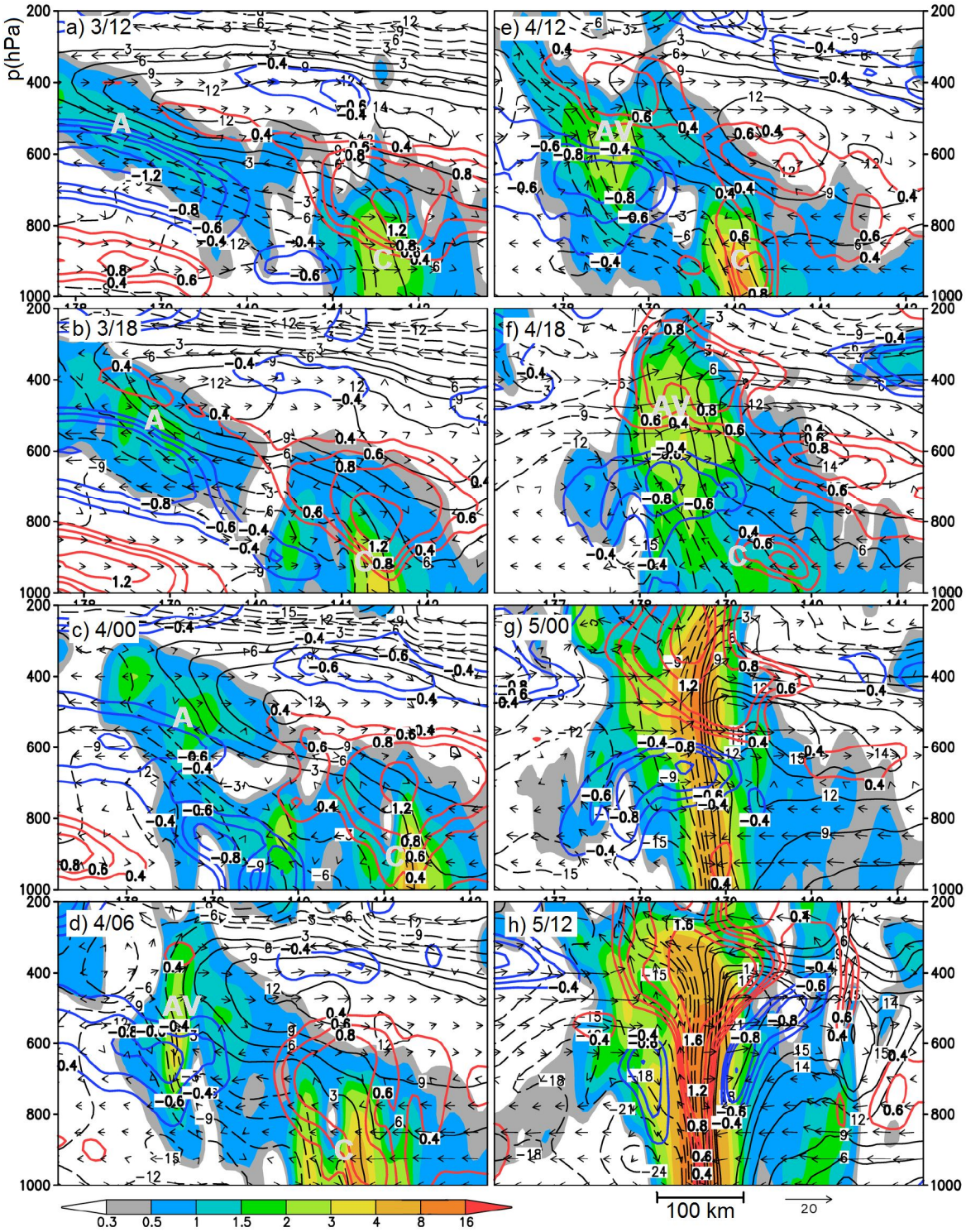

Figure 3.9. As in Fig. 3.4b, but for (a) 3/12-156; (b) 3/18-162; (c) 4/00-168; (d) 4/06-174; (e) 4/12-180; (f) 4/18-186; (g) 5/00-192; and (h) 5/12-204 from the 6-km resolution domain. Each field has been laterally averaged within a 36-km to show more representative features.

Fig. 3.9 also shows again the presence of the large positive vertical shear in tangential winds across the midlevel tilted rotational layer. The tilted WWB-vortex is cold-cored with a warm layer above. Of importance is that this warm layer increases in depth and intensity, and becomes a warm column aloft as the midlevel circulation A intensifies. By comparison, the low-level circulation is warm-cored, with little vertical shear below 700 hPa. Despite its occurrence near the equator, a thermal gradient of 2.4°C $(250\ km)^{-1}$ between the cold and warm core coincides qualitatively well with the large vertical wind shear in the vortex layer (e.g., Fig. 3.9a).

Of particular relevance to the trigger of genesis in the present case is the build-up of a warm–cored column above the low-level circulation. Although such a warm-cored column is present even earlier than 3/00-144, it is too shallow and weak to cause a large pressure drop with respect to its equatorial environment. Furthermore, because of the two distinct circulations of the upright lower- and the tilted midlevel circulations, the relatively colder air mass in the latter system tends to erode into the columns of the low-level system (e.g., see Figs. 3.9e-g), thus suppressing convective development in the southwestern quadrant of the WWB-vortex where weak subsidence prevails. As mentioned before, TCG occurs as the tilted WWB-vortex becomes upright. Obviously, *the essence of this upright vortex structure is that it facilitates the superposition of the upper-level and lower-level warm columns, leading to the rapid drop of central pressure or the genesis of Chanchu (Fig. 3.9g,h)*. In this regard, the convective contribution of cyclonic vorticity at the system scale, as shown in Fig. 3.8, should be considered as the balanced warm core congregated by

the MCSs combined with a pre-existing disturbance that could cause hydrostatic pressure falls at the surface.

The trigger of TCG has recently attracted some attention in the recent literature. Kieu and Zhang (2008) show the important role of vortex merger in the rapid increase of surface heat fluxes and intensification of Tropical Storm Eugene (2005). From the simulation of an idealized mesovortex, Nolan (2007) finds that the key to TCG is the convective moistening over a sufficient depth of the troposphere in the core region of the vortex. To examine if the present TCG scenarios fit the framework of Nolan, a height-time cross section of several area-averaged quantities during the 2-day pre-genesis period is given in Fig. 3.10, which shows that the relative humidity (RH) and equivalent potential temperature (θ_e) remain nearly constant prior to 3/18-162, with a RH of 80% at 950 hPa. Both exhibit rapid increases near 4/00-168. That is, the system-scale RH of 80% extends to 800 hPa after the life cycles of MCS1and MCS2. Such high RH is considered by Nolan (2007) as one of the preconditions for TCG, but the genesis of Chanchu and rapid increase in surface fluxes and surface θ_e value in the present case do not occur until 24 h later. The delay in TCG after the moistening implies that a *deep-layer humidification of the troposphere is a necessary but not sufficient condition for TCG*. In order for the WISHE process to be operative, it is necessary to build up a warm-cored column near the center of a surface cyclone. This can only occur when the tilted vortex becomes upright in the vertical. The processes associated with the warm-core transition will be expounded upon in Chapter 4.

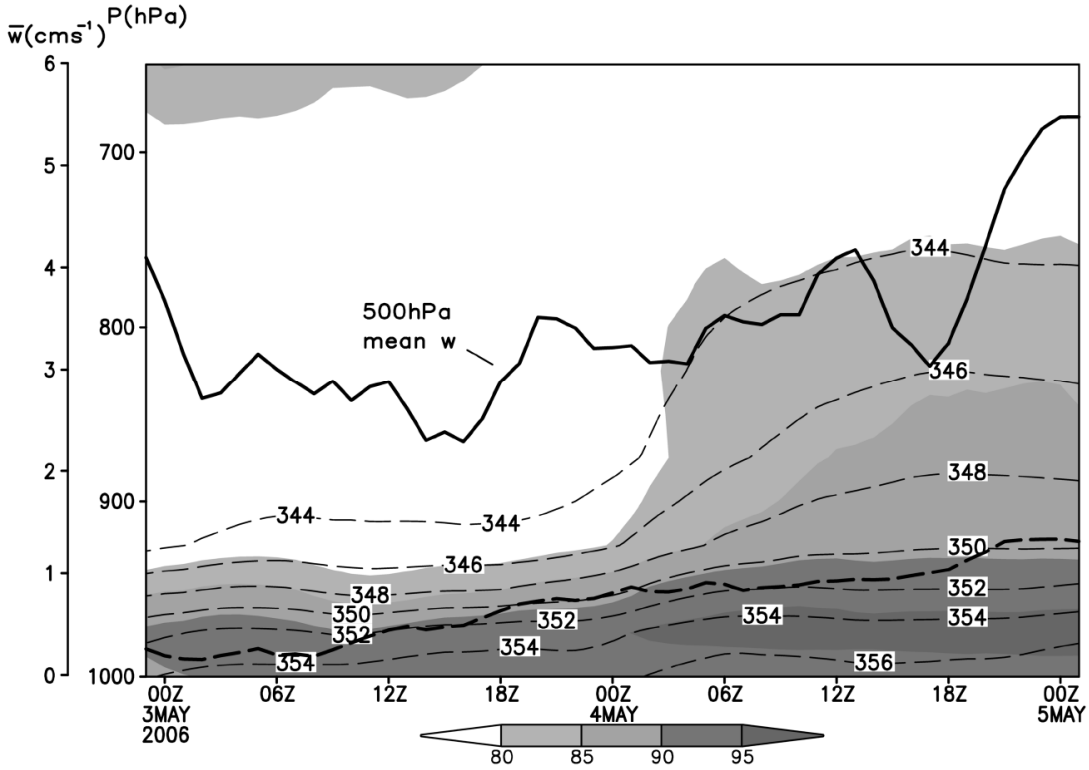

Figure 3.10. Time-pressure cross section of the system-averaged relative humidity (shaded, %) and equivalent potential temperature (θ_e, dashed contours at intervals of 2 K above 344 K) during the period of 3/00-144 and 5/00-192 from the 6-km resolution domain. See Fig. 3.5 for the subdomain sizes at different times. Domain-averaged time series of vertical motion (cm s^{-1}) at 500 hPa (solid) and 950 hPa (dashed) are also shown.

3.5. Summary and conclusions

In this chapter we document the organization of precipitation on the downtilt-right of the pre-Chanchu disturbance during the two days prior to its genesis. We find that the simulated storm intensifies via midlevel vortex mergers prior to genesis. The increase in midlevel vorticity during the two days prior to genesis is facilitated by persistent downtilt-right precipitation that organizes into four distinct MCSs (MCS1 – MCS4). MCS1 and MCS3 take on the appearance of a tropical squall line, with leading line deep convection and stratiform precipitation to their north. Both MCSs exhibit cold pools that serve as the foci for initiation of the subsequent MCS.

The second MCS, which evolves more than a day prior to genesis, develops in its stratiform region an intense MCV, V_2, which merges with the pre-Chanchu vortex in the midlevels. The resulting midlevel vortex exhibits greater depth and magnitude post-merger. It is found that the orientation of the MCS2 with respect to the midlevel flow aids in the generation of the anomalously strong MCV by creating an area of strong horizontal convergence behind the leading line. MCS2 also develops a significant cold pool near the surface.

The final MCS4 is larger than any of the first three MCSs, exhibits broad and deep slanting updrafts and neither cool downdrafts nor a near-surface cold pool. Apparently, the evolution of the first three MCSs during the two days prior to genesis facilitates a rapid increase in the low-level RH, which serves to suppress downdrafts within MCS4. MCS4 develops into the first primary rainband of Chanchu. The primary conclusion from the present study is that the initial westward tilt of the cold-core pre-Chanchu vortex, combined with persistent downtilt-right precipitation, is a favorable scenario for the eventual vertical alignment and TCG as a warm-core vortex.

The tendency of the vortex to become vertically upright is critically dependent on the persistence of deep convective precipitation, toward which the low- and midlevel vortices deflect. In the absence of precipitation, Jones (1995) found that the circulation centers do not lock phase in the vertical. In the real atmosphere, the intermittence of precipitation could depend on various factors including humidity, since the precipitation must be triggered by weak downtilt-right isentropic ascent, and could explain why not all westward-tilted vortices culminate in TCG. In fact, in a

recent study of the impact of the modulation of TCG by the MJO, Camargo et al. (2009) found that RH is the most important contribution of the MJO to TCG.

It is obvious that TCG occurs as a complex 3D process that involves the interaction of a tilted vortex and convection. Up to now, however, we have neglected to discuss the development of near-surface vorticity, which remains the most immediate issue for TCG research. Chapter 4 will focus on the processes by which the *surface* circulation intensifies as the vortex becomes vertically upright.

Chapter 4: Storm-Scale Genesis of Chanchu

4.1. Introduction

A sufficient mechanism or a so-called trigger of tropical cyclogenesis (TCG) continues to elude understanding. Precursor disturbances of wide-ranging origin can provide favorable conditions for TCG, but the processes that comprise TCG within each precursor scenario are still largely unknown. The general lack of understanding of TCG can probably be ascribed to the dearth of comprehensive observational data in the global TCG areas, as the geneses of other rotating storms that occur over land (e.g. the midlatitude cyclone and the supercell) are more thoroughly understood. Might it be possible that TCG, similar to the evolution of other rotating storms, occurs in a relatively invariant manner despite the array of TC precursors?

The air-sea interaction (WISHE, Emanuel 1987) by which a pre-existing tropical disturbance can undergo self-sustaining intensification is well understood, but the manner in which the lucky minority of pre-existing disturbances reaches the threshold for the invocation of WISHE is the essence of the TCG problem. From a dynamic point of view, the vorticity must increase sufficiently near the ocean surface, and at a scale significantly smaller than that of its precursor. Recent studies on TCG frame the problem of near-surface vorticity production in the top-down, bottom-up paradigm, where the threshold for WISHE is reached by stochastic processes. For example, deep vortical hot towers (Hendricks et al. 2004) may amalgamate and result in the upward growth of vorticity, or mesoscale convective vortices (MCVs) may interact (Simpson et al. 1997) in the midlevels and increase their penetration depth

toward the surface. The implicit stochasticity in both TCG pathways provides no obvious avenue by which to improve the predictability of TCG.

The TC is not the only phenomenon for which the development of an intense vertical column of mesoscale vorticity persists as a research issue. Supercells (Browning 1964) are intense rotating thunderstorms, characterized always by strong mesocyclones in the midlevels and sometimes by strong low-level rotation and an attendant tornado. The mechanisms responsible for the generation of midlevel vorticity in supercells are well known as the tilting of environmental shear-generated horizontal vorticity and subsequent stretching in deep updrafts (Barnes 1970; Rotunno 1981). While tilting of horizontal vorticity by an updraft creates two symmetric counter-rotating vortices, the vast majority of supercells exhibit cyclonic rotation (Davies-Jones 1985). Maddox (1976) and Klemp and Wilhelmson (1978) showed that the predominance of cyclonic supercells is associated with their preferred development in environments in which the shear vector turns cyclonically with height. The turning of the shear vector selectively enhances (suppresses) updraft growth on cyclonic (anticyclonic) flank of the updraft (Rotunno and Klemp 1982), leading to net generation of cyclonic midlevel vorticity.

The mechanisms for low-level vorticity generation in the supercell are similarly related to the cyclonically-turning shear vector, which favors the development of low-level streamwise horizontal vorticity (Davies-Jones 1984), i.e., that which has a component parallel to the flow. Parcels with streamwise vorticity immediately acquire cyclonic vorticity when tilted by an updraft and are subsequently stretched (Klemp and Rotunno 1983). A reason for the relative success in

understanding supercell low-level spin-up is that the convective structure of the supercells that sometimes spawn tornadoes is well-known and can be identified prior to the development of the tornado, allowing rapid mobilization of nonstationary observation networks near the incipient storm (e.g. the VORTEX field experiment, Rasmussen et al. 1994). Up to now, however, no such general structure of tropical convection that may spawn a mesoscale TC circulation has been identified; of course, observational challenges in the TCG environment are enormous.

Lemon and Doswell (1979) draw an analogy between the qualitative similarities of the supercell and the midlatitude cyclone, with the primary difference being horizontal scale. Tornado formation occurs in an area known as the hook echo, which is a radar manifestation of the downdraft wrapping around the updraft. The explosive midlatitude cyclone exhibits a similar comma-shaped cloud structure at peak intensity, as the storm occludes. The comma cloud typically marks the end of midlatitude baroclinic intensification, as the upper- and lower-level circulation centers become vertically stacked. The location of minimum surface pressure in both a tornado and a midlatitude cyclone occurs at the interface of the wrap-around precipitation and the clear slot. Both systems reach peak intensity as the clear slot develops, and both weaken soon after occlusion. Marquis et al. (2009) show observations of a Texas tornado that appears completely encircled by low-θ_e air at peak intensity, i.e. after the occlusion.

In terms of horizontal scale, the TC falls between the supercell and the midlatitude cyclone, both of which undergo amplification of near-surface vorticity. The TCG process has not been thoroughly compared to the geneses of other rotating

storms up to now for an obvious reason: the other geneses occur in highly sheared environments, while it is widely understood that vertical shear is unfavorable for TCG. The few studies on the baroclinic development of TCs are thus limited in number and confined to the midlatitudes where shear can be significant (e.g. Davis and Bosart 2001; Zhang and Bao 1996). Hulme and Martin (2009) found that TCG is favored when the occlusion of a midlatitude cyclone occurs warm ocean water, the so-called tropical transition.

While recent studies on TCG seem to represent a growing consensus that the bottom-up route is more plausible (Houze et al. 2009; Kieu and Zhang 2009) than top-down, the present chapter aims to frame the TCG problem in the context of more well-understood rotating storms and provide evidence that TCG may indeed proceed in a more deterministic manner than that provided by the top-down, bottom-up frameworks. As a first step, it has been noticed that genesis is often preceded by a large, coherent MCS that contains an exceptionally broad, downdraft-free updraft region (Houze et al. 2009; Hogsett and Zhang 2010a??) and can take on the comma (or more conventionally "spiral band") shape (Zipser and Gautier 1978; Stossmeister and Barnes 1992). The present chapter revisits TCG in the deep tropics as a unique sub-synoptic phenomenon that, at least for the present case, can be placed in a spectrum of rotating storms that spawn near-surface vortices, at a scale between midlatitude cyclones and the supercell.

In Chapter 2, we presented a cloud-resolving simulation of the genesis of Typhoon Chanchu, which developed in the near-equatorial west Pacific during the active phase of the MJO. The westerly wind burst associated with the MJO

modulated low-level vorticity and convection, and Chanchu developed after an eight-day pre-genesis period??since a closed low-level circulation??. We found that because the WWB t height, the resulting vortex also tilted westward with height, leading to forced isentropic ascent on its downtilt-right side. During the lead-up to genesis, the tilted vortex became more vertically upright in the presence of persistent downtilt-right precipitation.

In Chapter 3, we investigated the mesoscale evolution of the pre-genesis, downtilt-right precipitation, which took the form of squall lines and convective clusters with large areas of stratiform precipitation. One of the MCSs left a strong MCV in its wake that merged with and strengthened the midlevel circulation, in the manner discussed by Ritchie and Holland (1997). The first three of four MCSs left cold outflow near the surface, along which the subsequent MCSs developed. The fourth and final MCS (i.e., MCS4) left no cold pool prior to genesis, though it exhibited larger size than any of the previous three and exhibited a downdraft-free updraft region and a spiral shape, similar to those investigated by Zipser and Gautier (1978) and Houze et al. (2009). Apparently, the first three MCSs served to precondition the environment by raising low- and midlevel RH.

In Chapter 4 of this dissertation, we present results from the finest 2-km nest of the WRF simulation discussed in Chapter 2 and emphasize the evolution of MCS4 in a preconditioned and sheared (at the storm scale) environment. The finest nest tracks the low-level pre-Chanchu circulation from 3 – 7 May. The purposes of the present chapter are to (i) demonstrate how the genesis of Chanchu is related to the evolution of MCS4, which deforms into a spiral band and eventually occludes; (ii)

show that near-surface cyclonic vorticity is preferentially generated along a near-surface convergence zone; (iii) propose a unique pathway to genesis.

The next section provides an overview the storm-scale evolution of the incipient Chanchu before and after the threshold of TCG. Section 4.3 discusses the mechanisms by which the midlevel circulation intensifies prior to TCG. Section 4.4 shows the processes by which near-surface vorticity is rapidly enhanced and concentrated into a TC-scale circulation. Section 4.5 discusses the implications of the occlusion of MCS4. Section 4.6 compares the present TCG and the geneses of other rotating storms, and conclusions are given in the final section.

4.2. Storm-scale evolution

In this chapter, we focus almost exclusively on the 24-h period centered on the onset of TCG, i.e. model hours 180 – 204, valid between 1200 UTC 4 May – 1200 UTC 5 May, hereafter 4/12-180 – 5/12-204. In this section we provide an overview of the near-storm environment, which we consider a roughly 500 x 500 km area that contains the entire tilted vortex and the relevant downtilt-right precipitation while following the storm.

4.2.1. 12 h prior to genesis

During the 12 h prior to genesis, the large scale vertical shear remains below 6 m s^{-1} (Fig. 2.8) and thus favorable for storm intensification. The storm scale 900 – 400 hPa shear, on the other hand, remains westerly (Fig. 4.1) with a nearly constant magnitude of 20 m s^{-1} throughout the period under study. Since the incipient disturbance exhibits a northwest-southeast vertical tilt and peak vorticity occurs in the midlevels (see Fig. 4.2), the westerly 900 – 400 hPa shear in Fig. 4.1 can be

considered as "self-imposed" by the midlevel portion of the tilted vortex onto that in the low levels. Because the relative vorticity of the pre-Chanchu disturbance diminishes above 500 hPa (see Fig. 4.2), perhaps the typical shear calculation that extends into the upper troposphere is not appropriate during the pre-genesis period. For this reason, we confine the subsequent discussion to the vertical shear between the 400 and 900 hPa levels.

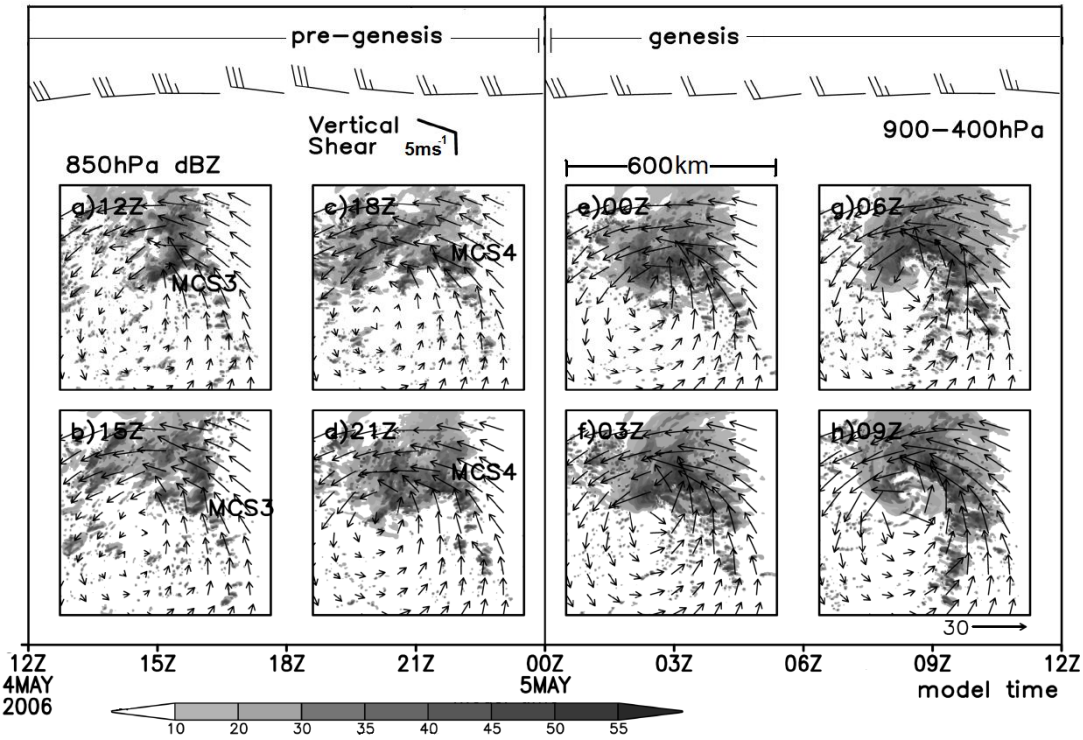

Figure 4.1. Time series (90 min) of the area-averaged (500 x 500 km) vertical shear (m s^{-1}) between 900 – 200 hPa (heavy barbs??) and 900 – 500 hPa (light barbs??) between 1200 UTC 4 May – 1200 UTC 5 May. In (a) – (h), the horizontal distribution of 850-hPa precipitation fields (dBZ, shaded) from the finest 2-km nest, superposed by the 850-hPa flow vectors from 1200 UTC 4 May – 1200 UTC 5 May, at 3-h intervals.

The precipitation during pre-genesis (Fig. 4.1a-d) is triggered and maintained by forced isentropic ascent on the downtilt-right (i.e. north) side of this tilted vortex (Jones 1995; Frank and Ritchie 1999), as detailed in Chapter 2, while the downtilt-left-also downshear le half remains largely precipitation-free. The downtilt-right precipitation consists of

MCS3, which propagates from west to east and decays (Fig. 4.1a,b), and MCS4, which subsequently develops along the cold pool ??was not discussed in Part II?? of MCS3 (Fig. 4.1c) a take on the spiral shape by 4/21-189 (Fig. 4.1d). As MCS4 intensifies, the magnitude of the area- and layer-mean vertical motion doubles during the 6 h prior to genesis (Fig. 4.2), during which time the vertical tilt diminishes from nearly 200 km to less than 50 km (Chapter 3, Fig. 3.9). During the rapid intensification of MCS4, the mean 600-hPa vorticity increases by 7 x 10^{-5} s^{-1} during the 9 h prior to TCG (Fig. 4.2), while the mean vorticity at 900-hPa increases by only 4 x 10^{-5} s^{-1} and the minimum pressure remains relatively constant. The mechanisms by which the midlevel vortex intensifies prior to the onset of TCG will be discussed in the next section.

4.2.2. Onset of genesis

As mentioned above, the midlevel vertical shear does not diminish as TCG begins (Fig. 4.1). MCS4 transitions into a primary rainband (Figs. 4.1e,f), which is typical of incipient TCs (Willoughby et al. 1984), and by 5/03-195 the low-level circulation begins to exhibit a small-scale intense circulation south of the peak spiral band convection (Fig. 4.1f)-rewording??. By 5/06-198 (Fig. 4.1g) a nascent eye begins to appear and the comma shape is even more obvious. The persistence of a 20 ??m s^{-1} 900 – 400 hPa shear (Fig. 4.1) during TCG shows clearly that the vortex still exhibits some vertical tilt. As discussed in Chapter 2, only in the immediate vicinity of the circulation center is the vortex upright. The spiral band persists in a highly vertically sheared environment. Thus the downtilt-right thinking can be applied to the pattern of precipitation for some time after the onset of genesis??why not using downshear left??. The notion that exhibits less tilt that the far-field flow can be seen in Fig. 4.1h: a quasi-axisymmetric

area of precipitation is obvious near the upright core, but the outer rainband continues to exhibit a spiral structure. The physical relationship between the spiral band and vertically sheared flow will be discussed in the next section.

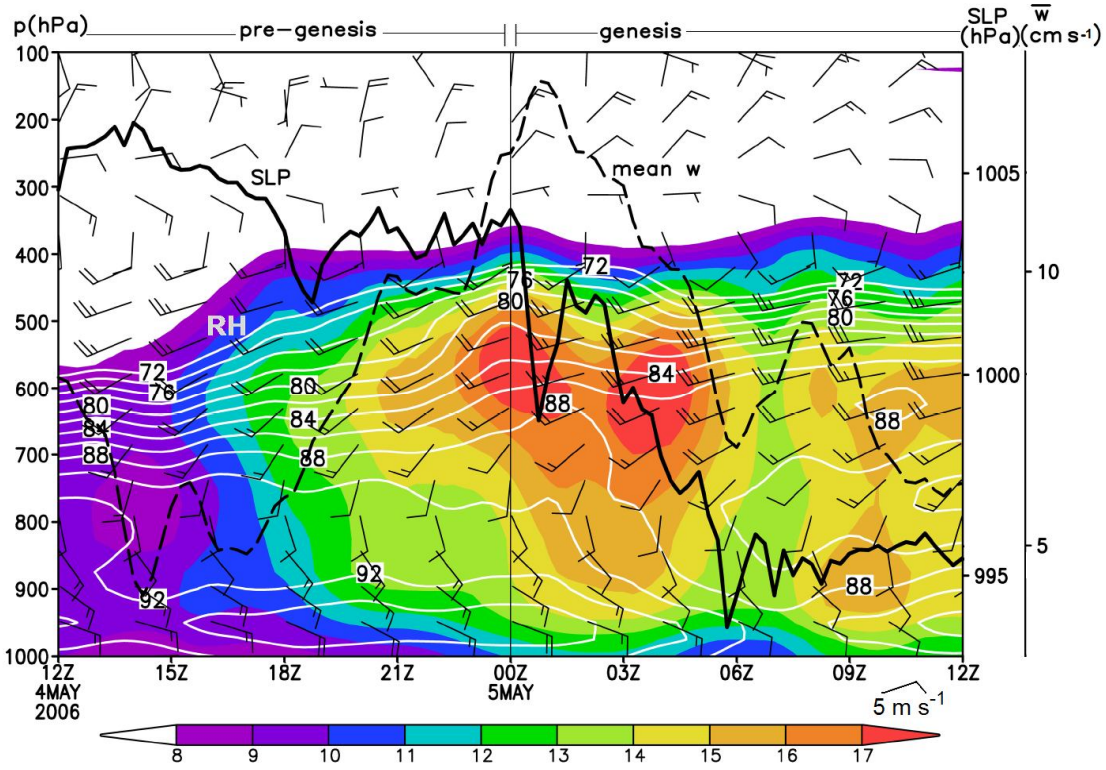

Figure 4.2. Time–height cross section (15 min) of the area-averaged (500 x 500 km) relative vorticity (x 10^{-5} s^{-1}, shaded), relative humidity (%, contoured at intervals of 3% above 72%), and wind barbs (m s^{-1}, 2-h intervals). The minimum surface pressure (solid contour, hPa) and the 900 – 400 hPa mean area-averaged (500 x 500 km) vertical motion (dashed, cm s^{-1}) are superposed. ??vorticity is not representative, explain why discontinuity & decrease after5/06

The minimum central pressure begins to fall rapidly near 5/00-192 (Fig. 4.2) and decreases by 11 hPa during 5/00-192 – 5/06-198. We consider this the onset of TCG. In Chapter 3, we show that during pre-genesis the mean vertical motion and RH increase in association with the low-level humidification and the intensification of MCS4, i.e., preconditioning (Nolan 2007). Interestingly, the storm-scale RH and mean vertical motion *decrease* during the first 6-h period of rapid deepening (Fig.

4.2). The temporary dehumidification and decreasing upward motion suggest the increasing prevalence of downdrafts in the low- and mid-troposphere??. A goal of this chapter is to reconcile the apparent discrepancy between midlevel downdrafts and concurrent rapid intensification. *How does rapid spin-up occur at the surface when the mean vertical motion is rapidly decreasing? ??plot area*down +area*up??*

After the initial 6-h deepening period, the surface pressure ceases deepening temporarily, low-level RH begins to increase again, and area-averaged low-level relative vorticity exhibits a temporary minimum (Fig. 4.2)??why. After this 6-h period of intensity maintenance, Chanchu deepens at a more constant rate throughout the remainder of the simulation (Chapter 3, Fig. 3.2a). *Why does intensification, in terms of minimum pressure, cease (temporarily) after the initial onset of TCG?* In the next two sections we attempt to answer the above questions.

4.3. Midlevel vortex enhancement

To understand genesis, we must first understand why the midlevel vorticity increases more rapidly than the near-surface vorticity prior to the onset of TCG??answered in Part II??. this end, we aim to understand the relationship between the vertical wind shear and the transition of MCS4 into a spiral band (c.f. Figs. 4.1d,h). The vertical structure of the wind profile in the highly-sheared, near-MCS4 environment may hold the key to genesis (Fig. 4.2).

4.3.1. Potential mechanism for midlevel generation

Supercell thunderstorms are also well-known to exhibit a rapid increase in cyclonic midlevel rotation due to their prevalence in environments with veering wind profiles (Fig. 4.3a). As shown by Rotunno (1981), the midlevel rotation in a supercell

arises due to the tilting of environmental westerly vertical shear by a vigorous updraft, which leads to a pair of counter rotating vertical vortices. However, because the shear vector rotates cyclonically with height (i.e., it veers), Rotunno and Klemp (1982) showed that dynamically-induced vertical pressure gradients develop on both flanks of the updraft such that the cyclonically rotating member of the pair (i.e. that to the right of the midlevel shear) is favored for enhanced vertical motion and new updraft growth. The vertical motion associated with the anticyclonic member of the tilt couplet, conversely, is suppressed. Thus environments with a cyclonically curved hodograph favor a net increase in midlevel cyclonic vorticity via tilting of shear-generated horizontal vorticity by updrafts.

Fig. 4.3b shows that the hodograph in the present case exhibits cyclonic turning with height, similar to that characteristic of the most intense supercells, which always develop intense midlevel mesocyclones and often spawn near-surface vortices. Of course, the hodograph is simply another method of representing the veering wind profile shown in Fig. 4.2. The implication is that every discrete updraft triggered in this environment will not only tilt environmental shear vorticity, but will acquire net cyclonic vorticity due to preferential generation on the cyclonic flank (in this case, to the south).

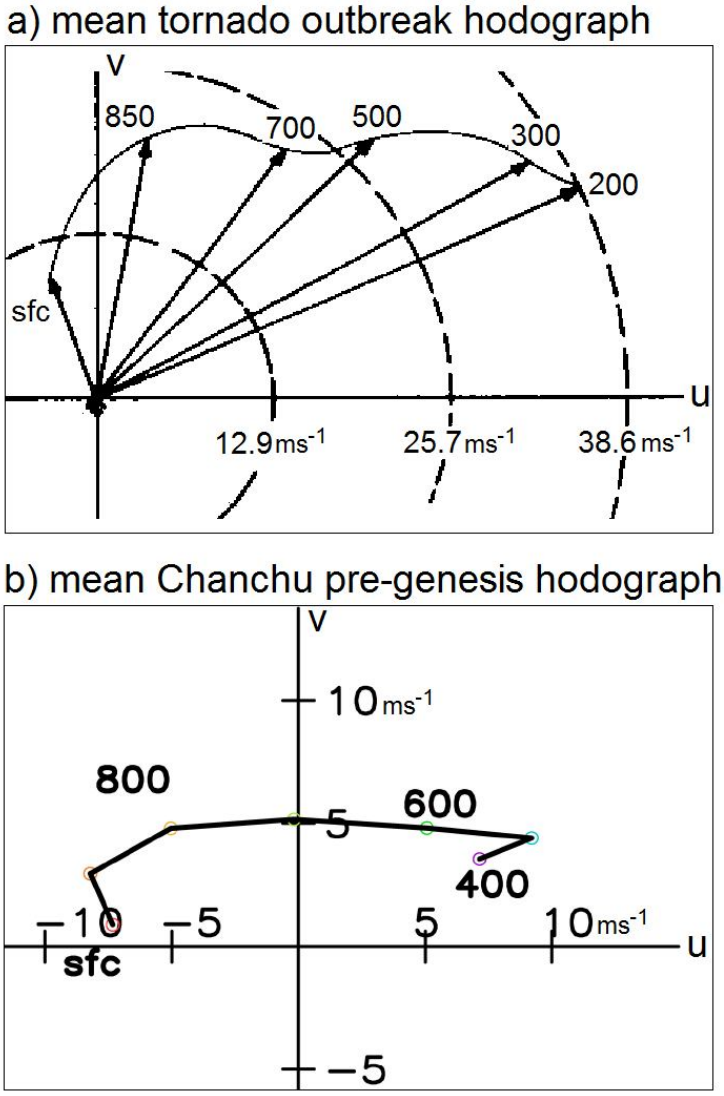

Figure 4.3. Hodographs for (a) the average of 23 soundings taken in the proximity of a tornado outbreak, adapted from Maddox (1976), and (b) the area-averaged (500 x 500 km) environment prior to the genesis of Chanchu. Note the cyclonic turning with height in (a) and (b).

4.3.2. Midlevel vortex structure

In order to demonstrate the mechanisms for the increase in midlevel vorticity, we show the storm-scale structure of the pre-Chanchu disturbance in Fig. 4.4, during the transition to genesis from 4/21-199 – 5/0330-195.5. The simulation captures a broad cyclonic circulation at 500 hPa (Fig. 4.4a), a poorly organized MCS4 (Fig.

4.4e) northwest of the 850-hPa circulation center at 4/21-189, and a weak convergence zone near the surface (Fig. 4.4i). The convergence zone separates a relatively low-θ_e airmass beneath MCS4 from the high-θ_e airmass, which feeds into MCS4 from the southeast. The temperature gradient across this convergence zone (not shown) does not exceed 1 K.

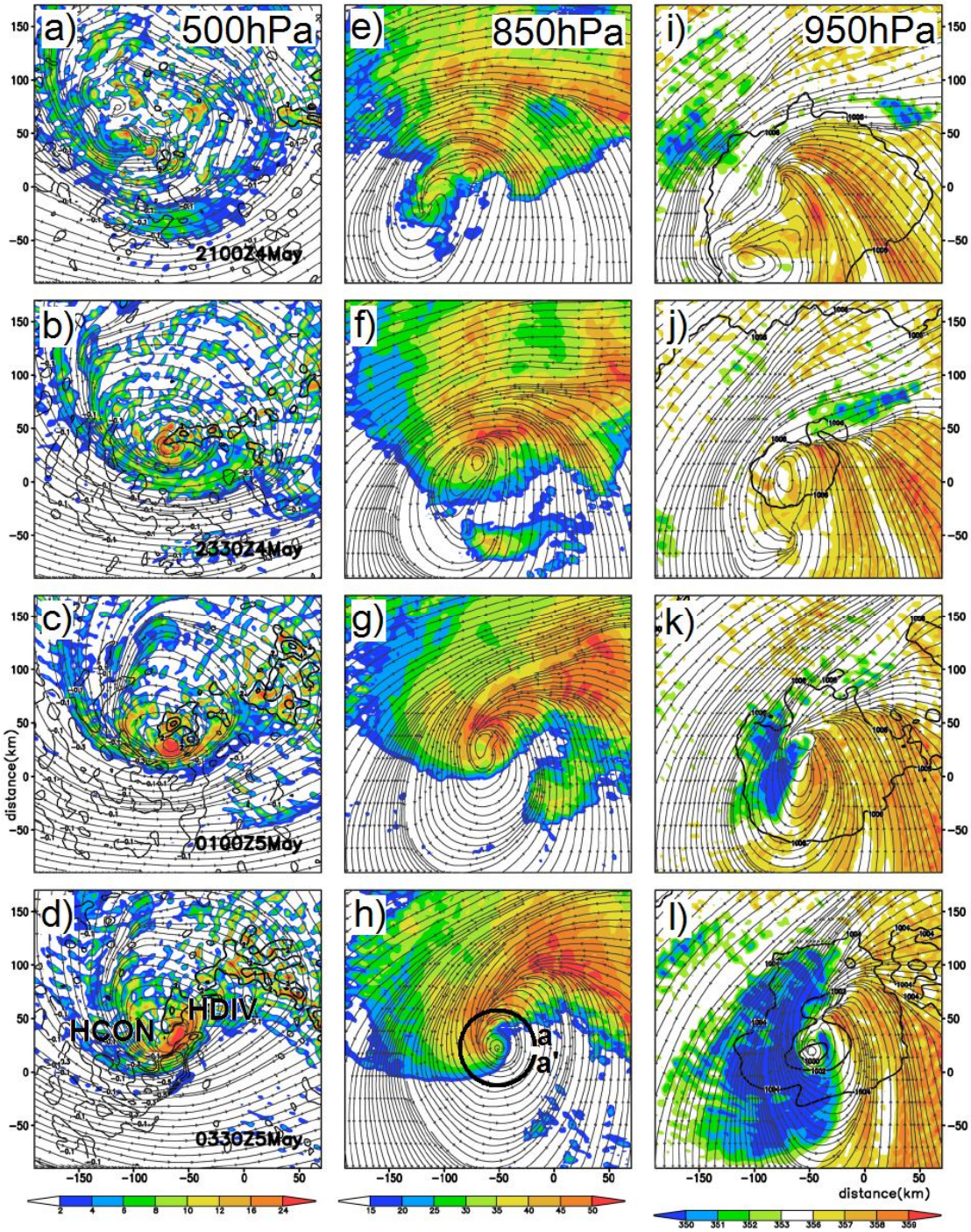

Figure 4.4. Horizontal distribution of (a-d, left panel) 500-hPa relative vorticity (x 10^{-5} s^{-1}), (e-h, center panel) 850-hPa radar reflectivity (dBZ), and (i-l, right panel) 950-hPa equivalent potential temperature θ_e (K), all shaded from 2100 UTC 4 May (top row) – 0330 UTC 5 May (bottom row) at 150-min intervals. In (d), areas of enhanced horizontal convergence (HCON) and divergence (HDIV) are shown. In (h), the path of the circular cross section (a – a') for Figure 4.7 is shown as the heavy solid arc. In (i-l), surface pressure (at intervals of 1 hPa) is contoured, and streamlines are superposed at each level. ??what are
the solid contours in a-d?? provide a reference point in each figure
Negative vorticity should also be plotted?? show vertical profiles of the area-averaged +ve and -ve vorticity

By 4/2330-191.5, a well-defined 500-hPa vorticity maximum develops within the circulation center (Fig. 4.4b)why??, and in association with enhanced midlevel difluence downstream ?? of the center (Fig. 4.4b), convection organizes along the increasingly sharp low-level?? convergence zone (Fig. 4.4j). Of interest is that the 500-hPa vorticity maximum develops not in the center of the 500-hPa circulation, as might be expected from a series of random vortex mergers. Instead it develops along the southern periphery of the broad midlevel circulation (Fig. 4.4b) and immediately to the south of the strongest upward motion (Fig. 4.4b).

The location of peak midlevel vorticity is not coincidental or random. Instead, the vertical motion associated with the intensifying convection tilts the horizontal?? shear vorticity, which leads to preferential generation on the southern flank of the updraft. The 500-hPa vorticity maximum develops at exactly the location where the 500-hPa flow passes over the 850-hPa circulation center (c.f.,??cf.?? Figs. 4.4b,f), i.e., where the horizontal shear vorticity?? is greatest (not shown), and to the south of the updraft maxima. This process is summarized in Fig. 4.5, and begins with the shear-generated horizontal vorticity that generally points northward in the midlevels (Fig. 4.5a). As updrafts associated with MCS4 tilt the horizontal vorticity, a vertical vorticity couplet (Fig. 4.5b) is created with anticyclonic (cyclonic) vorticity generation to the north (south). Because the shear??wind rather than shear?? vector turns cyclonically ??clockwise?? with height, t member of the tilting couplet is favored for strengthening (Fig. 4.5c) on the southern flank of the convection (Fig. 4.4b).??unclear?? On the northern flank of the updrafts, cyclonic vorticity is suppressed.

perhaps shear vector should be recalculated with smaller areas50x50km??if shear vector veers, so does vo

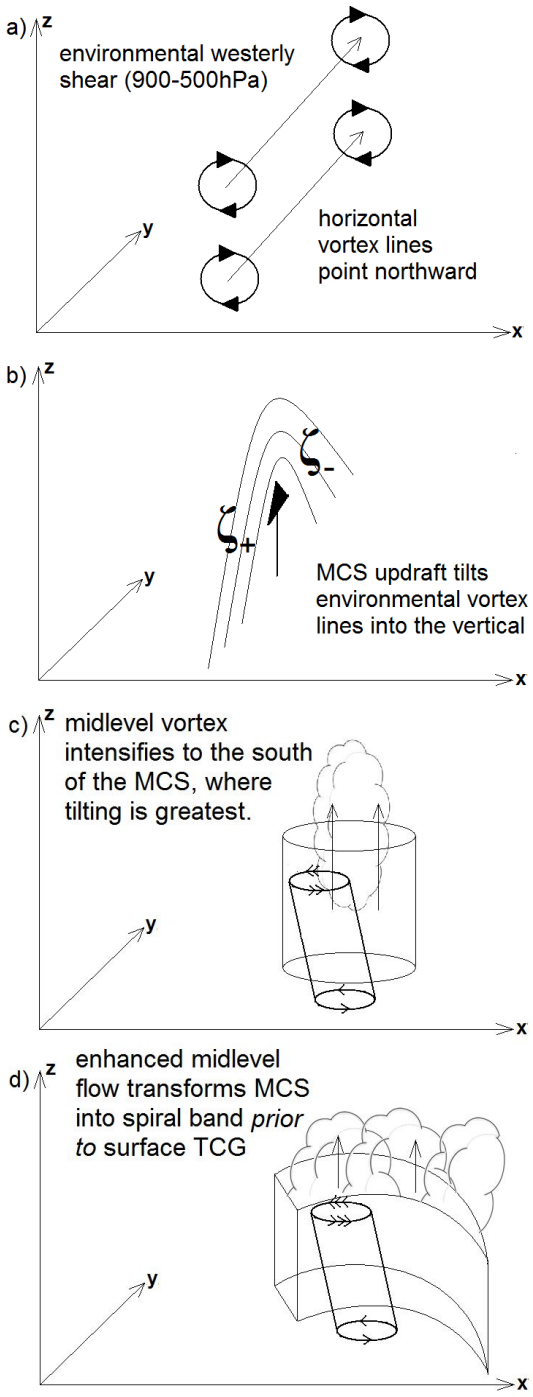

Figure 4.5. Conceptual model of midlevel intensification. C is unclear, d does not seem to be correct??

The increasingly intense midlevel vortex (Fig. 4.4c) remains peaked at the southern periphery of MCS4, which begins its transition into a spiral band (Fig. 4.4f) in response to increasing midlevel flow that advects the western (eastern) portion of

the MCS southward (northward). The only plausible explanation for the MCS-to-spiral-band transition is rapid midlevel vortex enhancement on the *southern flank* of the MCS??not right??. This process begins to occur prior to the onset of TCG (Fig. 4.5d), similar to the manner in which a supercell develops an inflow notch and "hook echo" just prior to the tornado phase. It is in this way that midlevel tilting-generated vorticity on the flank of the MCS4 triggers the transition from a general MCS into a spiral band??not right??. In section 4.4 we investigate the detailed structure of this convection in the context of the surface vortex spin-up.??need to show how vorticity helps organize convection??

In Fig. 4.6, we show the mean structures during the first 2-h period of TCG to further understand the ongoing processes. It is obvious from Fig. 4.6a that the location of the surface circulation occurs at the tip of the, for lack of a better term, "hook echo." However, because the circulation center in the midlevels is displaced slightly northwest of that in the low levels (cf. streamlines Figs. 4.6a,d), the local vertical shear in the core region remains large during this period. The implication of the vertical shear for the present discussion is that horizontal vorticity may be large, and thus in the vicinity of strong upward motion (or more specifically horizontal gradients of vertical motion), the vorticity tilting term may continue to be important for the evolution of the spiral band??unclear??.

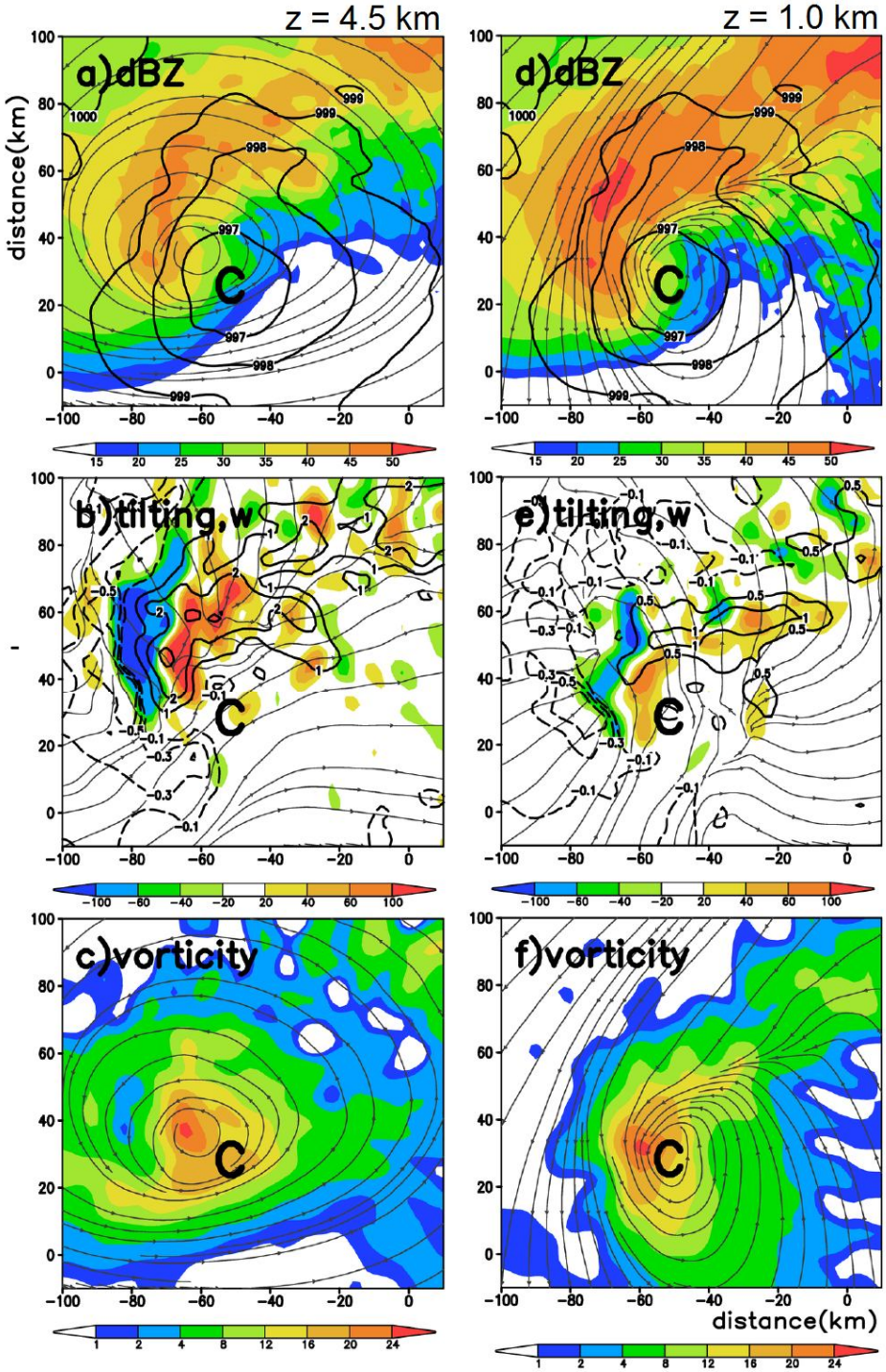

Figure 4.6. Horizontal distribution of radar reflectivity (dBZ, shaded, top row) and surface pressure (hPa, contours), the vorticity tilting term (x 10^{-8} s^{-2}, shaded, middle row), and relative vorticity (x 10^{-4} s^{-1}, shaded, bottom row) at 4.5 km (a-c, left panel) and 1 km (d-f, right panel), taken as the 2-h average during 0230 - 0430 UTC 5 May. The horizontal streamlines are superposed in the top and bottom panels, and the local vertical shear streamlines between (b) 3.5 – 5.5 km and (e) 0.2 – 1.5 km are superposed in the middle panel. What are the contours in b and e??

In fact, Fig. 4.6b shows that the midlevel vertical motion exhibits a spiral pattern associated with the updrafts ??redundant? within the convective band. The local vertical shear has a component perpendicular to the gradient of vertical motion within the spiral band (see shear streamlines in Fig. 4.6b). As the updraft within the spiral band tilts the shear-generated horizontal vorticity, a dipole structure appears in the vortex tilting term. The tilting enhances (suppresses) cyclonic vorticity radially-inside of the spiral band??but -ve vorticity is also large in Fig. 4.6??. This process is simply a modification of described in Fig. 4.5, and it has two consequences. First, midlevel vorticity exhibits a *net increase* to the downshear-right of the peak updraft, where the tilting is large (Fig. 4.4b-d), thus ensuring that the midlevel circulation center (and vorticity maximum, Fig. 4.4d) remains displaced toward the downshear-right flank of the peak convection (Fig. 4.6a). Second, the net vorticity generation inside the spiral band tends to deflect the midlevel vortex toward the tilting (Fig. 4.6c), which moves it closer to a vertically stacked position with the low-level vortex.??unclear??

The negative portion of the tilting dipole occurs radially outside ??on the outward side??of the band, and its magnitude is actually larger than the positive tilting due to the enhancement by the downdraft occurring on the outside yes?? (Fig. 4.6b). As found by Rotunno and Klemp (1982), the tilting-generated midlevel vorticity on the flanks of the updraft dynamically promote updraft (downdraft) growth on the downshear-right (-left). This suggests that while updrafts are dynamically favored inside the band, the pool of low-θ_e air that develops east of the circulation center (Fig. 4.4k) is dynamically forced from the midlevels ??why not lower levels??where tilting promotes downward motio

Of course, the net effect of the tilting dipole is not significant in an area-averaged sense??small area??, but it appears that tilting is critical to understand the location of midlevel vorticity maximum at the periphery of the MCS (Fig. 4.4b-d), the tendency of the MCS to transition into a spiral shape, and the continued location of the vorticity maximum at the flank of the spiral band. These results emphasize the criticality of the local vertical shear associated with the pre-Chanchu vortex; without vertical shear the vortex tilting term is unimportant. In fact, such a tilting mechanism has not been presented until now. ??what about other cases? e.g., in Bonnie. you may check?? does it mean that for an axisymmetric vortex, there will be no spiral bands?

4.4. Initial surface deepening phase

As the spiral band develops in association with midlevel vortex enhancement, related processes are occurring that favor near-surface TCG. Thus we aim to understand how the spiral band facilitates the first ??6-h surface intensification after TCG ??(Fig. 4.2).

4.4.1. Development of near-surface cold pool

As convection intensifies by 5/01-193 along the convergence zone (Fig. 4.4g), the pool of near-surface low-θ_e air develops (Fig. 4.4k) northwest of the center and begins to advect cyclonically around the upshear portion of the low-level circulation. The low-θ_e pool develops as the mean vertical motion shifts to a negative trend??area averaged, may not be local features (Fig.

4.2), likely as a dynamically-forced downdraft from the spiral band convection. The critical element of this evolution in relation to TCG is that the rapid deepening of surface pressure begins coincident with the formation of the surface low-θ_e pool and continues as the area covered with low-θ_e air grows larger (Figs??. 4.4k,l). The low-θ_e air is thus not?? detrimental to genesis, as is often assumed. At 5/0330-195.5 MCS4

continues to evolve as a spiral band (Fig. 4.4h) as surface pressure continues its rapid fall (Fig. 4.4l), and a clear slot ??due to the cold cored vortex, as discussed in Part II??develops east of th similarities between the processes described above and those that occur in a rapidly deepening midlatitude cyclone (Sanders 1986) and a supercell entering the tornado phase (Lemon and Doswell 1979) cannot be ignored. However, we reserve detailed comparisons for Section 4.6.

4.4.2. Vertical structure of spiral band

In Fig. 4.7, we show the vertical structure of the spiral band in the vicinity of the circulation center (see Fig. 4.4h). The updrafts initiate along the convergence zone in the northeast quadrant of the circulation, beneath an area of midlevel divergence (HDIV??why? may be related to evaportive driven, also tilt cyclonically donward, please check, and show a map of thetae, vertical motion and flow vectors following Fig. 13 in K midlevels of a mature TC, but we emphasize that the processes ongoing are completely different than those within a mature TC??why??. As parcels near the surface approach the convergence zone (Fig. 4.7, 0º – 60º), they acquire cyclonic vorticity immediately upon ascent and take a slantwise vortical path due to the sheared flow in which they initiate. As the updrafts reach the 500-hPa level, they encounter strongly convergent horizontal flow ??why??(HCON, Fig. 4.4d), and thus ascend (descend) above (below) the 500-hPa level (Fig. 4.7, 180º). The most significant downdrafts occur in the southwest quadrant of the vortex, descend anticyclonically to the surface ??unclear(Fig. 4.6), and likely transport the relatively low-θ_e air to the surface (Fig. 4.4l). The slantwise ascent that occurs within the sheared spiral band is critical to the longevity of the spiral band since downdrafts do not fall through and contaminate the updraft, as is well-known for supercells (Weisman and Klemp 1986).

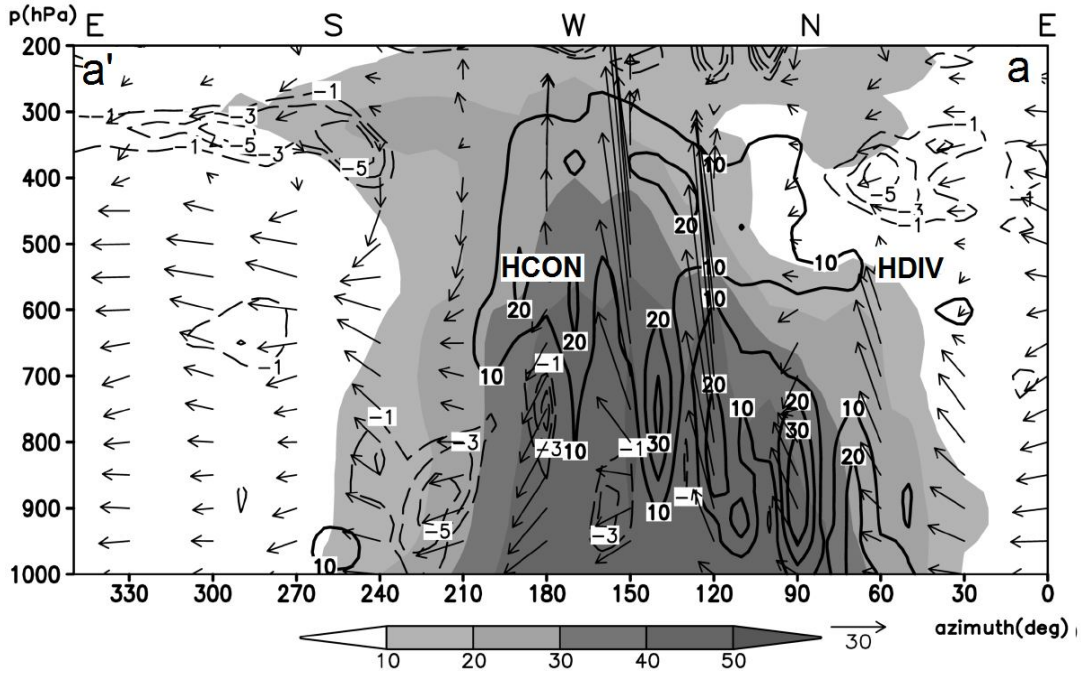

Figure 4.7. Height-azimuth cross section of radar reflectivity (dBZ, shaded) and relative vorticity (x 10^{-7} s^{-1}, contoured) at 0330 UTC 5 May, taken at a R = 30 km from the center of circulation, as shown in Figure 4.4h from a – a'. In-plane wind vectors (vertical motion enhanced by a factor of ten) are superposed. HCON and HDIV represent areas of midlevel horizontal convergence, as shown in Figure 4d. ??add a distance of 50 km, may take another crosssection at R =60

4.4.3. Low-level vorticity generation

In the low levels (Fig. 4.6d), the mean precipitation structure during TCG is similar to that in the midlevels, but with a more pronounced radar reflectivity "hook." The convergence zone and circulation center lie at the inner edge of the hook. The processes by which net cyclonic vorticity is generated along the convergence zone and input into the primary circulation center are obviously critical to TCG.

Here we argue that vortex tilting plays the critical role by locally generating net cyclonic low-level vorticity along the convergence zone. Fig. 4.6e shows that the local shear vector in the vicinity of the convergence zone is southerly such that the low-level horizontal vorticity is oriented parallel to the easterly inflow along the convergence zone. Thus, the parcels flowing along the convergence zone have a

streamwise component of horizontal vorticity. To visualize the importance of streamwise vorticity in the present case, imagine a parcel flowing along the convergence zone toward the circulation center (Fig. 4.6d). As soon as the parcel encounters an updraft, the vertical cyclonic vorticity immediately increases via tilting (Davies-Jones 1984; Rotunno and Klemp 1985), and thus becomes immediately available for stretching. Conversely, a streamwise parcel that encounters a downdraft exhibits an immediate decrease in vertical cyclonic vorticity as it is tilted downward. However, since the convergence zone is updraft-dominated (Fig. 4.6e), we should expect net upward tilting and thus net vorticity generation in this region.

Fig. 4.8a shows that all of the parcels approaching the convergence zone have a streamwise component of horizontal vorticity. Thus, when the parcels that enter the convergence zone are tilted upward, net cyclonic low-level vorticity is generated along the convergence zone. The updrafts that initiate along the convergence zone are subsequently stretched along their vortical ascent, while the near-surface vorticity is advected along the boundary. As the low-level parcels along the convergence zone acquire cyclonic vorticity more rapidly than those away from the convergence zone, they take a spiral cyclonic route to the center. Streamwise vorticity is favored in environments with veering wind profiles (Fig. 4.2) and is known to be the source of low level rotation in supercell thunderstorms (Davies-Jones 1984). Because the net positive tilting occurs radially inside of the spiral band (Fig. 4.6e), each discrete updraft within the convective band tends to spiral inward toward the source of

.

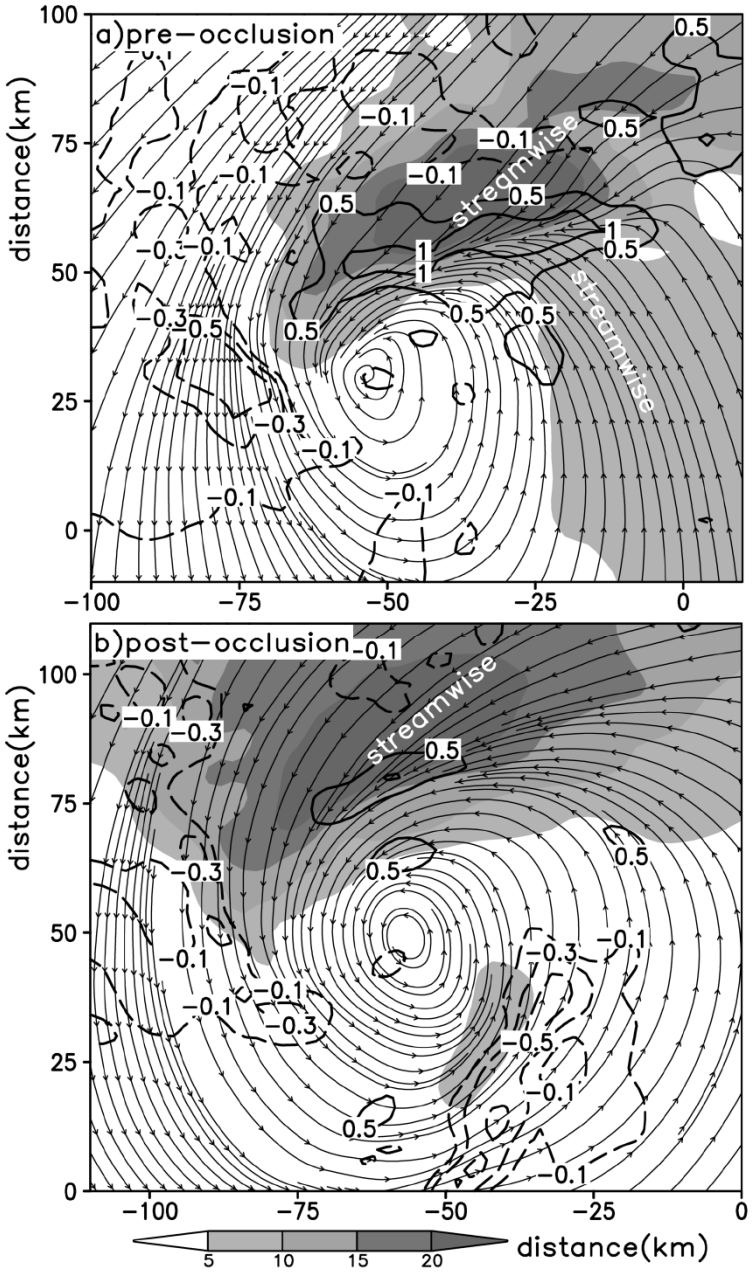

Figure 4.8. As in Fig. 4.6e, but for the mean streamwise vorticity (shaded) and vertical motion (contoured) in the sfc – 1.5 km layer during the (a) rapid intensification phase (i.e. pre-occlusion) and (b) maintenance phase (i.e. post-occlusion). Fields are time-averaged during (a) 0230 - 0430 and (b) 0730 – 0930 UTC 5 May.

Within and radially outward from the spiral band, downdrafts occur (Fig. 4.7e) and do not converge into the circulation center. It would be misleading to state that the downdrafts are *dispelled* from the circulation center; instead, there is simply

no mechanism by which they can acquire sufficient cyclonic vorticity ??unclear?to spiral inward at a similar rate to that occurring along the convergence zone. Thus the downdrafts remain radially outward of the inward-spiraling convective band. In this discussion of downdrafts, it is important to mention the importance of environmental preconditioning in facilitating TCG. The high environmental RH (Fig. 4.2) suppresses strong downdrafts, which could disrupt the processes ongoing along the convergence zone if they were strong enough to spread in all directions when they impacted the ground. In fact, Markowski and Richardson (2009) state that in environments with high low-level RH, the likelihood of supercell tornadoes increases due to the suppression of strong downdrafts.

4.4.4. A discrete updraft along the convergence zone

An individual updraft along the convergence zone is shown in Fig. 4.9a. It is the first of many similar convective features that comprise the convergence zone (near the time in Fig. 4.4f, just prior to TCG). A close inspection of this storm indicates that in scale and structure it resembles a supercell, which is not surprising since the environment in which it develops is conducive to such storm mode (Fig. 4.3b). The detailed structure of this storm is not the focus here, but of interest to TCG is that the near-surface vorticity in the "hook echo" reaches 0.01 s^{-1}, almost reaching the levels of a tornado??interesting, but neew double checking. Such intense low-level vorticity cannot by simply stretching of ambient cyclonic vorticity. Instead, Fig. 4.9b shows that as inflow approaches the primary updraft it is indeed first tilted and then stretched. The tilting in advance of the primary updraft provides additional vorticity for stretching.

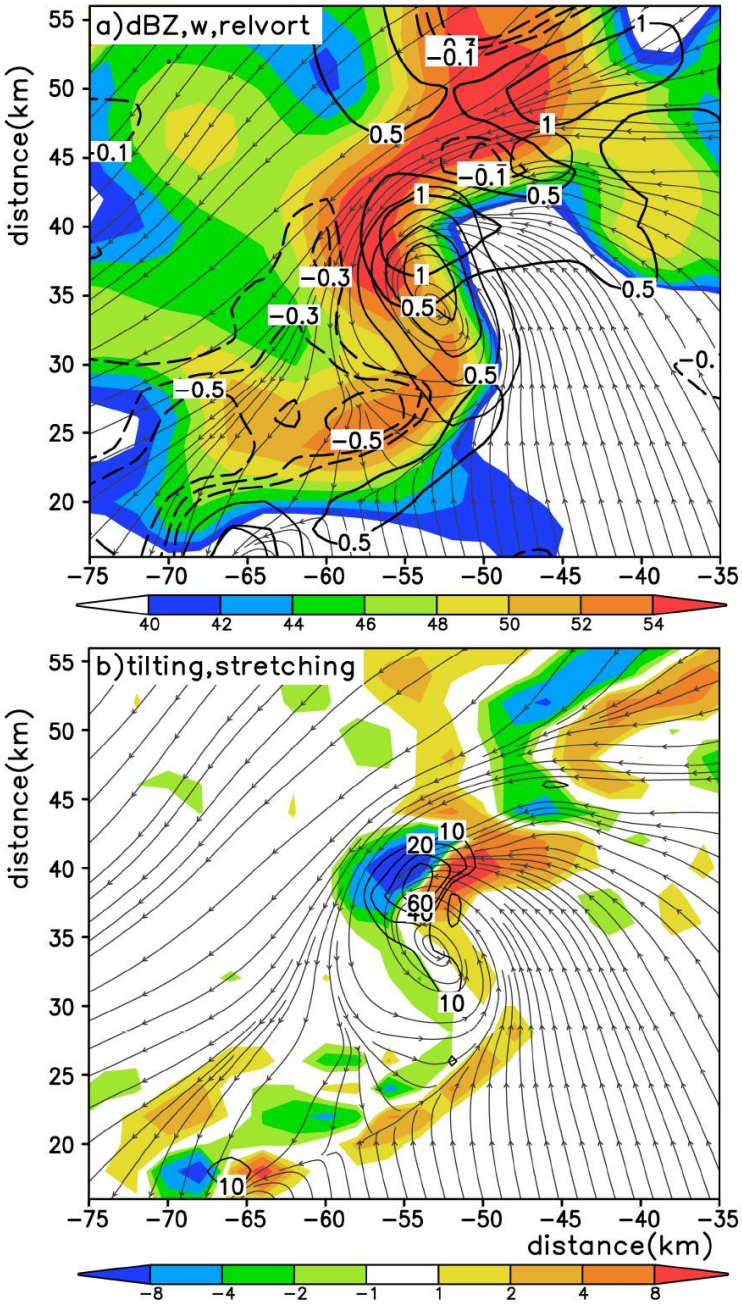

Figure 4.9. Horizontal distribution of near-surface (a) radar reflectivity (shaded, dBZ), vertical motion (heavy contours, ms^{-1}), and relative vorticity (light contours at 2, 4, 6, 8, and 10 x 10^{-3} s^{-1}); (b) tilting rates (shaded, x10^{-6} s^{-2}) and stretching rates (contours, x10^{-6}). Streamlines at 950 hPa are superposed.

In summary, streamwise vorticity is swept into updrafts along the convergence zone, initially tilted then rapidly stretched, leading to enhanced near-surface vorticity along the convergence zone. This process occurs in many

convective cells along the convergence zone of the spiral band, and only tilting of streamwise vorticity can explain the initial development of near-surface cyclonic vorticity *available for stretching*.

4.4.5. Vortex mergers

The supercell described above becomes part of the initial TC-scale vortex, but its scale is of course too small to initiate WISHE. Instead, the merger of several near-surface vortices, spawned in a similar manner, merge to form the primary circulation center. This process is shown explicitly in Fig. 4.10, where vortex 1 (Fig. 4.10a, "1") consumes two additional vortices (Fig. 4.10a, "2" and "3"). Vortices 2 and 3 develop along the convergence zone where streamwise vorticity is preferentially tilted (Fig. 4.8a) and intense convection is supported by midlevel divergence (Fig. 4.4d). Vortex 2 (3) develops about 40 km (70 km) northeast of the center and advects cyclonically inward toward vortex 1. Vortices 2 and 3 are both coupled with discrete updrafts, which constantly ingest streamwise vorticity, first tilting and subsequently stretching to produce the areas of locally-enhanced near-surface cyclonic vorticity. Vortex 3 exhibits in its center an area of minimum pressure, which deepens as it approaches vortex 1. ??cold they be considered as VHTs or be traced to VHTs??

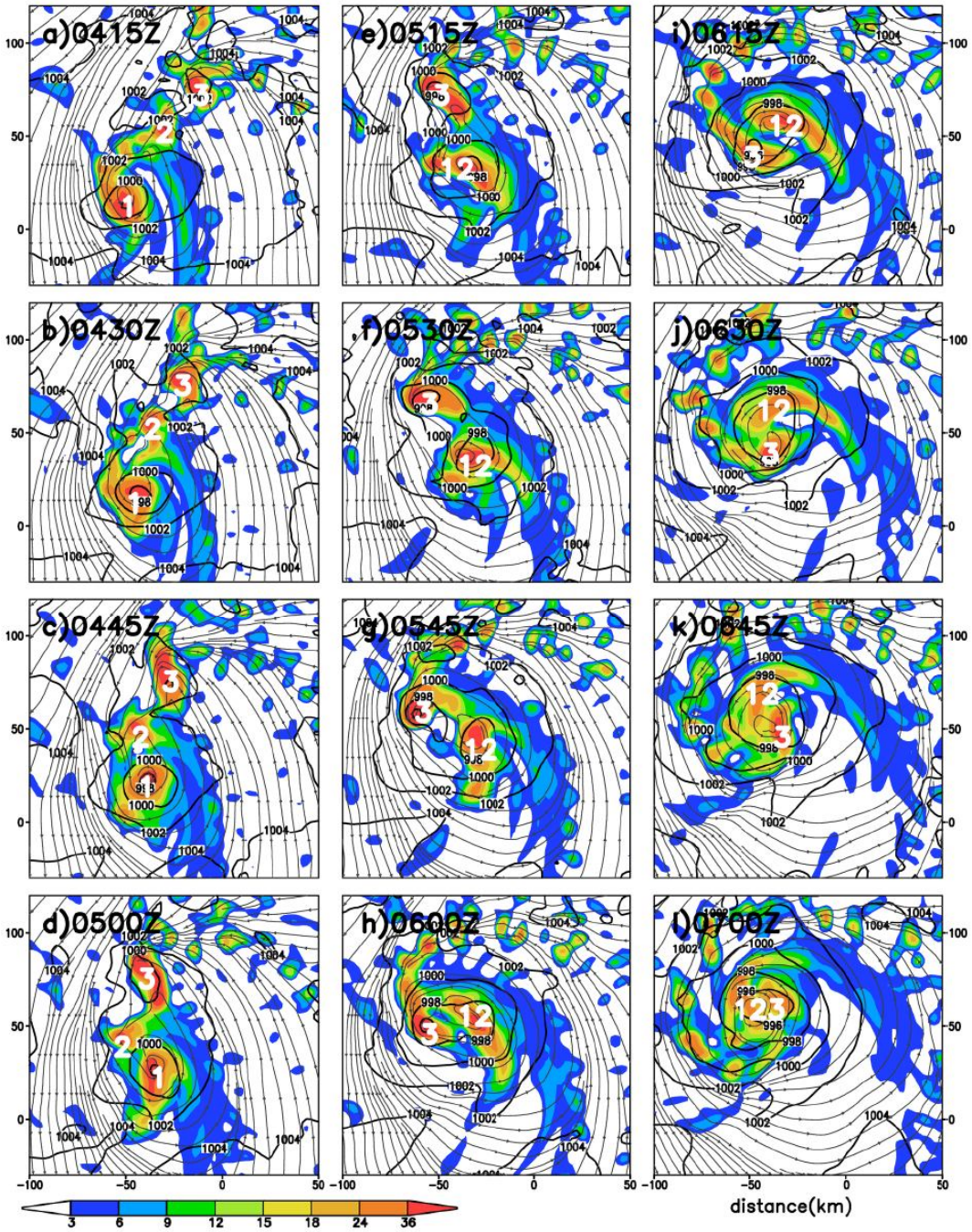

Figure 4.10. Horizontal distribution of 950-hPa relative vorticity (x 10^{-5} s^{-1}, shaded) at 15-min intervals from (a) 0415 UTC (top-left) – (l) 0700 UTC (bottom-right) 5 May. The surface pressure field (hPa, contours) and the horizontal streamlines are superposed. Symbols "1," "2," and "3" in (a) denote vortices of interest that merge into "123" by (l). ?? check to see if vorticity and Psea grow at the same pace. Use smaller domains to enlarge vortices. Also plot a map of conv/div for 3 vortices??

Vortex 2 merges with vortex 1 by 5/5.25-197.25 UTC (Fig. 4.10e), and by 5/06-198 (Fig. 4.10h) vortices 12 and 3 are within close proximity. The vortices

merge into a single, coherent vortex 123 by 5/07-199 (Fig. 4.10l), at which time no dominant vortices are active along the convergence zone. In fact, as the vortex mergers occur near the surface, the convergence zone rotates cyclonically around the center (Fig. 4.10). Vortex 123 exhibits a significantly lower pressure and larger physical size after the mergers (Fig. 4.10l). It is important to note that the mergers shown in Fig. 4.10 are not random mergers; instead they are related to the tendency of convection along the convergence zone to acquire net cyclonic vorticity. In this sense, *vortex mergers near the surface are simply a symptom of TCG ??unclear?? and not the cause of TCG*. As will be discussed in the next section, significant changes to the surface vortex occur after 5/06-198, when intensification ceases temporarily (Fig. 4.2).

The processes associated with the low-level vortex amplification during the rapid deepening phase are summarized in Fig. 4.11a-c. As low-level convergence increases along the spiral band, enhanced vertical motion occurs (Fig. 4.11a). Because the low-level inflow is rich in streamwise horizontal vorticity, the updrafts immediately acquire cyclonic vorticity through near-surface tilting (Fig. 4.11b) and subsequently advect along the convergence zone toward the circulation center (Fig. 4.11c).

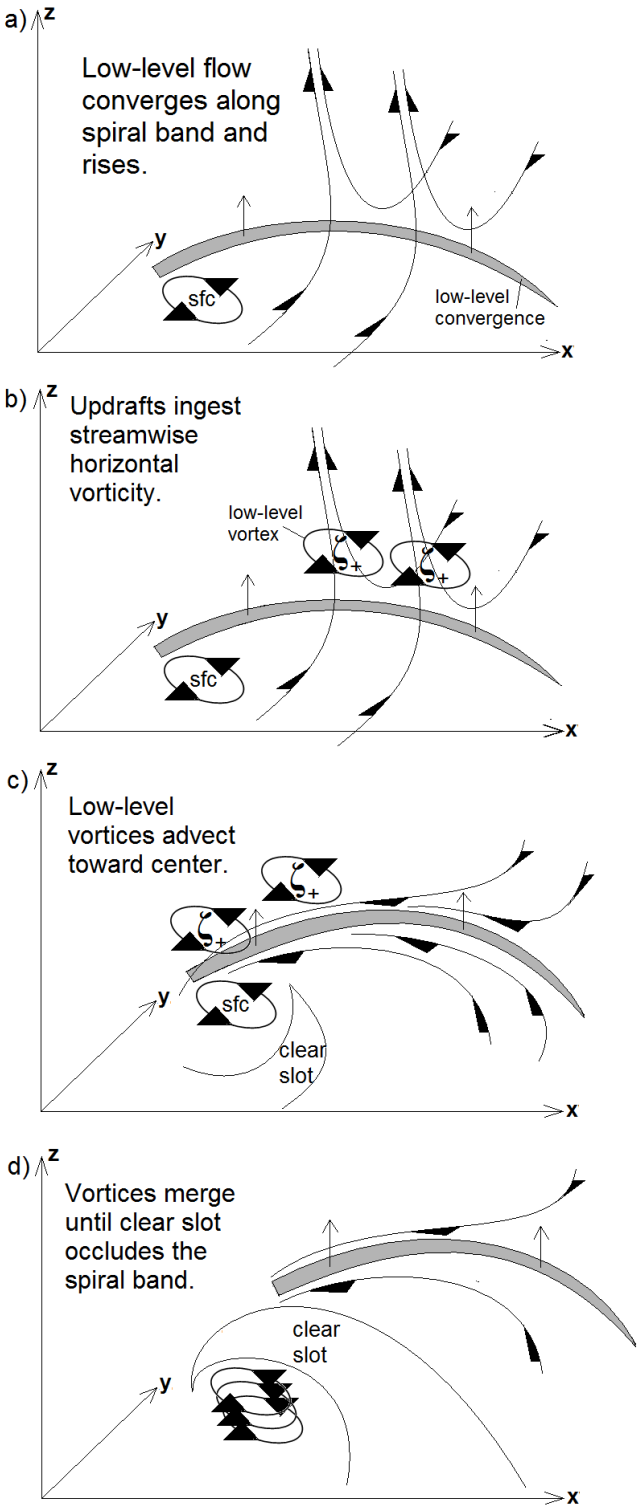

Figure 4.11. Conceptual model of the low-level rapid intensification phase.

4.5. Intensity maintenance phase

The processes responsible for the development of near-surface vorticity, and thus the deepening of the central pressure, occur in association with the life cycle of MCS4. At first a disorganized cluster of convection, MCS4 intensifies along a convergence zone and is composed of many cyclonically-rotating convective cells. In this section, we show how the continued evolution of the rainband temporarily causes TCG to stall.

4.5.1. Thermodynamic characteristics of the clear slot

As the vortex intensifies by the mergers of low-level vortices, the clear slot wraps cyclonically around the circulation center and covers an increasing spatial area to the east of the circulation center by 5/06-198 (Fig. 4.12a). The low-θ_e clear slot covers much of the southern semicircle of the low-level circulation (Fig. 4.12b), but only a small portion of the clear slot contains hydrometeors. The critical aspect of the clear slot is that although it comprised entirely of low-θ_e air near the surface, the thermodynamic characteristics within it differ greatly (c.f. Fig. 4.12b,d). In the vicinity of precipitation, the air is relatively cool and moist due to the evaporative effects of rainfall??must be related to the vortex circulation??. However, at the easternmost periphery of descending motion occurs in the clear air (c.f. Fig. 4.12a,c) and is dry and relatively warm (Fig. 4.12d).

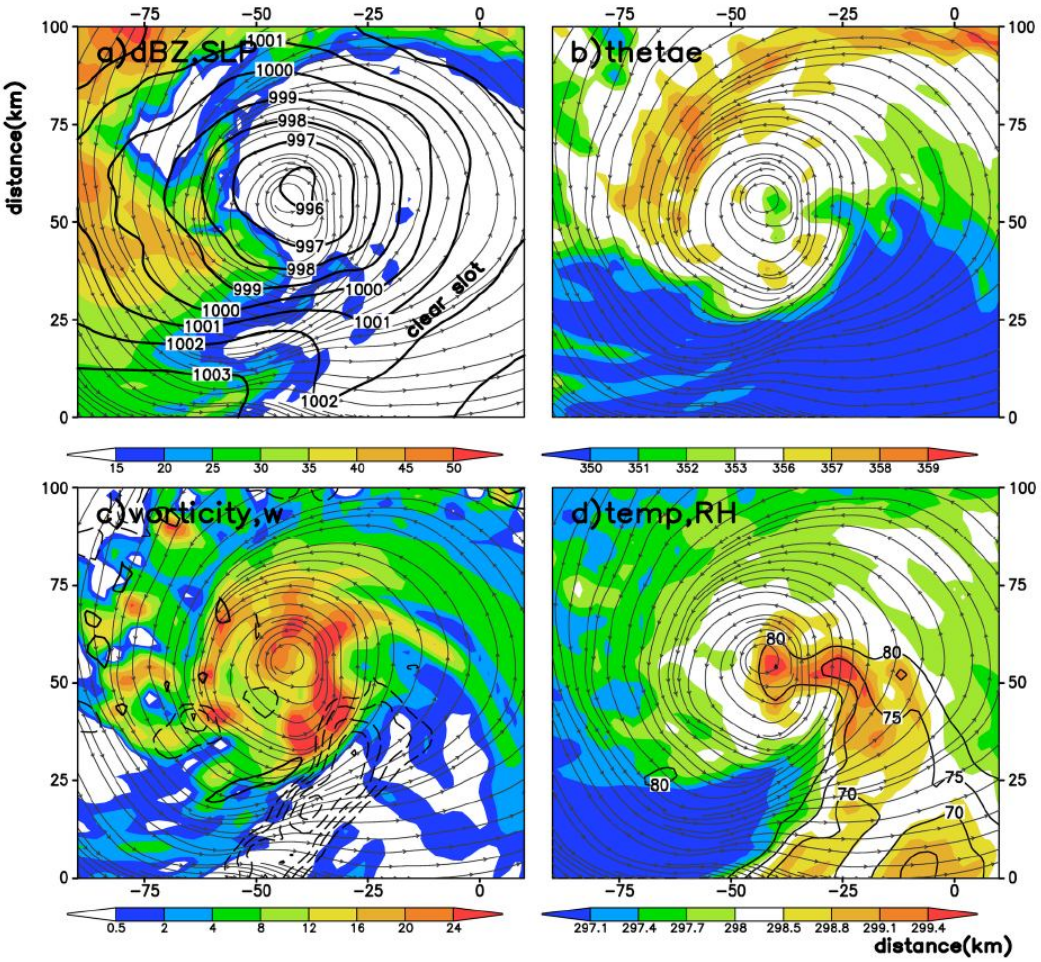

Figure 4.12. Horizontal distribution of (a) radar reflectivity (dBZ, shaded) and sea level pressure (contoured every 1 hPa), (b) θ_e (shaded), (c) relative vorticity (x 10^{-5} s^{-1}, shaded??include -ve) and vertical motion (contoured at -1, -0.8, -0.6, -0.4 -0.2, 1, and 2 m s^{-1}what about 0.5 intervals??); (d) temperature (shaded, K) and relatsive humidity (contoured at intervals of 5% below 80%), at 0600 UTC 5 May during the occlusion. ??you have shown similar results before, e.g., Fig. 4.4??

The dry adiabatic descent likely has its origin in the upstream midtroposphere, where downward motion is dynamically favored on the outside of the spiral band (Fig. 4.6b). Its location to the east of the "hook echo" begs for comparison with the rear flank downdraft (RFD) during tornado formation. Lemon and Doswell (1979) show that tornadogenesis often occurs as the primary updraft of the supercell collapses and downdrafts occur on the upshear side. The downdrafts that wrap cyclonically around the supercell updraft contain some combination of hydrometeors

and forced dry descent, as is evident in this case in Fig. 4.12d. The dry descent during tornado formation allows the tornado to be viewed easily without obstruction from precipitation (see Lemon and Doswell 1979, their Fig. 4). Recent observations indicate that in some cases of strong tornadoes, the RFD is indeed warm (Markowski et al. 2002). When the warm descending air reaches the ground, it spreads in all directions??not right??, some inward toward the center. Further, in a study of TCG, Stossmeister and Barnes (1992) observe what appears to be a very similar process in an intensifying TC. They show not only the comma-shaped cloud field with adjacent clear slot (their Fig. 2), but also an area of low-θ_e air within the clear slot that is warm and dry near the surface. They may have actually observed a similar phenomenon to that described herein, associated with the initial stage of TCG, which in many ways resembles the formation of a larger-scale tornado.

4.5.2. Occlusion

Immediately after completion of the mergers by 5/06-198, the low-θ_e clear slot completely surrounds the circulation center (Fig. 4.13i,j) and effectively cuts off the inflow to the circulation center (Fig. 4.13e,f), which then becomes displaced from the main updrafts within the spiral band (Fig. 4.11c,d). While some convection persists near the circulation center (Fig. 4.13f), the most intense convection along the convergence zone is no longer connected to the circulation center (Fig. 4.8b), which can no longer intensify via mergers, as shown in Fig. 4.10. This process can be considered as an occlusion, similar to that which occurs in a tornado (Alderman et al. 1999; Marquis et al. 2008), and herein marks the end of the first phase of genesis.

After the occlusion, the minimum surface pressure actually slightly increases (Fig. 4.2) during the ensuing 6-h maintenance period, i.e. 5/06-198 – 5/12-204.

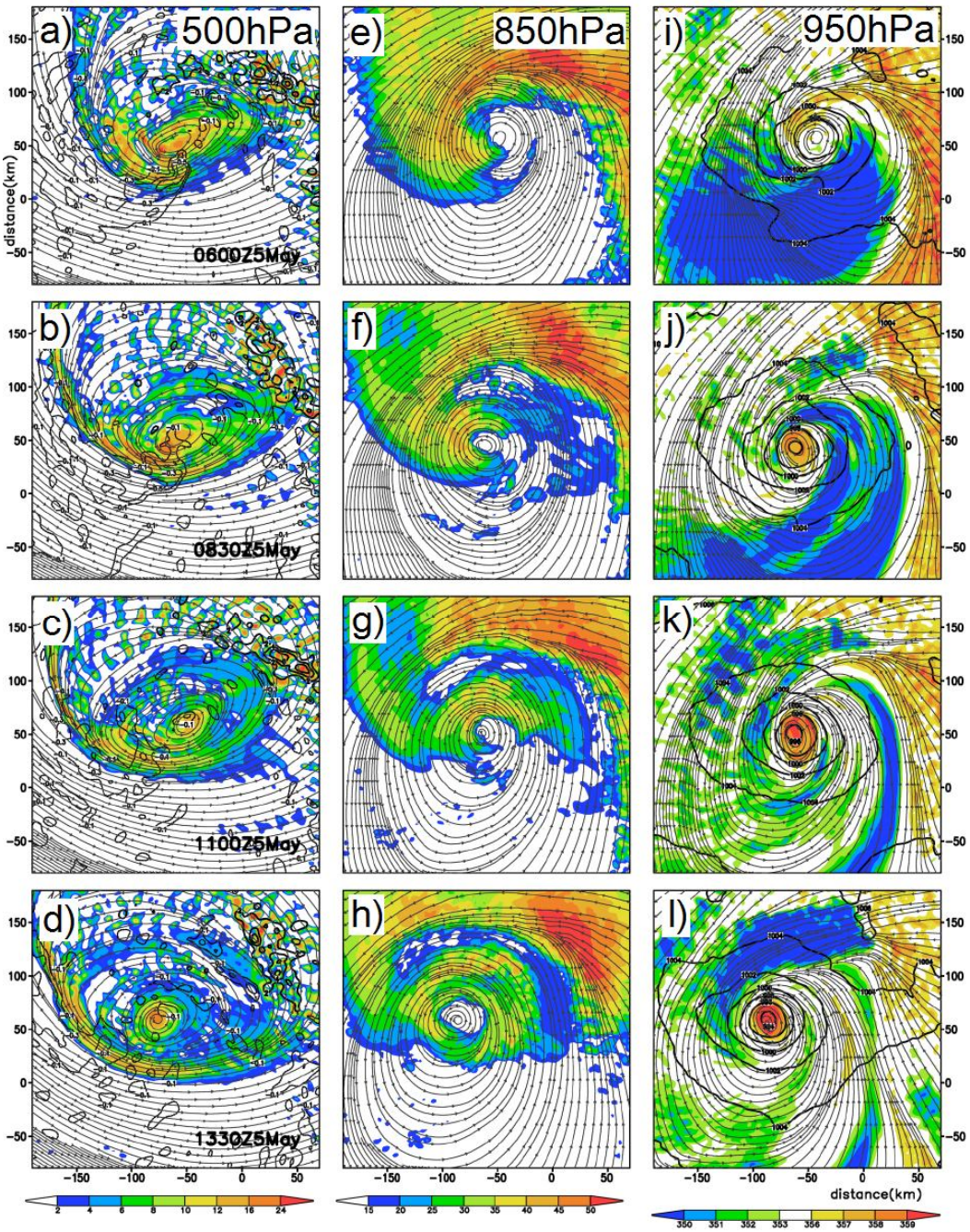

Figure 4.13. As in Fig. 4.4, but for 0600 – 1330 UTC 5 May, i.e. the maintenance phase.

?? this similar to Fig. 4.4. Yes at a different time.

An important feature of the occlusion is that it represents the final transition to an upright vortex at the center (cf. Fig. 4.13a,e). Because the circulation centers

are vertically coherent during this maintenance period, the vertical shear in the core region is very small (not shown), while the shear in the outer regions, e.g. in the vicinity of the detached spiral band, remains large. Thus the large magnitude of the 900 – 400 hPa vertical shear (Fig. 4.1) during this period is associated with peripheral differences in the circulations at 900 and 400 hPa. In this way, the conventional use of area-averaged vertical shear appears to be less applicable to the determination of likelihood of intensification during this portion of Chanchu's life cycle. Although pressure deepening ceases during this period, the detached spiral band (Fig. 4.8b) continues to ingest streamwise vorticity and likely contributes to continued storm-scale intensification (i.e., area-averaged vorticity, Fig. 4.2), but not central pressure deepening.

If the pre-Chanchu disturbance existed over land, it surely would be nearing the end of its life due to the impact of the occlusion. And, as discussed above, post-occlusion Chanchu does temporarily cease intensification. Unfortunately for those affected by Typhoon Chanchu, when the primary band of convection detaches from the circulation center, intensification only temporarily stalls. Because the near-core wind speed increases by nearly 50% (Chapter 2, Fig. 2.8) during the initial 6-h deepening period, the air-sea interaction can quickly modify the low-level low-θ_e air, which warms through fluxes of both sensible and latent heat. This is particularly true for the warm, dry air (RH < 80%) that descends into the center of the storm during the occlusion. Thus the 950-hPa θ_e increases between 5/0830-200.5 – 5/11-203 (Fig. 4.13i-l). During this 'recovery period' between 5/06-198 – 5/11-203, the θ_e increases

significantly in the nascent eye (Fig. 4.13j-l), and the storm-scale RH increases again (Fig. 4.2) after the decrease associated with the drying downdrafts.

The occluded circulation thus does not dissipate, and after the 6-h period of post-occlusion intensity maintenance (Fig. 4.2), Chanchu's intensification simply continues (not shown) in the manner more typically understood for TCs: a warm-core, vertically upright vertical structure, and a quasi-axisymmetric eyewall. The nascent eyewall can be seen in Fig. 4.13f-h.

4.6 Discussion and conclusions

In the case of Chanchu, TCG apparently occurs due to the interaction of convection with vertical shear, the latter of which is often ignored for TC studies.?? do you mean the shear is good for TCG?

Thus it is worthwhile to note some similarities with the evolution of supercells and midlatitude cyclones, both of which are rotating storms that can develop an intense near-surface circulation in sheared environments. The horizontal scale of Chanchu is of course somewhere between the midlatitude cyclone and supercell thunderstorm, but the midlevel-surface interaction that comprises TCG appears qualitatively similar to the canonical depiction of explosive midlatitude cyclogenesis and supercell tornadogenesis. The three highly-sheared storm systems all exhibit rapid surface cyclogenesis??different processes??, midlevel intensification prior to that at the surface, intensifying r surface convergence zones, a clear slot during the rapid surface intensification, and an occlusion. And all three take on the comma shape.

In the midlatitudes, a large-amplitude 500-hPa vorticity maximum typically exists for several days prior to surface cyclogenesis (Sanders 1986), and similarly in cases of supercell tornadogenesis the midlevel mesocyclone precedes that in the low

levels and develops due to tilting of environmental vorticity associated with environmental vertical shear. As discussed above, a similar tilting mechanism occurs leading to the intensification of the midlevel vortex in this case.

Another feature common to midlatitude cyclones and supercells is the clear slot, which is associated with rapid near-surface cyclogenesis (Browning 1997) in the midlatitudes and remains a research focus in understanding tornadogenesis. The dry slot in supercell storms acts to focus inflow into a primary updraft which can subsequently tilt and stretch ambient streamwise vorticity to extreme levels. In fact, in this case the minimum surface pressure drops most rapidly as a clear slot forms (Fig. 4.4h), and the location of the minimum pressure occurs at the southeastern tip of the reflectivity signature (Fig. 4.7d), often the location of tornado formation in supercells.

The midlatitude cyclones and tornadoes both occlude as the dry slot encircles and isolates the circulation center from the convection to its northeast and suffocates its supply of moisture. The occlusion typically signals the end of intensification, which stalls without sufficient input of moisture. A similar occlusion occurs in the present case, but aside from the obvious difference in scale, a critical distinction in the analogy of TCG to the other storms is that the *occlusion in the present case does not mark the end of the incipient TC, but rather isolates the circulation such that it can intensify via WISHE*.

This chapter represents a significant departure from the ongoing discourse regarding TCG. Rather than a stochastic process, the TCG process in the case of Chanchu proceeds in an well-organized manner beginning with favorable large scale

conditions. As an MCS intensifies in a sufficiently humid environment in which winds veer with height (Fig. 4.2), midlevel cyclonic vorticity enhancement is strongly favored (Fig. 4.5). The resulting midlevel circulation deforms the MCS into a spiral rainband, along which low-level cyclonic vorticity is preferentially generated from the tilting and subsequent stretching of streamwise vorticity and advected toward the circulation center (Fig. 4.8, 4.9). Through mergers, the surface circulation increases markedly (Fig. 4.10) before the rainband occludes and intensification ceases temporarily.

In this way, we hypothesize that the processes associated with the initial deepening phase (Fig. 4.2, 5/00-192 – 5/06-198), specifically the processes associated with the evolution of MCS4, may represent a *unique mesoscale phenomenon, something like a tropical megacell (TMC).* The life cycle of the TMC in the present case spans a 14-h period from initiation to occlusion (4/16-184 – 5/06-198) and is characterized by a spiraling radar reflectivity structure composed of many discrete updrafts which each acquire cyclonic vorticity from the veering environmental wind. The timescale is significantly shorter (longer) than its midlatitude (supercell) counterpart. Prerequisite to the development of such a TMC in the present case are: a veering wind profile up to 400 hPa, low- and midlevel moistening (Chapter 3), some sort of triggering mechanism (in this case a cold pool left by a previous MCS), and all of the typical TCG preconditions. Barotropic intensification follows after the occlusion phase of the TMC. The 14-hr TMC itself appears responsible for the production of near-surface vorticity, which has until now remained a mysterious process for TCG. Whether such a TMC mechanism occurs in reality and serves as

the trigger for actual TCG must be tested. The present dissertation is merely a single case study.

In summary, we have investigated the processes associated with the TCG of Typhoon Chanchu, as simulated with the WRF at finest resolution of 2 km. Apparently, TCG occurs in three phases. The first phase of initial deepening lasts just 6 h and occurs in a highly vertically sheared (900 – 500 hPa) environment, in which the tilted vortex transitions to vertically upright, facilitated by a spiral convective band. The second phase is one of intensity maintenance that begins as the spiral band occludes and the occluded circulation transitions to a warm core. The second phase of genesis begins with a 6-h period of near-constant intensity. During the maintenance phase, the near-core vertical wind shear diminishes significantly. This period is characterized by the development of a near-surface warm core inside a nascent eye, which is surrounded by low-θ_e air from the dry slot. After the low-θ_e air recovers through oceanic heat fluxes, the third phase of intensification occurs as convection intensifies around the warm core and Chanchu continues its intensification in the manner well-understood as a quasi-axisymmetric barotropic cyclone.

Chapter 5: Summary

5.1. Concluding remarks

Several new insights into TCG have been brought to light in this dissertation. The first major result was that the synoptic scale precursor disturbance that eventually spawns Typhoon Chanchu exhibited initially a dramatic westward vertical tilt, which transitioned over a week-long period to a vertically upright structure at the onset of TCG. The tilt arose due to the westward-tilted structure of a westerly wind burst, which was associated with the active phase of the MJO and modulated the formation of the pre-Chanchu vortex. The implication of the vertical tilt was that forced ascent occurred to the downtilt-right of the vortex axis and thus favored ascent and precipitation there. The role of precipitation was its vorticity generation, which served to attract the tilted vortex and align it in the vertical.

The downtilt-right precipitation was shown to take the form of squall lines and convective clusters, which persisted during the several days leading to TCG. Each of the strongest mesoscale convective systems (MCSs) left at the surface a cold pool, which served as the focus for subsequent MCS development. One MCS spawned a midlevel convective vortex (MCV), which merged with and intensified the preexisting tilted vortex. In whole, the series of MCSs preconditioned (i.e., humidified) the near-vortex environment such that the final MCS exhibited no cold pool and was dominated by slantwise updrafts. The final MCS became the first spiral rainband of the incipient TC and persisted during the initial rapid surface pressure deepening period, which was characterized as a transition from a cold-core vortex to a warm-core vortex.

A second major result arose because the final MCS developed in a highly vertically sheared environment associated with the tilted vortex. The updrafts within the final MCS tilted environmental shear-generated horizontal vorticity, selectively enhancing vorticity on the flanks of the updrafts and ultimately leading to the deformation into a spiral shape. More specifically, because the environmental wind veered with height, it was concluded that net cyclonic vorticity generation was favored on the cyclonic flank of the updrafts. Updrafts that initiated within the MCS thus preferentially acquired cyclonic vorticity at the surface through tilting of horizontal vorticity, and were subsequently stretched in deep vortical updrafts. In short, the initiation of an MCS in an environment with veering winds dictates that each updraft will acquire net cyclonic vorticity at low altitudes, possibly facilitating the often-observed rapid TCG. Until now, the implications of a veering wind profile in the TCG environment has not been mentioned in the literature, likely due to the long-held view that vertical shear-related processes are unfavorable for TCG.

5.2. Future research agenda

Research will continue on several fronts. First, the existence of vertically tilted precursors has not been clearly established in the literature, but the precipitation structure and evolution associated with the vertical alignment of the tilted precursor herein resembles the canonical depiction of TCG, e.g., the development of a spiral band during initial surface pressure deepening. Thus, future research will aim to understand whether other precursor disturbances do in fact exhibit vertical tilt more often than previously thought, particularly away from dynamic MJO environments.

Moreover, the model exploited herein (the WRF) has demonstrated its ability to successfully reproduce TCG given the existence of a tilted precursor. This suggests that with sufficient representation of the sub-synoptic environment, particularly the vertical structure of the tilted vortex, skillful deterministic predictions of TCG may indeed be possible in these cases. A goal is to work with operationally-acquired datasets to understand whether present observation methodologies are sufficiently sampling the pre-TC environment. If precursors do tilt in the vertical, and the downtilt-right environment does exhibit a veering wind profile, successful numerical TCG forecasts may depend on adequate representation of the vertical structure of the horizontal wind far from the near-surface circulation center, which is often the focus of observational campaigns.

Next, at the convective scale, where convective "hot towers" have long been known to exist in the near-TC environment and play some role in TCs, the supercell structure presented herein has been neither observed nor considered in the deep tropical environment. Of future interest is the detailed structure of this convective cell and the prevalence of its peers in nature. If the typical spiral band in nature is indeed composed of supercellular convection, or at least some tropical variant of the supercell, the mechanisms for TCG could be quite different than that presently understood.

Bibliography

Aiyyer, A. R., and J. Molinari, 2003: Evolution of mixed Rossby–gravity waves in idealized MJO environments. *J. Atmos. Sci.,* **60,** 2837–2855.

Barnes, S. L., 1970: Some aspects of a severe, right-moving thunderstorm deduced from mesonetwork rawinsonde observations. *J. Atmos. Sci.,* **27,** 634–648.

Barrett, B. S., and L. M. Leslie, 2009: Links between tropical cyclone activity and Madden–Julian oscillation phase in the North Atlantic and Northeast Pacific basins. *Mon. Wea. Rev*., **137**, 727 – 744.

Bartels, D. L., and R. A. Maddox, 1991: Midlevel cyclonic vortices generated by mesoscale convective systems. *Mon. Wea. Rev.*, **119**, 104–118.

Biggerstaff, M. I., and R. A. Houze, Jr., 1991: Kinematic and precipitation structure of the 10 – 11 June 1985 squall line. *Mon. Wea. Rev*., **119**, 3034 – 3065.

Bister, M., and K. A. Emanuel, 1997: The genesis of Hurricane Guillermo: TEXMEX analyses and a modeling study, *Mon. Wea. Rev*., **125**, 2662–2682.

Black, M. L., J. F. Gamache, F. D. Marks, C. E. Samsury, and H. E. Willoughby, 2002: Eastern Pacific Hurricanes Jimena of 1991 and Olivia of 1994: The effect of vertical shear on structure and intensity. *Mon. Wea. Rev.,* **130,** 2291–2312.

Bracken, W. E., and L. F. Bosart, 2000: The role of synoptic-scale flow during tropical cyclogenesis over the North Atlantic Ocean., *Mon. Wea. Rev*., **128,** 353–376.

Braun, S. A., M. T. Montgomery, K. J. Mallen, and P. D. Reasor, 2010: Simulation and interpretation of the genesis of Tropical Storm Gert (2005) as part of the NASA Tropical Cloud Systems and Processes Experiment, *J. Atmos. Sci*., (pre-release).

Browning, K. A., 1964: Airflow and precipitation trajectories within severe local storms which travel to the right of the winds. *J. Atmos. Sci.,* **21,** 634–639.

Camargo, S. J., M.C. Wheeler, and A.H. Sobel, 2009. Diagnosis of the MJO modulation of tropical cyclogenesis using an empirical index, *J. Atmos. Sci.*, **66**, 3061-3074.

Chang, H.-R., and P. J. Webster, 1990: Energy accumulation and emanation at low latitudes. Part II: Nonlinear response to strong episodic equatorial forcing. *J. Atmos. Sci.,* **47,** 2624–2644.

Davies-Jones, R.P.,1984. Streamwise vorticity: the origin of updraft rotation in supercell storms. *J. Atmos. Sci*. **41**, 2991–3006.

Davis, C. A., and L. F. Bosart, 2001: Numerical simulations of the genesis of Hurricane Diana (1984). Part I: Control simulation. *Mon. Wea. Rev.*, **129**, 1859-1881.

——, and ——, 2003: Baroclinically induced tropical cyclogenesis. *Mon. Wea. Rev.*, **131,** 2730–2747.

——, and ——, 2004: The TT problem: Forecasting the tropical transition of cyclones. *Bull Amer. Meteor. Soc*., **85,** 1657–1662.

Dickinson, M., and J. Molinari, 2002: Mixed Rossby–gravity waves and western Pacific tropical cyclogenesis. Part I: Synoptic evolution. *J. Atmos. Sci.,* **59,** 2183–2196.

Emanuel, K. A., 1986: An air–sea interaction theory for tropical cyclones. Part I: Steady-state maintenance. *J. Atmos. Sci.,* **43,** 585–604.

Emanuel, K. A., 1987: An air–sea interaction model of intraseasonal oscillations in the tropics. *J. Atmos. Sci.*, **44**, 2324–2340.

Frank, W. M., and P. E. Roundy, 2006: The role of tropical waves in tropical cyclogenesis. *Mon. Wea. Rev.,* **134,** 2397–2417.

——, and E. A. Ritchie, 1999: Effects of environmental flow upon tropical cyclone structure. *Mon. Wea. Rev.,* **127**, 2044–2061.

Fritsch, J. M., J. D. Murphy, and J. S. Kain, 1994: Warm core vortex amplification over land. *J. Atmos. Sci.,* **51,** 1780–1807.

Gamache, J. F., and R. A. Houze Jr. (1982), Mesoscale air motions associated with a tropical squall line, *Mon. Wea. Rev*., **110**, 118–135.

Gray, W. M., 1998: The formation of tropical cyclones. *Meteor. Atmos. Phys.,* **67,** 37–69.

Hack, J.J., and W.H. Schubert, 1986: Nonlinear response of atmospheric vortices to heating by organized cumulus convection. *J. Atmos. Sci.*, **43**, 1559-1573.

Harr, P. A., and R. L. Elsberry, 1996: Structure of a mesoscale convective system embedded in Typhoon Robyn during TCM-93. *Mon. Wea. Rev.,* **124,** 634–652.

——, M. S. Kalafsky, and R. L. Elsberry, 1996: Environmental conditions prior to formation of a midget tropical cyclone during TCM-93. *Mon. Wea. Rev.,* **124,** 1693–1710.

Hendricks, E. A., M. T. Montgomery, and C. A. Davis, 2004: The role of ‘‘vortical’’ hot towers in the formation of Tropical Cyclone Diana (1984). *J. Atmos. Sci*., **61**, 1209–1232.

Holland, G. J., 1995: Scale interaction in the western Pacific monsoon. *Meteor. Atmos. Phys.,* **56,** 57–79.

Hong, S.-Y., Y. Noh, and J. Dudhia, 2006: A new vertical diffusion package with an explicit treatment of entrainment processes. *Mon. Wea. Rev.*, **134**, 2318-2341.

Houze, R. A., Jr., S. A. Rutledge, M. I. Biggerstaff, and B. F. Smull, 1989: Interpretation of Doppler weather-radar displays of midlatitude mesoscale convective systems. *Bull. Amer. Meteor. Soc.,* **70**, 608 – 619.

——, 2004: Mesoscale convective systems, *Rev. Geophys.*, **42**, RG4003, doi:10.1029/2004RG000150.

——, W.-C. Lee, and M. M. Bell, 2009: Convective contribution to the genesis of Hurricane Ophelia (2005). *Mon. Wea. Rev*., **137**, 2778 – 2800.

Hulme, A. L., and J. E. Martin, 2009: Synoptic- and frontal-scale influences on tropical transition events in the Atlantic basin. Part I: A six-case survey. *Mon. Wea. Rev*., **137**, 3605 – 3625.

Jones, S. C., 1995: The evolution of vortices in vertical shear. I: Initially barotropic vortices. *Quart. J. Roy. Meteor. Soc.,* **121,** 821–851.

Kain, J. S., and J. M. Fritsch, 1993: Convective parameterization for mesoscale models: The Kain–Fritsch scheme. *The Representation of Cumulus Convection in Numerical Models, Meteor. Monogr.,* No. 46, Amer. Meteor. Soc., 165–170.

Kieu, C. Q., and D. L. Zhang, 2008: Genesis of Tropical Storm Eugene (2005) Associated with the ITCZ Breakdowns. Part I: Observational and Modeling Analyses. *J. Atmos. Sci.*, **65**, 3419-3433.

——, and ——, 2009: Genesis of Tropical Storm Eugene (2005) from merging vortices ssociated with the ITCZ Breakdowns. Part II: Roles of vortex merger and ambient potential vorticity. *J. Atmos. Sci.*, **66**, 1980-1966.

Kim, J.-H., C.-H. Ho, H.-S. Kim, C.-H. Sui, S. K. Park, 2008: Systematic variation of summertime tropical cyclone activity in the Western North Pacific in relation to the Madden-Julian oscillation. *J. Climate*, **21**, 1171 – 1191.

Klemp, J. B., and R. Rotunno, 1983: A study of the tornadic region within a supercell thunderstorm. *J. Atmos. Sci.,* **40,** 359–377.

Klemp, J. B., and R. B. Wilhelmson, 1978: The simulation of threedimensional convective storm dynamics. *J. Atmos. Sci.,* **35,** 1070–1096.

Lander, M. A., 1990: Evolution of the cloud pattern during the formation of tropical cyclone twins symmetrical with respect to the equator. *Mon. Wea. Rev.*, **118**, 1194–1202.

Lemon, L. R., and C. A. Doswell, 1979: Severe thunderstorm evolution and mesocyclone structure as related to tornadogenesis. *Mon. Wea. Rev.,* **107,** 1184–1197.

Liebmann, B., H. H. Hendon, and J. D. Glick, 1994: The relationship between tropical cyclones of the western Pacific and Indian Oceans and the Madden–Julian oscillation. *J. Meteor. Soc. Japan,* **72,** 401–411.

Lin, Y.-L., R. D. Farley, and H. D. Orville, 1983: Bulk parameterization of the snow field in a cloud model. *J. Appl. Meteor.,* **22,** 1065–1092.

Madden, R. A., and P. R. Julian, 1994: Observations of the 40–50 day tropical oscillation — A review. *Mon. Wea. Rev.,* **122,** 814–837.

Maddox, R. A., 1976: An evaluation of tornado proximity wind and stability data. *Mon. Wea. Rev.,* **104B,** 133 – 142.

Maloney, E. D., and D. L. Hartmann, 2001: The Madden–Julian oscillation, Barotropic dynamics, and North Pacific tropical cyclone formation. Part I: Observations. *J. Atmos. Sci.,* **58,** 2545–2558.

Mao, J., and G. Wu (2008), Influences of Typhoon Chanchu on the 2006 South China Sea summer monsoon onset, *Geophys. Res. Lett.*, **35**, L12809, doi:10.1029/2008GL033810.

Markowski, P.M., Straka, J.M., Rasmussen, E.N., 2002. Direct surface thermodynamic observations within the rear-flank downdrafts of nontornadic and tornadic supercells. *Mon. Wea. Rev.* **130**, 1692–1721.

Markowski, P.M., Straka, J.M., Rasmussen, E.N., 2003. Tornadogenesis resulting from the transport of circulation by a downdraft. *J. Atmos. Sci.* **60**, 795–823.

Markowski, P. M., and Y. P. Richardson, 2009: Tornadogenesis: Our current understanding, forecasting considerations, and questions to guide future research. *Atmospheric Research*, **93**, 3–10.

Marquis, J., Y. Richardson, J. Wurman, P. M. Markowski, 2008: Single- and dual-Doppler analysis of a tornadic vortex and surrounding storm-scale flow in the Crowell, Texas, supercell of 30 April 2000. *Mon. Wea. Rev.*, **136**, 5017-5043.

Menard, R. D., and J. M. Fritsch, 1989: A mesoscale convective complex-generated inertially stable warm core vortex, *Mon.Wea. Rev.*, **117**, 1237–1261.

Mlawer, E. J., S. J. Taubman, P. D. Brown, M. J. Iacono, and S. A. Clough, 1997: Radiative transfer for inhomogeneous atmospheres: RRTM, a validated correlated-*k* model for the longwave. *J. Geophys. Res.,* **102,** 16 663–16 682.

Molinari, J., K. Lombardo, and D. Vollaro, 2007: Tropical cyclogenesis within an equatorial Rossby wave packet. *J. Atmos. Sci.*, **64**, 1301 – 1317.

Montgomery, M. T., M. E. Nicholls, T. A. Cram, and A. B. Saunders, 2006: A vortical hot tower route to tropical cyclogenesis. *J. Atmos. Sci.*, **63**, 355–386.

Nolan, D. S., 2007: What is the trigger for tropical cyclogenesis? *Aust. Met. Mag*., **56**, 241 – 266.

Rasmussen, E. N., J. M. Straka, R. Davies-Jones, C. A. Doswell III, F. H. Carr, M. D. Eilts, and D. R. MacGorman, 1994: Verification of the Origins of Rotation in Tornadoes Experiment: VORTEX. *Bull. Amer. Meteor. Soc.,***75,** 995–1006.

Ritchie, E. A., and G. J. Holland, 1997: Scale interactions during the formation of Typhoon Irving. *Mon. Wea. Rev.,* **125,** 1377–1396.

——, and ——, 1999: Large-scale patterns associated with tropical cyclogenesis in the Western Pacific. *Mon. Wea. Rev.,* **127**, 2027–2043.

Rotunno, R., 1981: On the evolution of thunderstorm rotation. *Mon. Wea. Rev.,* **109,** 577–586.

——, and J. B. Klemp, 1982: The influence of the shear-induced pressure gradient on thunderstorm motion. *Mon. Wea. Rev.,* **110,** 136–151

——, and ——, 1985: On the rotation and propagation of simulated supercell thunderstorms. *J. Atmos. Sci.,* **32,** 271 – 292.

Sanders, F., 1986: Explosive cyclogenesis in the west-central North Atlantic Ocean, 1981-84. Part I: Composite structure and mean behavior, *Mon. Wea. Rev*., **114**, 1781-1794.

Simpson, J., E. Ritchie, G. J. Holland, J. Halverson, and S. Stewart, 1997: Mesoscale interactions in tropical cyclone genesis. *Mon. Wea. Rev.,* **125,** 2643–2661.

Sobel, A. H., and E. D. Maloney, 2000: Effect of ENSO and the MJO on western North Pacific tropical cyclones. *Geophys. Res. Lett.,* **27,** 1739–1742.

Skamarock, W. C., J. B. Klemp, J. Dudhia, D. O. Gill, D. M. Barker, W. Wang, and J. G. Powers, 2005: A description of the Advanced Research WRF, version 2. NCAR Tech. Note NCAR/TN-468_STR, 88 pp.

Sperber, K. R., 2003: Propagation and the vertical structure of the Madden-Julian oscillation. *Mon. Wea. Rev.*, **131**, 3018 – 3037.

Stossmeister, G. J., and G.M. *Barnes*, 1992: The Development of a Second Circulation Center within Tropical Storm Isabel (1985). *Mon. Wea. Rev*., **120**, 685–697.

Tao, W.-K., J. Simpson, C.-H. Sui, B. Ferrier, S. Lang, J. Scala, M.-D. Chou, and K. Pickering, 1993: Heating, moisture, and water budgets of tropical and midlatitude squall lines: Comparisons and sensitivity to longwave radiation. *J. Atmos. Sci.*, **50**, 673-690.

Wang, Y., and G. J. Holland, 1996: The beta drift of baroclinic vortices, Part II: Diabatic vortices. *J. Atmos. Sci.,* **53,** 3737–3756.

Weisman, M. L., and J. B. Klemp, 1986: Characteristics of isolated convective storms. *Mesoscale Meteorology and Forecasting,* P. S. Ray, Ed., Amer. Meteor. Soc., 331–358.

——, and C. A. Davis, 1998: Mechanisms for the generation of mesoscale vortices within quasi-linear convective systems. *J. Atmos. Sci*, **55**, 2603–2622.

Willoughby, H. E., F. D. Marks, Jr., and R. J. Feinberg, 1984: Stationary and moving convective bands in hurricanes. *J. Atmos. Sci.*, **22**, 3189-3211.

Yuter, S. E., and R. A. Houze Jr., 1998: The natural variability of precipitating clouds over the western Pacific warm pool. *Quart. J. Roy. Meteor. Soc.*, **124**, 53–99.

Zhang, D.-L., and J. M. Fritsch, 1987: Numerical simulation of the meso-b scale structure and evolution of the 1977 Johnstown flood. Part II: Inertially stable warm-core vortex and the mesoscale convective complex. *J. Atmos. Sci.*, **44**, 2593–2612.

——, and ——,1988 Numerical simulation of the meso-beta scale structure and evolution of the 1977 Johnstown flood. Part III: Internal gravity waves and the squall line. *J. Atmos. Sci.,* **45,** 1252–1268.

——, , and K. Gao, 1989: Numerical simulation of an intense squall line during 10–11 June 1985 PRE-STORM. Part II: Rear inflow, surface pressure perturbations, and stratiform precipitation, *Mon. Wea. Rev*., **117**, 2067–2094.

——, 1992: The formation of a cooling-induced mesovortex in the trailing-stratiform region of a midlatitude squall line, *Mon. Wea. Rev*., **120**, 2763–2785.

——, and N. Bao, 1996a: Oceanic cyclogenesis as induced by a mesoscale convective system moving offshore. Part I: A 90-h real-data simulation. *Mon. Wea. Rev.,* **124,** 1449–1469.

——, and ——, 1996b: Oceanic cyclogenesis as induced by a mesoscale convective system moving offshore. Part II: Genesis and thermodynamic transformation. *Mon. Wea. Rev.,* **124,** 2206–2226.

——, Y. Liu and M.K. Yau, 2001: A multiscale numerical study of Hurricane Andrew (1992). Part IV: Unbalanced flows. *Mon. Wea. Rev.*, **129**, 92-107.

——, and C. Q. Kieu, 2006: Potential vorticity diagnosis of a simulated hurricane. Part II: Quasi-balanced contributions to forced secondary circulations. *J. Atmos. Sci.,* **63,** 2898–2914.

Zhu, C.-W., T. Nakazawa and J.-P. Li, 2003: Modulation of twin tropical cyclogenesis by the MJO westerly wind burst during the onset period of 1997/98 ENSO. *Advances in Atmos. Sci.*, **20**, 882-898.

Zipser, E. J., and C. Gautier, 1978: Mesoscale events within a GATE tropical depression. *Mon. Wea. Rev.*, **106**, 789-805.